Polarized endosome dynamics by spindle asymmetry during asymmetric cell division

Derivery, Emmanuel; Seum, Carole; Daeden, Alicia; Loubery, Sylvain Philippe; Holtzer, Laurentius Henricus; Jülicher, Frank; Gonzalez Gaitan, Marcos

How to cite

DERIVERY, Emmanuel et al. Polarized endosome dynamics by spindle asymmetry during asymmetric cell division. In: Nature, 2015, vol. 528, n° 7581, p. 280–285. doi: 10.1038/nature16443

This publication URL: https://archive-ouverte.unige.ch//unige:143353

Publication DOI: 10.1038/nature16443

LETTER

doi:10.1038/nature16443

Polarized endosome dynamics by spindle asymmetry during asymmetric cell division

Emmanuel Derivery[1], Carole Seum[1], Alicia Daeden[1], Sylvain Loubéry[1], Laurent Holtzer[1], Frank Jülicher[2] & Marcos Gonzalez-Gaitan[1]

During asymmetric division, fate determinants at the cell cortex segregate unequally into the two daughter cells. It has recently been shown that Sara (Smad anchor for receptor activation) signalling endosomes in the cytoplasm also segregate asymmetrically during asymmetric division[1,2]. Biased dispatch of Sara endosomes mediates asymmetric Notch/Delta signalling during the asymmetric division of sensory organ precursors in *Drosophila*[1]. In flies, this has been generalized to stem cells in the gut[3] and the central nervous system[1], and, in zebrafish, to neural precursors of the spinal cord[4]. However, the mechanism of asymmetric endosome segregation is not understood. Here we show that the plus-end kinesin motor Klp98A targets Sara endosomes to the central spindle, where they move bidirectionally on an antiparallel array of microtubules. The microtubule depolymerizing kinesin Klp10A and its antagonist Patronin generate central spindle asymmetry. This asymmetric spindle, in turn, polarizes endosome motility, ultimately causing asymmetric endosome dispatch into one daughter cell. We demonstrate this mechanism by inverting the polarity of the central spindle by polar targeting of Patronin using nanobodies (single-domain antibodies). This spindle inversion targets the endosomes to the wrong cell. Our data uncover the molecular and physical mechanism by which organelles localized away from the cellular cortex can be dispatched asymmetrically during asymmetric division.

We first identified Klp98A as the kinesin mediating Sara endosome motility during sensory organ precursor (SOP) division (Fig. 1). Klp98A is the *Drosophila* homologue of mammalian KIF16B, an early endosomal kinesin containing a phosphatidylinositol 3-phosphate-binding PX domain[5]. Indeed, Klp98A localizes to Sara-positive early endosomes (Extended Data Fig. 1a–e).

During SOP division, Klp98A–GFP-positive Sara endosomes segregate to the pIIa daughter, but not the pIIb[1,2] (Fig. 1a, Supplementary Video 1). Sara endosomes were monitored by following Delta 20 min after internalization (iDelta$_{20}$) through an improved antibody internalization assay[1]. iDelta$_{20}$ parallels Sara endosome dynamics in the controls and mutants studied here (*in vivo* and primary cultures; Extended Data Fig. 2). Like KIF16B[5,6], purified Klp98A (Fig. 1b) binds specifically to phosphatidylinositol 3-phosphate (Extended Data Fig. 1f) and is a plus-end-directed motor (Fig. 1c) whose velocity is $0.76 \pm 0.02\,\mu m\,s^{-1}$ (mean ± s.e.m., $n = 345$ motility strides; Fig. 1d).

To study Klp98A function, we generated deletions within the motor domain (*Klp98A*$^{\Delta 6}$, *Klp98A*$^{\Delta 7}$ and *Klp98A*$^{\Delta 8}$, 6, 7 and 8-base-pair deletions, respectively) and a clean coding sequence deletion (*Klp98A*$^{\Delta 47}$) (Extended Data Fig. 1a, b, g–k). Except *Klp98A*$^{\Delta 6}$, all are protein nulls. In *Klp98A*$^{-}$, Sara endosomes move diffusively (diffusion coefficient $D = 0.0021 \pm 0.0001\,\mu m^2\,s^{-1}$, mean ± s.e.m., $n = 4$ independent methods each based on at least 100 tracks; Fig. 1e, g and Extended Data Fig. 4a–e; 'Mean Square Displacement analysis' in Methods). Therefore, Klp98A mediates Sara endosome motility.

In wild-type cells, Sara endosomes move on microtubules to the Pavarotti-positive central spindle (Fig. 1e–g, Supplementary Video 2) and, late in cytokinesis, to pIIa (Fig. 1a, e, g (arrows) and h). Spindle microtubule plus-ends are oriented towards the equator[7], explaining central spindle endosomal targeting by a plus-end motor. Indeed, Sara endosome central spindle targeting fails in *Klp98A*$^{-}$ mutants (Fig. 1e–g, Supplementary Video 2). Importantly, in *Klp98A*$^{-}$ mutants and upon RNAi-mediated *Klp98A* knockdown, endosomes are symmetrically dispatched (Fig. 1e, g, h).

Klp98A-mediated motility contributes to cell fate assignation through asymmetric Notch signalling, but this activity is redundantly covered by Neuralized and Numb[8]. Indeed, *Klp98A*$^{-}$*;pnr > neur*^{RNAi} double mutants show a synergistic fate assignation phenotype: the notum is largely void of bristles (Fig. 1i, j and Extended Data Fig. 3a, b; 'Quantification of the Neur/Numb phenotypes' in Methods). Conversely, *Klp98A;Numb* double mutants strongly suppress the diagnostic *Numb*$^{-}$ multiple socket phenotype[9] (Extended Data Fig. 3d–f). Therefore, having established the role of Klp98A motility in Notch signalling, we focus here on the mechanisms orchestrating asymmetric motility.

Central spindle targeting of Sara endosomes precedes asymmetric segregation to pIIa. We therefore focused on Sara endosome motility with respect to the central spindle reference frame. The central spindle is composed of the Pavarotti-positive core (containing antiparallel microtubules) plus the microtubules emanating from it[10] (Fig. 2a). We automatically tracked the Pavarotti core, defining a 2D cartesian reference frame whose origin is the Pavarotti centroid and whose *x* axis is the pIIb–pIIa axis (Fig. 2a, b and Supplementary Video 3; for algorithm and accuracy, Methods and Extended Data Fig. 4f–i). This also defines a Pavarotti width (PW) and length (PL, the length of the microtubule antiparallel array). We used the contracting PW for time-registration of our movie data sets (Fig. 2a–c; Methods and Extended Data Fig. 4o–x; registered time 0 represents anaphase B onset).

We then tracked Sara endosomes with respect to this reference frame (with 160 nm accuracy; Methods and Extended Data Fig. 4j–n). Automatic tracking and spatio-temporal registration provided a large data set (2,897 traces) from which a spatio-temporal density plot of endosomes at the central spindle was generated (Fig. 2d). For 500 s, endosomes remain mostly within the Pavarotti region (Fig. 2d). Remarkably, at the central spindle, motility along the *x* axis is bidirectional (Fig. 2e, Supplementary Video 4, Extended Data Fig. 4y). Motility along the *y* axis merely follows PW contraction (Fig. 2f), consistent with motility along central spindle microtubules, parallel to the *x* axis. Velocities are similar towards pIIa ($0.18 \pm 0.1\,\mu m\,sec^{-1}$; mean ± s.e.m., $n = 422$ events) and pIIb ($0.17 \pm 0.09\,\mu m\,sec^{-1}$; $n = 428$ events) and slower than *in vitro* (Fig. 1d), possibly due to crowding by microtubule-associated proteins[11,12].

[1]Department of Biochemistry, Faculty of Sciences, University of Geneva, 30 Quai Ernest Ansermet, Geneva 1211, Switzerland. [2]Max Planck Institute for the Physics of Complex Systems, Nöthnitzer Strasse 38, 01187 Dresden, Germany.

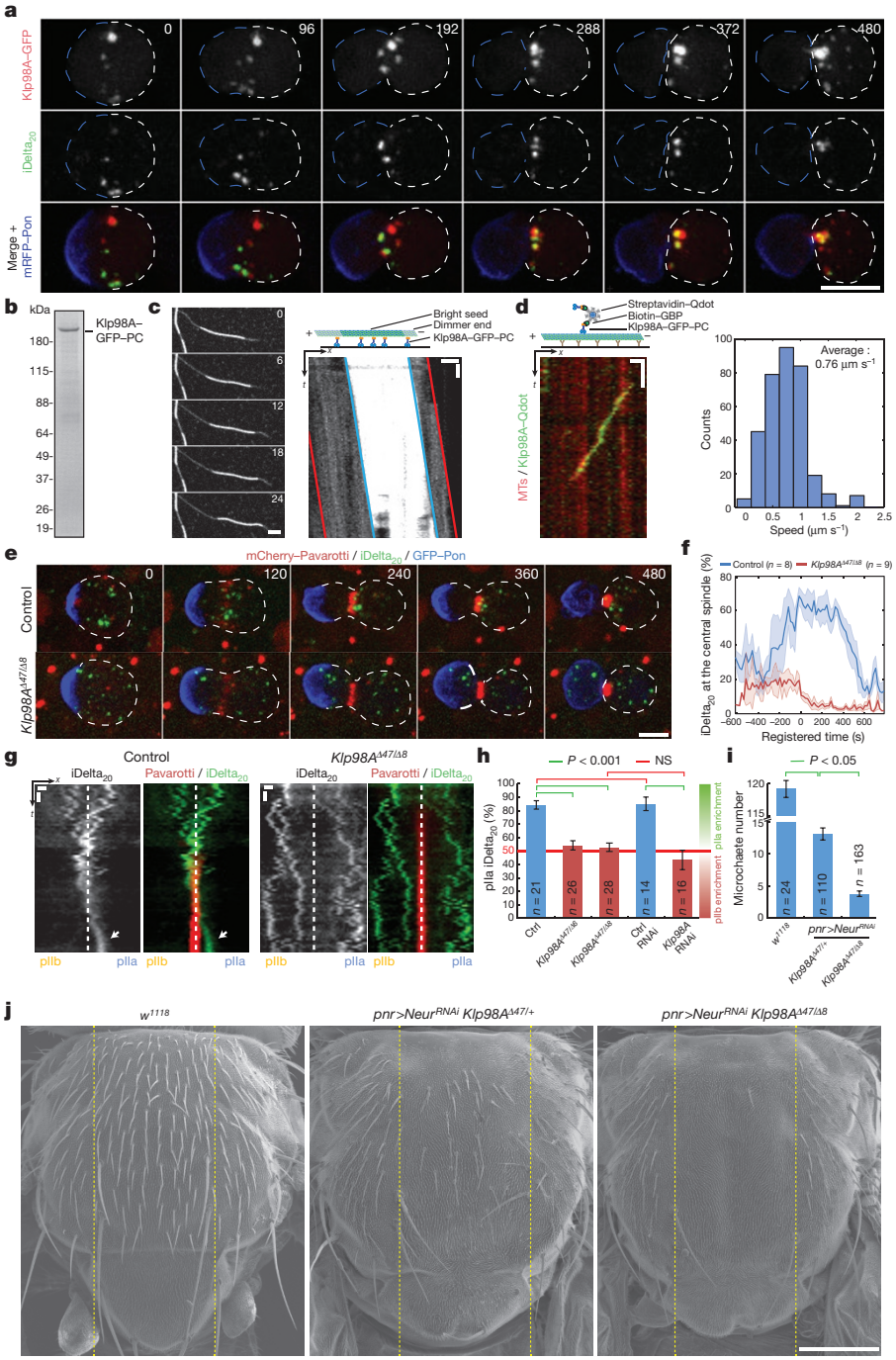

Figure 1 | Klp98A controls Sara endosome motility and central spindle targeting. **a**, Dividing SOP showing Klp98A–GFP, Sara endosomes (iDelta$_{20}$) and mRFP–Pon (monomeric red fluorescent protein fused to the cortex localization domain of Pon, which labels the pIIb cortex: dashed blue lines). pIIa cortex, dashed white lines. 84 ± 3% iDelta$_{20}$ co-localizes with Klp98A (mean ± s.e.m., $n = 51$ cells with a total of 308 endosomes). **b**, Purified Klp98A (Coomassie SDS–PAGE; PC, Protein C tag). **c**, Left, gliding assay of polarity-marked microtubules on purified Klp98A. Right, kymograph. The short, dimmer minus-end leads; Klp98A is a plus-end motor. **d**, Left, kymograph of Klp98A-bound quantum dots (Qdots) moving on microtubules (MTs). Right, speed distribution. **e**–**g**, iDelta$_{20}$ dynamics (**g**; kymograph of horizontal projection of **e**) and central spindle targeting in control and *Klp98A*$^{\Delta 47/\Delta 8}$ mutants (**f**). Time is registered between movies (see Methods). Registered time = 0, anaphaseB onset. **h**, iDelta$_{20}$ segregation after abscission. **i**, **j**, Scanning electron microscopy and microchaete numbers in *panier* region (dashed lines in **j**) in Klp98A/Neuralized mutants. In **h**, **i**, Kruskal–Wallis test. Scale bars: 5 µm (**a**, **e**), 1 µm/2 s (**c**), 5 µm/2 s (**d**), 1 µm/1 min (**g**), 200 µm (**j**). *n*, numbers of SOPs (**f**, **h**) or flies (**i**). Elapsed time, seconds. In **f**, **h**, **i** and throughout this report mean ± s.e.m. is shown.

Confinement within the Pavarotti region and bidirectional movement are both consistent with a plus-end motor switching direction on antiparallel microtubules. On single microtubules, Klp98A-bound quantum dots always maintain their directionality when resuming after a pause ($n = 29$; Fig. 1d). We asked whether Klp98A could switch direction in an antiparallel bundle. In an *in vitro* reconstitution assay, Klp98A-bound quantum dots move bidirectionally within antiparallel MAP65-1-mediated microtubule arrays[13] (Fig. 2g, h, Supplementary Video 5; 68% tracks ($n = 150$) change direction after pausing). Therefore, Klp98A supports bidirectional motility in antiparallel arrays.

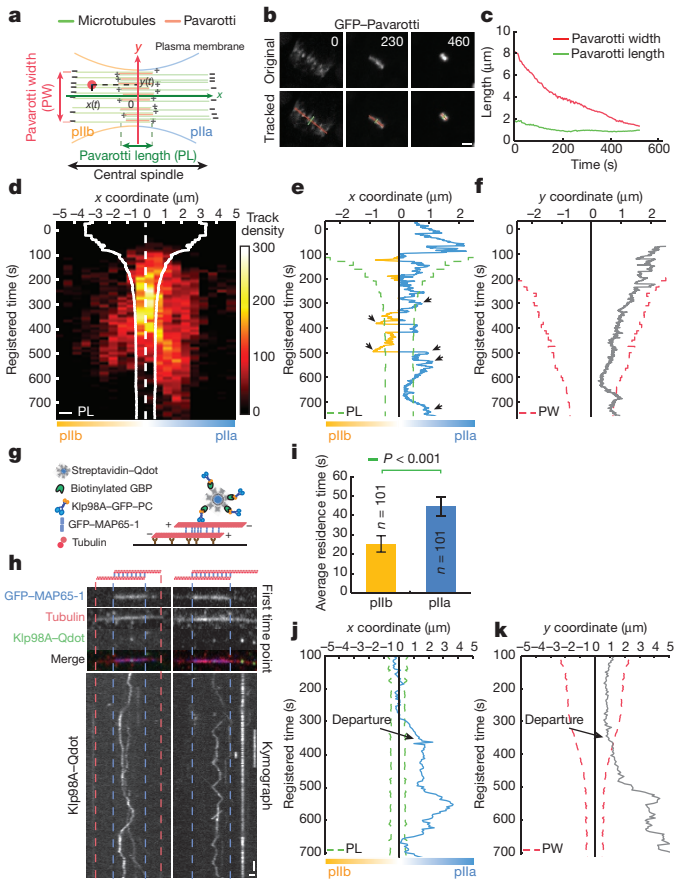

Figure 2 | Asymmetric motility of Sara endosomes at the central spindle. a–c, Central spindle reference frame (**a**), automatic tracking (**b**; PL, green; PW, red) and PW/PL dynamics (**c**). **d**, iDelta$_{20}$ spatio-temporal density plot at the central spindle. 2,897 tracks (45 cells) were registered in space/time and displayed in a single density plot. White line, averaged PL; dashed, Pavarotti centroid. **e**, **f**, Representative track on the *x* (**e**) and *y* (**f**) axes. **g**, **h**, *In vitro* reconstitution of bidirectional motility using Klp98A-bound quantum dots (Qdots) and antiparallel microtubule arrays organized by MAP65-1 (kymographs in **h**). **i**, pIIa/pIIb endosome residence time ($n = 101$ tracks, Mann–Whitney test). **j**, **k**, *x* and *y* axis tracks; see departure event. Scale bars: 2 μm (**b**); 1.2 μm/2 min (**h**).

Notably, *in vivo*, bidirectional endosome motility is asymmetric: the residence time in pIIa is 1.8-fold longer than in pIIb (Fig. 2i). Consistently, the spatio-temporal density plot is asymmetric (Fig. 2d). Furthermore, tracks overshoot beyond the Pavarotti region more frequently into pIIa (Fig. 2e, arrows; see also Fig. 2d).

Eventually, endosomes depart from central spindle microtubules into the cytoplasm and therefore move also on the *y* axis (Fig. 2j, k). The longer pIIa residence time and higher pIIa overshoot frequency make this final departure asymmetric, explaining the biased segregation into pIIa (Fig. 1h). Therefore, asymmetric endosome motility at the central spindle underlies asymmetric dispatch to pIIa.

We then wondered whether the central spindle itself is asymmetric. Using Pavarotti spatio-temporal registration, we generated an 'average cell' to map the densities of the microtubule markers Jupiter[14] and SiR-tubulin[15] (microtubule markers), Patronin[16] (minus-end), and Pavarotti (plus-ends/antiparallel overlap) (Fig. 3a, b; Extended Data Fig. 5a, b; Supplementary Video 6). This 'average cell' reveals a polarity map of the central spindle consistent with electron microscopy reports[17,18]: plus-ends are in the middle and minus-ends on the outer side (Fig. 3c). Microtubule densities in general, and Patronin in particular, are ~20% higher on the pIIb side (Fig. 3a, b; Extended Data Fig. 5c–i: quantifications and endogenous stainings). This asymmetry depends on Par complex activity, and is absent in neighbouring cells dividing symmetrically (Extended Data Fig. 5d–k). We confirmed previous reports of asymmetric centrosomes in SOPs[19–21], but this seems independent of central spindle or endosomal asymmetry (Extended Data Fig. 5l–s).

Microtubule asymmetry builds up during anaphaseB, concomitant with biased endosome motility, while, earlier, the metaphase spindle is symmetrical (Fig. 3d, e; Extended Data Figs 2i and 5l–n; Supplementary Video 7). During anaphaseB, the central spindle shrinks by microtubule depolymerization through depolymerizing kinesins like Klp10A[22,23], among other factors[24–26]. Depolymerization dynamics are asymmetric: microtubule loss is faster in pIIa (Fig. 3f). This could be explained by Patronin enrichment in the central spindle pIIb outer side (Fig. 3a, b) where it binds to minus-ends, counteracting Klp10A-mediated depolymerization[16,23,27,28].

Indeed, Klp10A/Patronin control asymmetric microtubule depolymerization: their depletion abolishes spindle asymmetry (Fig. 3e, g, h; Extended Data Fig. 6: controls, co-depletion and endogenous tubulin immunostainings). In *Patronin*-knockdown cells, both sides exhibit low microtubule densities characteristic of pIIa (Fig. 3g, h), consistent with Patronin pIIb enrichment in wild type (Fig. 3a, b) and its activity against depolymerization[16,23,27,28]. Conversely, upon knockdown of *Klp10A*, both sides exhibit high microtubule densities resembling pIIb (Fig. 3g-i).

The parallelism between central spindle asymmetry and asymmetric endosome motility suggests that spindle asymmetry causes biased motility. Indeed, endosome motility at the central spindle and, therefore, segregation become symmetric in *Klp10A*- and *Patronin*-knockdowns, while early central spindle targeting is normal (Fig. 4a, b; Supplementary Video 8; Extended Data Fig. 7: controls and co-depletion). This uncovers a quantitative correlation between spindle and endosomal asymmetry (Fig. 4c).

Together, a plus-end motor (Fig. 1) and microtubule plus-ends facing the centre (Fig. 3a-c) explain why a higher pIIb microtubule density (~20% enrichment) targets endosomes to pIIa (~80% pIIa, that is, >300% enrichment). In other words, endosomes move away from higher microtubule densities in pIIb.

Based on a theoretical model (see Supplementary Equations) of plus-end endosomal motility on an antiparallel, asymmetric microtubule overlap (Fig. 4d), the steady-state endosome distribution is

$$\frac{P_{\mathrm{pIIa}}}{P_{\mathrm{pIIb}}} = \frac{\rho_{\mathrm{b}}}{\rho_{\mathrm{a}}} \mathrm{e}^{\frac{lk_{\mathrm{on}}v(\rho_{\mathrm{b}}-\rho_{\mathrm{a}})}{Dk_{\mathrm{off}}}} \qquad (1)$$

Where P_{pIIa}, P_{pIIb}, the probabilities for an endosome to be on either side of the antiparallel overlap; ρ_{a}, ρ_{b}, microtubule densities in pIIa/pIIb, respectively; k_{on}, k_{off}, microtubule association/dissociation constants of the motor, respectively; v, the endosome motor-driven velocity; D, the diffusion coefficient of endosomes detached from microtubules; and l, the antiparallel overlap length (Extended Data Fig. 10a; Supplementary Equations).

Based on equation (1), Fig. 4e shows how the pIIa fraction of endosomes $\frac{P_{\mathrm{pIIa}}}{P_{\mathrm{pIIa}}+P_{\mathrm{pIIb}}}$ depends on the normalized difference of microtubule densities $\Delta = \frac{\rho_{\mathrm{b}}-\rho_{\mathrm{a}}}{\rho_{\mathrm{b}}+\rho_{\mathrm{a}}}$. We measured $D = 0.0021 \pm 0.0001\,\mu\mathrm{m}^2\,\mathrm{s}^{-1}$ (Extended Data Fig. 4a–e), $v = 0.173 \pm 0.007\,\mu\mathrm{m\,s}^{-1}$ (Fig. 2e), $l = \mathrm{PL} = 1 \pm 0.1\,\mu\mathrm{m}$ (Fig. 2d), $k_{\mathrm{off}} = 0.90 \pm 0.06\,\mathrm{s}^{-1}$ (Extended Data Fig. 10c) and $k_{\mathrm{on}}\rho = 0.05 \pm 0.01\,\mathrm{s}^{-1}$ (ρ corresponds to the average microtubule density, see Supplementary Information equation (36); Extended Data Fig. 10d). With these parameters, according to equation (1), a 20% microtubule pIIb enrichment is amplified into 300% endosome pIIa enrichment (Fig. 4e). Furthermore, if spindle asymmetry is inverted, endosomes become enriched in pIIb.

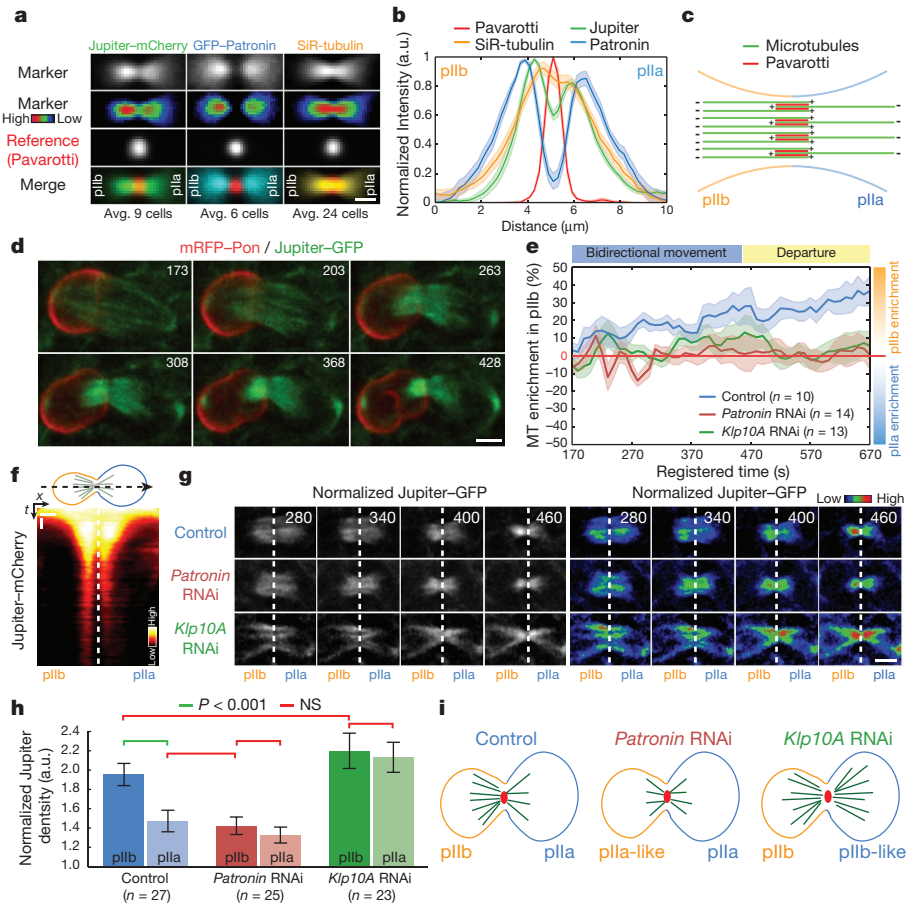

Figure 3 | The central spindle of SOPs is asymmetric. a, Average densities of microtubule markers at the central spindle (live; late cytokinesis, registered time ~600 s). **b**, Line scan through the average spindles in **a**. a.u., arbitrary units. **c**, Central spindle microtubule topology. **d**, Microtubule dynamics in a dividing SOP. **e**, Dynamics of central spindle microtubule (MT) pIIb enrichment ($100 \times \frac{(\rho_b - \rho_a)}{\rho_a}$; ρ_b, pIIb microtubule density; ρ_a, pIIa) in indicated genotypes. **f**, Microtubule density kymograph at central spindle. **g**, **h**, Jupiter–GFP in dividing SOPs of indicated genotypes and quantification (ANOVA). Normalization to pIIa centrosome. NS, not significant. **i**, Patronin/Klp10A phenotypes. Scale bars: 2 μm (**a**, **e**, **g**), 2 μm/1 min (**f**). Elapsed time in **d** and **g** is given in seconds and corresponds to registered time; *n*, SOP number.

To generate this inverted spindle, we established a 'nanobody assay' based on GFP-binding-peptide (GBP)–Pon, a nanobody fused to the Pon localization domain (Supplementary Information; Extended Data Figs 8 and 9). GBP–Pon traps GFP–Patronin away from the spindle at the pIIb cortex thereby reducing, specifically in pIIb, Patronin-dependent protection against central spindle depolymerization (Fig. 4f, g, white arrowheads; Supplementary Video 9). This inverts spindle asymmetry (Fig. 4g, red arrows), which consequently inverts endosomal asymmetry (green arrows; Extended Data Fig. 8c, d, h for controls). SiR-Tubulin and endogenous acetyl-tubulin stainings confirmed this spindle inversion (Extended Data Figs 8e–g and 9h; Supplementary Video 10).

Interestingly, this assay generates a phenotypic series of different levels of spindle reversal and their corresponding endosomal reversals. These data fall on the theoretical curve obtained with independently measured parameters: equation (1) captures the observed spindle/endosome correlation (Fig. 4h; Extended Data Fig. 10f; Supplementary Information equation (36)). Beyond the nanobody assay, equation (1) accounts for our entire data set (Jupiter–GFP and GFP–Patronin controls, *Klp10A* and *Patronin* RNAi knockdowns, and nanobody assay; Fig. 4i; Extended Data Fig. 10g). Therefore our results uncover the quantitative dependence of asymmetric endosome targeting on spindle asymmetry.

Here we identified Klp10A/Patronin as the machinery generating spindle asymmetry, which is read out by Klp98A to achieve asymmetric targeting of signalling endosomes. Asymmetric endosomal targeting contributes in turn to asymmetric cell fate assignation, confirming previous reports in flies[1–3] and fish[4]. Our data thus uncover a mechanism by which intracellular cargoes in general, and signalling endosomes in particular, can be targeted to one of the daughter cells during asymmetric division.

How could then other cargoes segregate symmetrically, if the spindle is asymmetric? Asymmetric targeting would only be efficient if k_{on}, k_{off} and v are optimized to amplify the mild asymmetry of the spindle, otherwise concealed by noise sources in the cell. More generally, plus- and minus-end motors are present simultaneously in the same vesicle and thereby may counteract each other to achieve symmetrical dispatch (a sort of 'tug of war'). Therefore, the precise landscape of microtubule polarity trails combined with the right cocktail of motors in vesicles provides the plasticity required to generate the plethora of molecular spatial patterns observed in polarized cells.

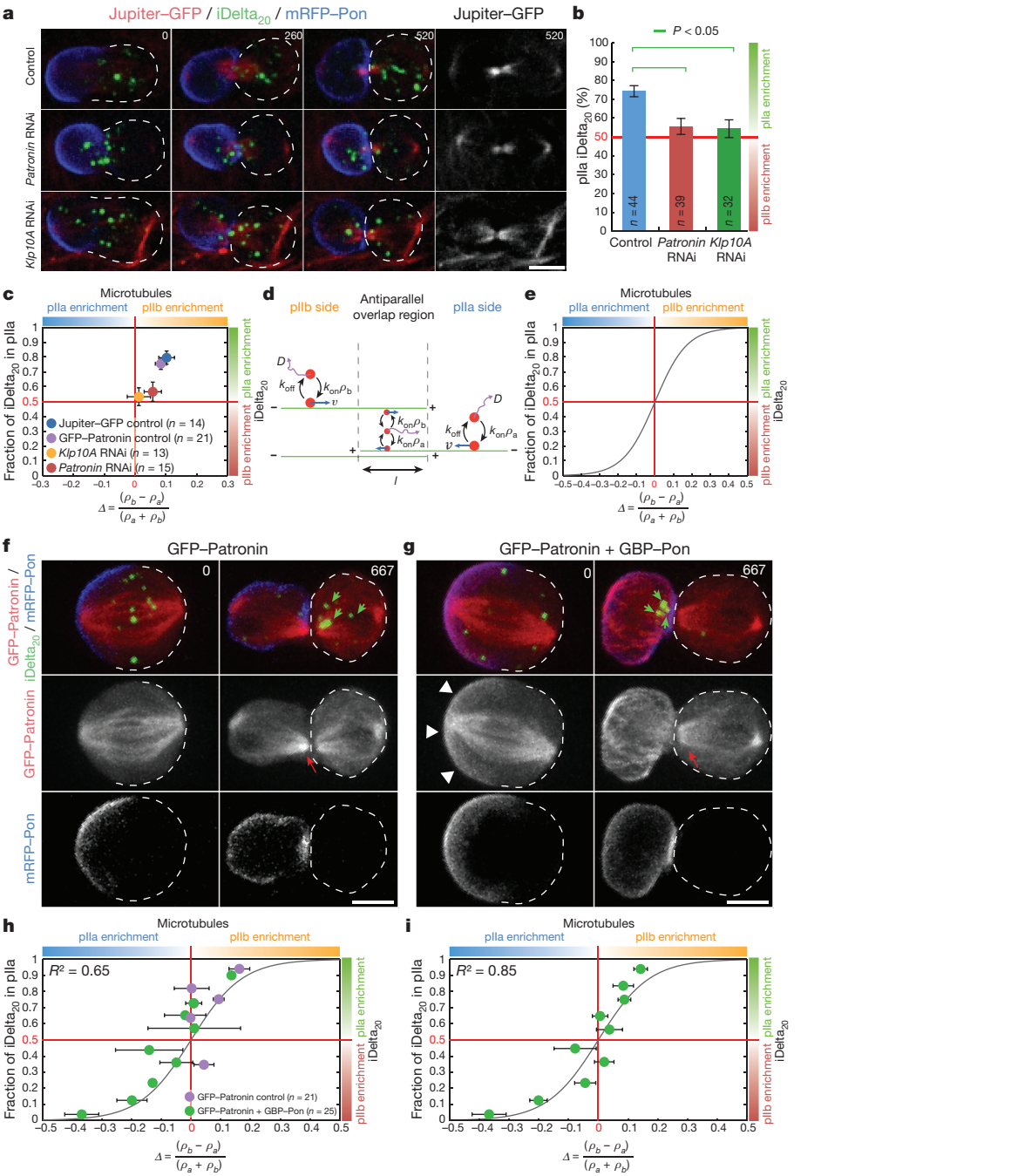

Figure 4 | Central spindle asymmetry orchestrates Sara endosome asymmetry. a, **b**, Microtubule/iDelta$_{20}$ dynamics (**a**) and iDelta$_{20}$ percentage in pIIa after abscission in SOPs of indicated genotypes (**b**; ANOVA). **c**, iDelta$_{20}$ pIIa fraction versus normalized microtubule pIIb enrichment ($\Delta = \frac{\rho_b - \rho_a}{\rho_a + \rho_b}$) measured simultaneously in indicated genotypes (registered time ≈ 600 s). **d**, **e**, Endosome segregation model by motor transport on an antiparallel microtubule overlap (**d**) and endosome-segregation/spindle-asymmetry dependence from the model (**e**; Supplementary Information equation (36)). **f**, **g**, GFP–Patronin and iDelta$_{20}$ dynamics without (**f**) and with (**g**) expression of GBP–Pon. **h**, iDelta$_{20}$ pIIa fraction versus normalized microtubule pIIb enrichment (as in **c**) in indicated genotypes and theoretical curve (as in **e**). Data point binning performed according to iDelta$_{20}$ segregation (un-binned, Extended Data Fig. 10f). **i**, Plot, as in **h**, for the pooled data from all genotypes in this study. (Un-binned, Extended Data Fig. 10g). Scale bars, 5 μm; elapsed time is given in seconds; *n*, SOP number.

Online Content Methods, along with any additional Extended Data display items and Source Data, are available in the online version of the paper; references unique to these sections appear only in the online paper.

Received 19 December 2014; accepted 11 November 2015.

1. Coumailleau, F., Furthauer, M., Knoblich, J. A. & Gonzalez-Gaitan, M. Directional Delta and Notch trafficking in Sara endosomes during asymmetric cell division. *Nature* **458,** 1051–1055 (2009).
2. Loubéry, S. *et al.* Uninflatable and Notch control the targeting of Sara endosomes during asymmetric division. *Curr. Biol.* **24,** 2142–2148 (2014).
3. Montagne, C. & Gonzalez-Gaitan, M. Sara endosomes and the asymmetric division of intestinal stem cells. *Development* **141,** 2014–2023 (2014).
4. Kressmann, S., Campos, C., Castanon, I., Furthauer, M. & Gonzalez-Gaitan, M. Directional Notch trafficking in Sara endosomes during asymmetric cell division in the spinal cord. *Nature Cell Biol.* **17,** 333–339 (2015).
5. Hoepfner, S. *et al.* Modulation of receptor recycling and degradation by the endosomal kinesin KIF16B. *Cell* **121,** 437–450 (2005).
6. Soppina, V. *et al.* Dimerization of mammalian kinesin-3 motors results in superprocessive motion. *Proc. Natl Acad. Sci. USA* **111,** 5562–5567 (2014).
7. Glotzer, M. The 3Ms of central spindle assembly: microtubules, motors and MAPs. *Nature Rev. Mol. Cell Biol.* **10,** 9–20 (2009).

8. Fürthauer, M. & Gonzalez-Gaitan, M. Endocytic regulation of notch signalling during development. *Traffic* **10,** 792–802 (2009).
9. Wang, S., Younger-Shepherd, S., Jan, L. Y. & Jan, Y. N. Only a subset of the binary cell fate decisions mediated by Numb/Notch signaling in *Drosophila* sensory organ lineage requires Suppressor of Hairless. *Development* **124,** 4435–4446 (1997).
10. Fededa, J. P. & Gerlich, D. W. Molecular control of animal cell cytokinesis. *Nature Cell Biol.* **14,** 440–447 (2012).
11. Korten, T. & Diez, S. Setting up roadblocks for kinesin-1: mechanism for the selective speed control of cargo carrying microtubules. *Lab Chip* **8,** 1441–1447 (2008).
12. LaPointe, N. E. *et al.* The amino terminus of tau inhibits kinesin-dependent axonal transport: implications for filament toxicity. *J. Neurosci. Res.* **87,** 440–451 (2009).
13. Stoppin-Mellet, V., Fache, V., Portran, D., Martiel, J. L. & Vantard, M. MAP65 coordinate microtubule growth during bundle formation. *PLoS ONE* **8,** e56808 (2013).
14. Karpova, N., Bobinnec, Y., Fouix, S., Huitorel, P. & Debec, A. Jupiter, a new *Drosophila* protein associated with microtubules. *Cell Motil. Cytoskeleton* **63,** 301–312 (2006).
15. Lukinavičius, G. *et al.* Fluorogenic probes for live-cell imaging of the cytoskeleton. *Nature Methods* **11,** 731–733 (2014).
16. Goodwin, S. S. & Vale, R. D. Patronin regulates the microtubule network by protecting microtubule minus ends. *Cell* **143,** 263–274 (2010).
17. Euteneuer, U. & McIntosh, J. R. Polarity of midbody and phragmoplast microtubules. *J. Cell Biol.* **87,** 509–515 (1980).
18. Schiel, J. A. *et al.* Endocytic membrane fusion and buckling-induced microtubule severing mediate cell abscission. *J. Cell Sci.* **124,** 1411–1424 (2011).
19. Januschke, J., Llamazares, S., Reina, J. & Gonzalez, C. *Drosophila* neuroblasts retain the daughter centrosome. *Nature Commun.* **2,** 243 (2011).
20. Januschke, J. *et al.* Centrobin controls mother–daughter centriole asymmetry in *Drosophila* neuroblasts. *Nature Cell Biol.* **15,** 241–248 (2013).
21. Jauffred, B. *et al.* Regulation of centrosome movements by numb and the collapsin response mediator protein during *Drosophila* sensory progenitor asymmetric division. *Development* **140,** 2657–2668 (2013).
22. Ems-McClung, S. C. & Walczak, C. E. Kinesin-13s in mitosis: key players in the spatial and temporal organization of spindle microtubules. *Semin. Cell Dev. Biol.* **21,** 276–282 (2010).
23. Wang, H., Brust-Mascher, I., Civelekoglu-Scholey, G. & Scholey, J. M. Patronin mediates a switch from kinesin-13-dependent poleward flux to anaphase B spindle elongation. *J. Cell Biol.* **203,** 35–46 (2013).
24. Connell, J. W., Lindon, C., Luzio, J. P. & Reid, E. Spastin couples microtubule severing to membrane traffic in completion of cytokinesis and secretion. *Traffic* **10,** 42–56 (2009).
25. Matsuo, M. *et al.* Katanin p60 contributes to microtubule instability around the midbody and facilitates cytokinesis in rat cells. *PLoS ONE* **8,** e80392 (2013).
26. Yang, D. *et al.* Structural basis for midbody targeting of spastin by the ESCRT-III protein CHMP1B. *Nature Struct. Mol. Biol.* **15,** 1278–1286 (2008).
27. Hendershott, M. C. & Vale, R. D. Regulation of microtubule minus-end dynamics by CAMSAPs and Patronin. *Proc. Natl Acad. Sci. USA* **111,** 5860–5865 (2014).
28. Jiang, K. *et al.* Microtubule minus-end stabilization by polymerization-driven CAMSAP deposition. *Dev. Cell* **28,** 295–309 (2014).

Supplementary Information is available in the online version of the paper.

Acknowledgements We thank A. Gautreau, in whose laboratory the GBP was cloned, for allowing us to use it before his own publication. We thank A. Gautreau, R. Vale, A. Houdusse, A. Roux, A. Trushko and V. Stoppin-Mellet for discussions and advices. We thank N. Chiaruttini for the preparation of liposomes and for insights throughout the project. We thank R. Le Borgne, S. Eaton, S. De Renzis, F. Karch, W. Zhong and R. Stanewsky for flies. We thank P. Kapusta from Picoquant for help with FLIM data analysis. We thank V. Stoppin-Mellet, M. Vantard and J. Gaillard for the gift of GFP-MAP65-1. We are indebted to J. Teyssier, E. Allémann and N. Boulens for letting us use their scanning electron microscopes. E.D. is supported by a Long term Fellowship of the Human Frontier Science Program. L.H. and S.L. are supported by a Marie-Curie Intra-European Fellowship. M.G.G. is supported by Departement de l'Instruction Publique of the Canton of Geneva, the SNF, the SystemsX epiPhysX program, the NCCR Chemical Biology program, the ERC (Sara and Morphogen) and the Polish–Swiss research programs.

Author Contributions E.D. conducted most of the biochemical experiments, imaging and image analysis and wrote the Matlab and ImageJ codes for spindle/endosome tracking and cell averaging with help from L.H. C.S. generated the anti-Klp98A antibody and characterized the four Klp98A mutants used in this study, with help from S.L. C.S., A.D. and S.L. performed additional imaging and genetic experiments. The model of endosome motility was developed jointly by E.D., M.G.G. and F.J. M.G.G. and E.D. designed the project. All authors contributed to writing the paper.

Author Information Reprints and permissions information is available at www.nature.com/reprints. The authors declare no competing financial interests. Readers are welcome to comment on the online version of the paper. Correspondence and requests for materials should be addressed to M.G.G. (marcos.gonzalez@unige.ch), F.J. (julicher@pks.mpg.de) or E.D. (emmanuel.derivery@unige.ch).

METHODS

Generation of *Klp98* mutants. *Klp98A*$^{\Delta 47}$ is a null allele generated by homologous recombination with the 'ends-out' strategy[29,30] using a pW25 plasmid containing two homology fragments flanking the coding region of *Klp98A* as described[31] (2,848 bp of homology in the 5′ region and 4,011 bp in the 3′ region, Extended Data Fig. 1g). Upon recombination, this construct replaces the coding sequence of *Klp98A* by the w^{hs} gene flanked by two *lox*P sites followed by an AttP ΦC31 site. The w^{hs} gene is subsequently floxed to generate *Klp98A*$^{\Delta 47}$ which corresponds to a deletion of the *Klp98A* coding sequence (Extended Data Fig. 1h). Gene deletion was confirmed by PCR (Extended Data Fig. 1i) and sequencing.

Three zinc-finger nuclease pairs targeting *Klp98A* were designed and produced by Sigma-Aldrich (product number CSTZFNY-1KT, lot number 03041026MN). The target sequences were (cut site indicated with underlining): no. 1, CAGAGCACTGGGCATGGGCTAAGGGTGCGGGAGCATCG; no. 2, CTTCGACTACTCCTATTGGTCATTCGATGCGGAGGATCCG; and no. 3, CTCTTTGCCCGCATGCGTGTGGGCCAGGAGTCGGGCA.

The mRNAs corresponding to the three pairs were injected together at 40 ng μl^{-1} in w^{1118} embryos by BestGene Inc. Adults from these embryos were crossed with *w;Df(3R)BSC497/TM6c*. *Df(3R)*BSC497 is a deletion spanning the *Klp98A* gene (Flybase and our own unpublished data). The relevant progeny (about 50 individuals) was then analysed by PCR using primers flanking the three cut sites and the amplicons sequenced. We found deletions only in the region corresponding to the zinc-finger pair no. 1. We studied three of them in more detail: *Klp98A*$^{\Delta 6}$, *Klp98A*$^{\Delta 7}$ and *Klp98A*$^{\Delta 8}$. *Klp98A*$^{\Delta 6}$ is a G to C substitution at position 500 of the coding sequence of *Klp98A* (CG5658-PA) followed by a six-nucleotide deletion. The amino acid sequence at position 167 is therefore changed from 164TGHGLRVRE172 to 164TGHA—VRE170 (see Extended Data Fig. 1j). This two amino acid deletion maps into the L8 loop of the motor domain of Klp98A and does not affect the stability of the protein (see Extended Data Fig. 1k) but behaves like a strong mutant in transheterozygocity with *Klp98A*$^{\Delta 47}$ (see Fig. 1h, Extended Data Fig. 3a, b, d–f). *Klp98A*$^{\Delta 7}$ is a deletion of seven nucleotides at position 502 in the coding sequence of Klp98A, leading to a frameshift starting at amino acid 168 and causing a stop codon after amino acid 209. *Klp98A*$^{\Delta 8}$ is a deletion of eight nucleotides at position 501, leading to a frameshift starting at amino acid 168 and causing a stop codon after amino acid 186.

Full-length Klp98A protein is undetectable in homozygous *Klp98A*$^{\Delta 47}$, *Klp98A*$^{\Delta 7}$ and *Klp98A*$^{\Delta 8}$ animals (Extended Data Fig. 1a, k). In this work, transheterozygous animals (that is, *Klp98A*$^{\Delta 47/\Delta 6}$ and *Klp98A*$^{\Delta 47/\Delta 8}$) were used in phenotypic analyses in order to avoid the effects of potential linked mutations. These transheterozygous combinations are viable and fertile. However, these mutants show Notch-dependent asymmetric cell fate assignation phenotypes when the other two systems controlling these events, that is, Numb and Neuralized, are compromised (see Fig. 1i, j and Extended Data Fig. 3).

Fly strains. Transgenes used in this study included *Ubi > mCherry-Pavarotti* (generated for this study), *UAS > Jupiter-mCherry* (this study), *UAS > Klp98A-mCherry* (this study), *UAS > Klp98A-GFP* (this study), *UAS-GFP-Patronin* (this study), *Asense > GFP-Pon* (this study), *Asense > mCherry-Pon* (this study), *Asense > GFP-Sara* (this study), *UAS-GBP-Pon* (this study), *UAS-GBP-mCherry-Pon* (this study), *UAS-GBP-Bazooka* (this study), *Jupiter-GFP* knock-in at the endogenous locus (ref. 14, Bloomington no. 6836), *UAS-mRFP-Pon* (ref. 32), *UAS-mRFP-Sara* (ref. 1), *Neur > Gal4* (ref. 33), *Ubi > GFP-Pavarotti* (ref. 34), *UAS > GFP-Pon* (ref. 35), *pnr > Gal4, phyllopod > GFP-Pon* (ref. 36), *pnr > Gal4* (Bloomington no. 3039), UAS > DsRed (kind gift from François Karch), *UAS > Patronin*$^{RNAi\#1}$ (VDRC no. 108927, referred to as *Patronin RNAi* in the main text), *UAS > Patronin*$^{RNAi\#2}$ (VDRC no. 27654), *UAS > Klp10A*^{RNAi} (ref. 37, VDRC no. 41534), *UAS > Klp98A*^{RNAi} (VDRC no. 40605), *UAS > Neuralized*^{RNAi} (VDRC no. 108239), *UAS > Numb*^{RNAi} (gift from W. Zhong, ref. 38), *Df(3R)BSC497* (Bloomington no. 25001), *Klp98A*$^{\Delta 47}$ (this study), *Klp98A*$^{\Delta 6}$ (this study), *Klp98A*$^{\Delta 7}$ (this study), *Klp98A*$^{\Delta 8}$ (this study), *Numb*^{SW} (ref. 9, gift from R. Stanewsky), *Numb*^{2} (kind gift from Roland Le Borgne), *Numb*^{15} (kind gift from Roland Le Borgne), *UAS > lgl3A* (ref. 39), *GFP-Rab5* knock-in at the endogenous locus (ref. 40), *YFP-Rab11* knock-in at the endogenous locus (ref. 41), *YFP-Rab7* knock-in at the endogenous locus (ref. 41) and *tub > Gal80*^{ts} (Bloomington no. 7017). The genotypes of mutant stocks were verified by PCR and sequencing, as well as the genotypes of the F1 progeny generated for interaction studies (Fig. 1i, j and Extended Data Fig. 3). Since the Jupiter–GFP gene trap is viable, fertile and does not induce visible phenotypes in the SOP lineage, we used it as an alternative to balancers for controls in gene interaction studies (Extended Data Fig. 3). Flies co-expressing GBP–Pon and GFP–Patronin (Fig. 4 and Extended Data Figs 8 and 9) displayed occasional polarity defects reflected by loss of mRFP–Pon asymmetry (See Extended Data Fig. 8d for quantification). Cells showing such polarity defects were excluded from subsequent analysis. We used *Gal80*^{ts} to achieve low levels of Klp98A–GFP expression to prevent endosome fusion (Fig. 1a, Extended Data Figs 1c–e and 2a, b).

Detailed genotypes and temperatures. Fig. 1a: w^{1118}*; Neur > Gal4 UAS > mRFP-Pon tub > gal80*^{ts}*/UAS > Klp98A-GFP* (25 °C).

Fig. 1e–g: w^{1118}*; Asense > GFP-Pon/Ubi > mCherry-Pavarotti* (25 °C). w^{1118}*; Asense > GFP-Pon/Ubi > mCherry-Pavarotti;Klp98A*$^{\Delta 47}$*/Klp98A*$^{\Delta 8}$(25 °C).

Fig. 1h: control: w^{1118}*; Asense > GFP-Pon/Ubi > mCherry-Pavarotti* (25 °C). *Klp98A*$^{\Delta 47/\Delta 6}$: w^{1118}*; Neur > Gal4 UAS > mRFP-Pon Klp98A*$^{\Delta 47}$*/Klp98A*$^{\Delta 6}$ (25 °C). *Klp98A*$^{\Delta 47/\Delta 8}$: w^{1118}*; Asense > GFP-Pon/Ubi > mCherry-Pavarotti;Klp98A*$^{\Delta 47}$*/Klp98A*$^{\Delta 8}$ (25 °C). Control RNAi: w^{1118}*; pnr > Gal4, phyllopod > GFP-Pon/+* (29 °C). Klp98A RNAi: w^{1118}*; pnr > Gal4, phyllopod > GFP-Pon/UAS > Klp98A*^{RNAi} (29 °C).

Fig. 1i, j: w^{1118} (25 °C). w^{1118}*; UAS > Neur*^{RNAi}*/+;pnr > Gal4 UAS > DsRed Klp98A*$^{\Delta 47}$*/TM6B* (29 °C). w^{1118}*; UAS > Neur*^{RNAi}*/+;pnr > Gal4 UAS > DsRed Klp98A*$^{\Delta 47}$*/Klp98A*$^{\Delta 8}$ (29 °C, sibling of fly above).

Fig. 2b–g, i–k: w^{1118}*;Neur > Gal4, UAS > mRFP-Pon, Ubi > GFP-Pavarotti/+* (25 °C).

Fig. 3a: w^{1118}*; UAS > Jupiter-mCherry/+; Neur > Gal4, Ubi > Pavarotti-GFP/+* (25 °C). w^{1118}*; Ubi > mCherry-Pavarotti/+;Neur > Gal4, tub > Gal80*^{ts}*/UAS > GFP-Patronin* (25 °C). w^{1118}*; Neur > Gal4, UAS > mRFP-Pon, Ubi > Pavarotti-GFP/+* (25 °C, for SiR-Tubulin column).

Fig. 3d: w^{1118}*;UAS > mRFP-Pon/+;Neur > Gal4, Jupiter-GFP/+* (25 °C).

Fig. 3e, g, h: control: w^{1118}*;UAS > mRFP-Pon/+;Neur > Gal4, Jupiter-GFP/+* (29 °C). Patronin RNAi: w^{1118}*;UAS > Patronin*$^{RNAi\#1}$*/UAS > mRFP-Pon;Neur > Gal4, Jupiter-GFP/+* (29 °C). Klp10A RNAi: w^{1118}*;Asense > mCherry-Pon/+;pnr > Gal4, Jupiter-GFP/UAS > Klp10A*^{RNAi} (29 °C).

Fig. 3f: w^{1118}*;UAS > Jupiter-mCherry;Neur > Gal4, Ubi > GFP-Pavarotti/+* (25 °C).

Fig. 4a, b: control: w^{1118}*;UAS > mRFP-Pon/+;Neur > Gal4, Jupiter-GFP/+* (29 °C). Patronin RNAi: w^{1118}*;UAS > Patronin*$^{RNAi\#1}$*/UAS > mRFP-Pon;Neur > Gal4, Jupiter-GFP/+* (29 °C). Klp10A RNAi: w^{1118}*;UAS > Jupiter-mCherry/+;pnr > Gal4, phyllopod > GFP-Pon/UAS > Klp10A*^{RNAi} (29 °C).

Fig. 4c: w^{1118}*;UAS > mRFP-Pon/+;Neur > Gal4, Jupiter-GFP/+* (25 °C). w^{1118}*;UAS > Patronin*$^{RNAi\#1}$*/UAS > mRFP-Pon;Neur > Gal4, Jupiter-GFP/+* (29 °C). w^{1118}*;Asense > mCherry-Pon/+;pnr > Gal4, Jupiter-GFP/UAS > Klp10A*^{RNAi} (29 °C). w^{1118}*;Neur > Gal4, UAS > mRFP-Pon/UAS > GFP-Patronin* (25 °C).

Fig. 4f: w^{1118}*;Neur > Gal4, UAS > mRFP-Pon/UAS > GFP-Patronin* (25 °C).

Fig. 4g: w^{1118}*;UAS > GBP-Pon/+;Neur > Gal4, UAS > mRFP-Pon/UAS > GFP-Patronin* (25 °C).

Fig. 4h: w^{1118}*;Neur > Gal4, UAS > mRFP-Pon/UAS > GFP-Patronin* (25 °C). w^{1118}*;UAS > GBP-Pon/+;Neur > Gal4, UAS > mRFP-Pon/UAS > GFP-Patronin* (25 °C).

Fig. 4i: w^{1118}*;Neur > Gal4, UAS > mRFP-Pon/UAS > GFP-Patronin* (25 °C). w^{1118}*;UAS > GBP-Pon/+;Neur > Gal4, UAS > mRFP-Pon/UAS > GFP-Patronin* (25 °C). w^{1118}*;UAS > mRFP-Pon/+;Neur > Gal4, Jupiter-GFP/+* (25 °C). w^{1118}*;UAS > Patronin*$^{RNAi\#1}$*/UAS > mRFP-Pon;Neur > Gal4, Jupiter-GFP/+* (29 °C). w^{1118}*;Asense > mCherry-Pon/+;pnr > Gal4, Jupiter-GFP/UAS > Klp10A*^{RNAi} (29 °C).

Extended Data Fig. 1a: w^{1118} (25 °C). w^{1118}*;Klp98A*$^{\Delta 47}$*/Klp98A*$^{\Delta 47}$ (25 °C). w^{1118}*;Klp98A*$^{\Delta 8}$*/Klp98A*$^{\Delta 8}$ (25 °C).

Extend Data Fig. 1b: w^{1118};Neur > Gal4, UAS > mRFP-Pon/+ (25 °C). w^{1118};Asense > GFP-Pon/Ubi > mCherry-Pavarotti;*Klp98A*$^{\Delta 47}$*/Klp98A*$^{\Delta 8}$ (25 °C).

Extended Data Fig. 1c: iDelta$_{20}$ endogenous Klp98A: w^{1118}*;Neur > Gal4 UAS > mRFP-Pon* (25 °C). GFP–Sara endogenous Klp98A: w^{1118}*;Asense > GFP-Sara/+;Neur > Gal4 UAS > mRFP-Pon/+* (29 °C). GFP–Sara Klp98A–mCherry: w^{1118}*;Asense > GFP-Sara/+;Neur > Gal4 tub > gal80*^{ts} *UAS > Klp98A-mCherry/+* (29 °C). GFP–Rab5 Klp98A–mCherry: w^{1118}*;GFP-Rab5/+;Neur > Gal4 tub > gal80*^{ts} *UAS > Klp98A-mCherry/+* (25 °C). YFP–Rab7 Klp98A–mCherry: w^{1118}*;Neur > Gal4 tub > gal80*^{ts} *UAS > Klp98A-mCherry/YFP-Rab7* (25 °C). YFP-Rab11 Klp98A–mCherry: w^{1118}*;Neur > Gal4 tub > gal80*^{ts} *UAS > Klp98A-mCherry/YFP-Rab11*(25 °C).

Extended Data Fig. 1d: GFP–Sara Klp98A–mCherry: w^{1118}*;Asense > GFP-Sara/+;Neur > Gal4 tub > gal80*^{ts} *UAS > Klp98A-mCherry/+* (29 °C). GFP–Rab5 Klp98A–mCherry: w^{1118}*;GFP-Rab5/+;Neur > Gal4 tub > gal80*^{ts} *UAS > Klp98A-mCherry/+* (25 °C). YFP–Rab7 Klp98A–mCherry: w^{1118}*;Neur > Gal4 tub > gal80*^{ts} *UAS > Klp98A-mCherry/YFP-Rab7* (25 °C).

Extended Data Fig. 1e: control: w^{1118}*;Asense > GFP-Sara/+;Neur > Gal4 UAS > mRFP-Pon/+* (29 °C). Klp98A–mCherry: w^{1118}*;Asense > GFP-Sara/+;Neur > Gal4 tub > gal80*^{ts} *UAS > Klp98A-mCherry/+* (29 °C).

Extended Data Fig. 1i: w^{1118} (25 °C). w^{1118}*;Df(3R)BSC497/Klp98A*$^{\Delta 47}$ (25 °C).

Extended Data Fig. 1k: w^{1118} (25 °C). w^{1118}*;Klp98A*$^{\Delta 6}$*/Klp98A*$^{\Delta 6}$ (25 °C). w^{1118}*;Klp98A*$^{\Delta 7}$*/Klp98A*$^{\Delta 7}$ (25 °C). w^{1118}*;Klp98A*$^{\Delta 8}$*/Klp98A*$^{\Delta 8}$ (25 °C).

Extended Data Fig. 2a, b: control: w^{1118}*;Asense > GFP-Sara/+;Neur > Gal4 UAS > mRFP-Pon/+* (29 °C). *Klp98A*$^{\Delta 47}$*/Klp98A*$^{\Delta 6}$: w^{1118}*;Asense > GFP-Sara Asense-mCherry-Pon/+;Klp98A*$^{\Delta 7}$*/Klp98A*$^{\Delta 6}$ (29 °C). *Klp98A*$^{\Delta 47}$*/Klp98A*$^{\Delta 8}$: w^{1118}*;Asense >*

GFP-Sara Asense-mCherry-Pon/+;Klp98A$^{\Delta 7}$/Klp98A$^{\Delta 8}$ (29 °C). Patronin RNAi: *w^{1118};Asense > GFP-Sara/UAS > Patronin$^{RNAi\#1}$;Neur > Gal4 UAS > mRFP-Pon/+* (29 °C). Klp10A RNAi: *w^{1118};Asense > GFP-Sara/+;pnr > Gal4 UAS > DsRed/UAS > Klp10A^{RNAi}* (29 °C). Klp98A–mCherry: *w^{111};Asense > GFP-Sara/+;Neur > Gal4 tub > gal80^{ts} UAS > Klp98A-mCherry/+* (29 °C). GFP-Patronin + GBP-Pon: *w^{1118};UAS > GBP-Pon/tub > gal80^{ts};UAS > GFP-Patronin/Neur > Gal4 UAS > mRFP-Sara* (25 °C).

Extended Data Fig. 2c: *w^{1118};Asense > GFP-Sara/+;Neur > Gal4 UAS > mRFP-Pon/+* (29 °C).

Extended Data Fig. 2d: *w^{1118};Asense > GFP-Sara Asense-mCherry-Pon/+;Klp98A$^{\Delta 47}$/Klp98A$^{\Delta 8}$* (29 °C).

Extended Data Fig. 2e: *w^{1118};Asense > GFP-Sara/UAS > Patronin$^{RNAi\#1}$;Neur > Gal4 UAS > mRFP-Pon/+* (29 °C).

Extended Data Fig. 2f: *w^{1118};Asense > GFP-Sara/+;pnr > Gal4 UAS > DsRed/UAS > Klp10A^{RNAi}* (29 °C).

Extended Data Fig. 2g: *w^{1118};Asense > GFP-Sara/+;Neur > Gal4 tub > gal80^{ts} UAS > Klp98A-mCherry/+* (29 °C).

Extended Data Fig. 2h: *w^{1118};UAS > GBP-Pon/tub > gal80^{ts};UAS > GFP Patronin/Neur > Gal4 UAS > mRFP-Sara* (25 °C).

Extended Data Fig. 2i: *w^{1118};Asense > GFP-Pon/Ubi > mCherry-Pavarotti* (25 °C). *w^{1118};Asense > GFP-Pon/Ubi > mCherry-Pavarotti;Klp98A$^{\Delta 47}$/Klp98A$^{\Delta 8}$*(25 °C).

Extended Data Fig. 3a, b: *w^{1118}* (25 °C). *w^{1118};UAS > Neur^{RNAi}/+;pnr > Gal4 UAS > DsRed Klp98A$^{\Delta 47}$/TM6B* (29 °C). *w^{1118};UAS > Neur^{RNAi}/+;pnr > Gal4 UAS > DsRed Klp98A$^{\Delta 47}$/Klp98A$^{\Delta 6}$* (29 °C; sibling of fly above).

Extended Data Fig. 3c: *Klp98A$^{\Delta 47/+}$: w^{1118};UAS > Neur^{RNAi}/+;pnr > Gal4 UAS > DsRed Klp98A$^{\Delta 47}$/TM6B* (29 °C; outside the *pnr* expression region). *pnr > Neur^{RNAi} Klp98A$^{\Delta 47/+}$: w^{1118};UAS > Neur^{RNAi}/+;pnr > Gal4 UAS > DsRed Klp98A$^{\Delta 47}$/TM6B* (29 °C; inside the *pnr* expression region). *pnr > Neur^{RNAi} Klp98A$^{\Delta 47/\Delta 8}$: w^{1118};UAS > Neur^{RNAi}/+;pnr > Gal4 UAS > DsRed Klp98A$^{\Delta 47}$/Klp98A$^{\Delta 8}$* (29 °C; inside the *pnr* expression region; sibling of fly above).

Extended Data Fig. 3d: *w^{1118}* (25 °C). *numb$^{2/SW}$ Klp98A$^{\Delta 47}$*/Jupiter–GFP: *w^{1118}(/+);Numb^{2}/Numb^{SW};Jupiter-GFP/Klp98A$^{\Delta 47}$* (25 °C). *numb$^{2/SW}$ Klp98A$^{\Delta 47/\Delta 8}$: w^{1118}(/+);Numb^{2}/Numb^{SW};Klp98A$^{\Delta 8}$/Klp98A$^{\Delta 47}$* (25 °C; sibling of the fly above). *pnr > numb^{RNAi} Klp98A$^{\Delta 47/+}$: w^{1118};pnr > Gal4 UAS > DsRed Klp98A$^{\Delta 47}$/UAS > numb^{RNAi}* (29 °C). *pnr > numb^{RNAi} Klp98A$^{\Delta 47/\Delta 8}$: w^{1118};pnr > Gal4 UAS > DsRed Klp98A$^{\Delta 47}$/Klp98A$^{\Delta 8}$ UAS > numb^{RNAi}* (29 °C).

Extended Data Fig. 3e: *numb$^{2/SW}$ Klp98A$^{\Delta 47}$*/Jupiter–GFP:*w^{1118}(/+);Numb^{2}/Numb^{SW};Jupiter-GFP/Klp98A$^{\Delta 47}$* (25 °C). *numb$^{2/SW}$ Klp98A$^{\Delta 47}$/Klp98A$^{\Delta 6}$: w^{1118}(/+);Numb^{2}/Numb^{SW};Klp98A$^{\Delta 6}$/Klp98A$^{\Delta 47}$* (25 °C; sibling of the fly above). *numb$^{2/SW}$ Klp98A$^{\Delta 47}$*/Jupiter–GFP: *w^{1118}(/+);Numb^{2}/Numb^{SW};Jupiter–GFP/Klp98A$^{\Delta 47}$* (25 °C). *numb$^{2/SW}$ Klp98A$^{\Delta 47}$/Klp98A$^{\Delta 8}$:w^{1118}(/+);Numb^{2}/Numb^{SW};Klp98A$^{\Delta 8}$/Klp98A$^{\Delta 47}$* (25 °C; sibling of the fly above). *numb$^{15/SW}$ Klp98A^{-}/+: w^{1118}(/+);Numb^{15}/Numb^{SW};Klp98A$^{\Delta 47}$/TM6B* (25 °C) or *w^{1118}(/+);Numb^{15}/Numb^{SW};Klp98A$^{\Delta 6}$/TM6B* (25 °C). *numb$^{15/SW}$ Klp98A$^{\Delta 47}$/Klp98A$^{\Delta 6}$:w^{1118}(/+);Numb^{2}/Numb^{SW};Klp98A$^{\Delta 6}$/Klp98A$^{\Delta 47}$* (25 °C; sibling of the fly above).

Extended Data Fig. 3f: *pnr > numb^{RNAi} Klp98A$^{\Delta 47}$/+: w^{1118};pnr > Gal4 UAS > DsRed Klp98A$^{\Delta 47}$/UAS > numb^{RNAi}* (29 °C). *pnr > numb^{RNAi} Klp98A$^{\Delta 47}$/Klp98A$^{\Delta 6}$: w^{1118};pnr > Gal4 UAS > DsRed Klp98A$^{\Delta 47}$/Klp98A$^{\Delta 6}$ UAS > numb^{RNAi}* (29 °C). *pnr > numb^{RNAi} Klp98A$^{\Delta 47}$/Klp98A$^{\Delta 8}$: w^{1118};pnr > Gal4 UAS > DsRed Klp98A$^{\Delta 47}$/Klp98A$^{\Delta 8}$ UAS > numb^{RNAi}* (29 °C).

Extended Data Fig. 4a–e: *w^{1118};Asense > GFP-Pon/Ubi > mCherry-Pavarotti* (25 °C). *w^{1118};Asense > GFP-Pon/Ubi > mCherry-Pavarotti;Klp98A$^{\Delta 47}$/Klp98A$^{\Delta 8}$* (25 °C).

Extended Data Fig. 4f–n: *w^{1118};Neur > Gal4, UAS > mRFP-Pon, Ubi > GFP-Pavarotti/+* (25 °C).

Extended Data Fig. 4o–v:*w^{1118};Neur > Gal4, UAS > mRFP-Pon, Ubi > GFP-Pavarotti/+* (25 °C).

Extended Data Fig. 4w: *w^{1118};Neur > Gal4, UAS > mRFP-Pon, Ubi > GFP-Pavarotti/+* (25 °C). *w^{1118};UAS > mRFP-Pon/+;Neur > Gal4, Jupiter-GFP/+* (29 °C).

Extended Data Fig. 4x: control: *w^{1118};Neur > Gal4, UAS > mRFP-Pon, Ubi > GFP-Pavarotti/+* (25 °C). *w^{1118};UAS > mRFP-Pon/+;Neur > Gal4, Jupiter-GFP/+* (29 °C). Patronin RNAi#1: *w^{1118};UAS > Patronin$^{RNAi\#1}$/+;Neur > Gal4,UAS > mRFP-Pon,Ubi > GFP-Pavarotti/+* (29 °C) and *w^{1118};UAS > Patronin$^{RNAi\#1}$/UAS > mRFP-Pon;Neur > Gal4, Jupiter-GFP/+* (29 °C). Klp10A RNAi: *w^{1118};Asense > mCherry-Pon/+;pnr > Gal4, Jupiter-GFP/UAS > Klp10A^{RNAi}* (29 °C). *Klp98A$^{\Delta 47}$/Klp98A$^{\Delta 8}$: w^{1118};Asense > GFP-Pon/Ubi > mCherry-Pavarotti; Klp98A$^{\Delta 47}$/Klp98A$^{\Delta 8}$* (25 °C).

Extended Data Fig. 4y: *w^{1118};Neur > Gal4, UAS > mRFP-Pon, Ubi > GFP-Pavarotti/+* (25 °C).

Extended Data Fig. 5a-b: *w^{1118};UAS > Jupiter-mCherry/+;Neur > Gal4, Ubi > GFP-Pavarotti/+* (25 °C).

Extended Data Fig. 5c: *w^{1118};UAS > Jupiter-mCherry/+;Neur > Gal4, UAS > mRFP-Pon, Ubi > Pavarotti-GFP/+* (25 °C).

Extended Data Fig. 5d–i: *w^{1118};Neur > Gal4, UAS > mRFP-Pon/+* (25 °C).

Extended Data Fig. 5j, k: control: *w^{1118};UAS > mRFP-Pon/+;Neur > Gal4, Jupiter-GFP/+* (25 °C). Lgl3A: *w^{1118};UAS > lgl3A/UAS > mRFP-Pon;Neur > Gal4, Jupiter-GFP/+* (25 °C).

Extended Data Fig. 5l, n: Jupiter–GFP: *w^{1118};UAS > mRFP-Pon/+;Neur > Gal4, Jupiter-GFP/+* (25 °C). GFP-Patronin and SiR-tubulin: *w^{1118};Neur > Gal4, UAS > mRFP-Pon/UAS > GFP-Patronin* (25 °C).

Extended Data Fig. 5m, n: Jupiter–GFP: *w^{1118};UAS > mRFP-Pon/+;Neur > Gal4, Jupiter-GFP/+* (25 °C). GFP–Patronin: *w^{1118};Neur > Gal4, UAS > mRFP-Pon/UAS > GFP-Patronin* (25 °C). SiR-Tubulin: *w^{1118};Neur > Gal4, UAS > mRFP-Pon, Ubi > GFP-Pavarotti/+* (25 °C).

Extended Data Fig. 5o, p: control: *w^{1118};UAS > mRFP-Pon/+;Neur > Gal4, Jupiter-GFP/+* (29 °C). Patronin RNAi: *w^{1118};UAS > Patronin$^{RNAi\#1}$/UAS > mRFP-Pon;Neur > Gal4, Jupiter-GFP/+* (29 °C). Klp10A RNAi: *w^{1118};Asense > mCherry-Pon/+;pnr > Gal4, Jupiter-GFP/UAS > Klp10A^{RNAi}* (29 °C).

Extended Data Fig. 5q, s: EB1–GFP and SiR-tubulin: *w^{1118};Ubi > mCherry-Pavarotti Neur > Gal4 tub > gal80^{ts}/UAS > EB1-GFP* (25 °C). Jupiter–GFP: *w^{1118};UAS > mRFP-Pon/+;Neur > Gal4, Jupiter-GFP/+* (25 °C). GFP–Patronin: *w^{1118};Neur > Gal4, UAS > mRFP-Pon/UAS > GFP-Patronin* (25 °C).

Extended Data Fig. 5r, s: EB1–GFP: *w^{1118};Ubi > mCherry-Pavarotti Neur > Gal4 tub > gal80^{ts}/UAS > EB1-GFP* (25 °C). Jupiter–GFP: *w^{1118};UAS > mRFP-Pon/+;Neur > Gal4, Jupiter-GFP/+* (25 °C). GFP–Patronin and SiR-tubulin: *w^{1118};Neur > Gal4, UAS > mRFP-Pon/UAS > GFP-Patronin* (25 °C).

Extended Data Fig. 6b, c: control: *w^{1118};UAS > mRFP-Pon/+;Neur > Gal4, Jupiter-GFP/+* (29 °C). Patronin RNAi#1: *w^{1118};UAS > Patronin$^{RNAi\#1}$/UAS > mRFP-Pon;Neur > Gal4, Jupiter-GFP/+* (29 °C).

Extended Data Fig. 6d–f: control: *w^{1118};UAS-mRFP-Pon/+;Neur > Gal4, Jupiter-GFP/+* (29 °C). Patronin RNAi#1: *w^{1118};UAS > Patronin$^{RNAi\#1}$/UAS > mRFP-Pon;Neur > Gal4, Jupiter-GFP/+* (29 °C). Patronin RNAi#2: *w^{1118};UAS > Patronin$^{RNAi\#2}$/UAS > mRFP-Pon;Neur > Gal4, Jupiter-GFP/+* (29 °C).

Extended Data Fig. 6g, h: GFP–Patronin: *w^{1118};Neur > Gal4, UAS > mRFP-Pon/UAS > GFP-Patronin* (25 °C). Patronin RNAi#1+ GFP-Patronin*: w^{1118};UAS > Patronin$^{RNAi\#1}$/+;Neur > Gal4, UAS > mRFP-Pon, UAS > GFP-Patronin/+* (29 °C).

Extended Data Fig. 6i, j: control: *w^{1118};UAS > mRFP-Pon/+;Neur > Gal4, Jupiter-GFP/+* (29 °C). Patronin RNAi#1: *w^{1118};UAS > Patronin$^{RNAi\#1}$/UAS > mRFP-Pon;Neur > Gal4, Jupiter-GFP/+* (29 °C). Klp10A RNAi: *w^{1118};Asense > mCherry-Pon/+;pnr > Gal4, Jupiter-GFP/UAS > Klp10A^{RNAi}* (29 °C). Klp10A RNAi + Patronin RNAi#1: *w^{1118};UAS > Patronin$^{RNAi\#1}$/UAS > mRFP-Pon;Neur > Gal4, Jupiter-GFP/UAS > Klp10A^{RNAi}* (29 °C).

Extended Data Fig. 7a–e: *w^{1118};UAS > Patronin$^{RNAi\#1}$/+;Neur > Gal4,UAS > mRFP-Pon, Ubi > GFP-Pavarotti/+* (29 °C).

Extended Data Fig. 7f: control: *w^{1118};Asense > GFP-Pon/Ubi > mCherry-Pavarotti* (25 °C). Patronin RNAi: *w^{1118};UAS > Patronin$^{RNAi\#1}$/UAS > mRFP-Pon;Neur > Gal4, Jupiter-GFP/+* (29 °C). Klp10A RNAi: *w^{1118};Asense > mCherry-Pon/+;pnr > Gal4, Jupiter-GFP/UAS > Klp10A^{RNAi}* (29 °C).

Extended Data Fig. 7g, h: control: *w^{1118};Neur > Gal4, UAS > mRFP-Pon/+* (29 °C). Patronin RNAi#1: *w^{1118};UAS > Patronin$^{RNAi\#1}$/+;Neur > Gal4, UAS > mRFP-Pon/+* (29 °C). Patronin RNAi#1 + GFP-Patronin: *w^{1118};UAS > Patronin$^{RNAi\#1}$/+;Neur > Gal4, UAS > mRFP-Pon, UAS > GFP-Patronin/+* (29 °C).

Extended Data Fig. 7i, j: control: *w^{1118};pnr > Gal4, phyllopod > GFP-Pon/+* (29 °C). Patronin RNAi#2: *w^{1118};UAS > Patronin RNAi #2/+;pnr > Gal4, phyllopod > GFP-Pon/+* (29 °C).

Extended Data Fig. 7k, l: control: *w^{1118};UAS > mRFP-Pon/+;Neur > Gal4, Jupiter-GFP/+* (29 °C). Patronin RNAi#1: *w^{1118};UAS > Patronin$^{RNAi\#1}$/UAS > mRFP-Pon;Neur > Gal4, Jupiter-GFP/+* (29 °C). Klp10A RNAi: *w^{1118};UAS > Jupiter-mCherry/+;pnr > Gal4, phyllopod > GFP-Pon/UAS > Klp10A^{RNAi}* (29 °C). Klp10A RNAi + Patronin RNAi#1: *w^{1118};UAS > Patronin$^{RNAi\#1}$/UAS > mRFP-Pon;Neur > Gal4, Jupiter-GFP/UAS > Klp10A^{RNAi}* (29 °C).

Extended Data Fig. 8c: *w^{1118};Neur > Gal4, UAS > mRFP-Pon/UAS > GFP-Patronin* (25 °C). *w^{1118};UAS > GBP-Pon/+;Neur > Gal4, UAS > mRFP-Pon/UAS > GFP-Patronin* (25 °C).

Extended Data Fig. 8d: control: *w^{1118};Neur > Gal4, UAS-mRFP > Pon/+* (25 °C). GFP–Patronin: *w^{1118};Neur > Gal4, UAS-mRFP > Pon/UAS > GFP-Patronin* (25 °C). GBP–Pon: *w^{1118};UAS > GBP-Pon/+;Neur > Gal4, UAS > mRFP-Pon/+* (25 °C). GBP–Pon+ GFP: *w^{1118};UAS > GBP-Pon/UAS > GFP;Neur < Gal4, UAS > mRFP-Pon/+* (25 °C). GBP–Pon+ GFP–Patronin: *w^{1118};UAS > GBP-Pon/+;Neur > Gal4,UAS > mRFP-Pon/UAS > GFP-Patronin* (25 °C).

Extended Data Fig. 8e: GFP–Patronin: *w*^{1118};*Neur > Gal4, UAS > mRFP-Pon/UAS > GFP-Patronin* (25 °C). GBP–Pon+ GFP–Patronin: *w*^{1118};*UAS > GBP-Pon/+;Neur > Gal4, UAS > mRFP-Pon/UAS > GFP-Patronin* (25 °C).

Extended Data Fig. 8f, g: control: *w*^{1118};*Neur > Gal4, UAS > mRFP-Pon/+* (25 °C). GBP–Pon+ GFP–Patronin: *w*^{1118};*UAS > GBP-Pon/+;Neur > Gal4, UAS > mRFP-Pon/UAS > GFP-Patronin* (25 °C).

Extended Data Fig. 8h: control: *w*^{1118};*Neur > Gal4, UAS > mRFP-Pon/+* (25 °C). GFP–Patronin: *w*^{1118};*Neur > Gal4, UAS > mRFP-Pon/UAS > GFP-Patronin* (25 °C). GBP–Pon: *w*^{1118};*UAS > GBP-Pon/+;Neur > Gal4, UAS > mRFP-Pon/+* (25 °C). GBP–Pon + GFP: *w*^{1118};*UAS > GBP-Pon/UAS > GFP;Neur-Gal4, UAS > mRFP-Pon/+* (25 °C). GBP–Pon + GFP–Patronin: *w*^{1118};*UAS > GBP-Pon/+;Neur > Gal4, UAS > mRFP-Pon/UAS > GFP-Patronin* (25 °C).

Extended Data Fig. 9a: *w*^{1118};*Neur > Gal4, UAS > mRFP-Pon/UAS-GFP-Patronin* (25 °C). *w*^{1118};*Neur > Gal4, UAS > GBP-mCherry-Pon/UAS-GFP-Patronin* (25 °C).

Extended Data Fig. 9c, d: *w*^{1118};*Neur > Gal4, UAS > mRFP-Pon/UAS > GFP-Patronin* (25 °C). *w*^{1118};*UAS > GBP-Pon/+;Neur > Gal4, UAS > mRFP-Pon/UAS > GFP-Patronin* (25 °C).

Extended Data Fig. 9e: *w*^{1118};*Neur > Gal4, UAS > mRFP-Pon/UAS > GFP-Patronin* (25 °C).

Extended Data Fig. 9f: *w*^{1118};*Neur > Gal4, UAS > mRFP-Pon/UAS > GFP-Patronin* (25 °C). *w*^{1118};*UAS > GBP-Bazooka/+;Neur > Gal4, UAS > mRFP-Pon, tub > gal80*^{ts}*/UAS > GFP-Patronin* (25 °C).

Extended Data Fig. 9g, h: *w*^{1118};*Neur > Gal4, UAS > mRFP-Pon/UAS > GFP-Patronin* (25 °C). *w*^{1118};*UAS > GBP-Pon/+;Neur > Gal4, UAS > mRFP-Pon/UAS > GFP-Patronin* (25 °C). *w*^{1118};*UAS > GBP-Bazooka/+;Neur > Gal4, UAS > mRFP-Pon, tub > gal80*^{ts}*/UAS > GFP-Patronin* (25 °C).

Extended Data Fig. 10b–f: *w*^{1118};*Neur > Gal4, UAS > mRFP-Pon, Ubi > GFP-Pavarotti/+* (25 °C).

Extended Data Fig. 10g: *w*^{1118};*Neur > Gal4, UAS > mRFP-Pon/UAS > GFP-Patronin* (25 °C). *w*^{1118};*UAS > GBP-Pon/+;Neur > Gal4, UAS > mRFP-Pon/UAS > GFP-Patronin* (25 °C).

Extended Data Fig. 10h, i: *w*^{1118};*Neur > Gal4, UAS > mRFP-Pon/UAS > GFP-Patronin* (25 °C). *w*^{1118};*UAS > GBP-Pon/+;Neur > Gal4, UAS > mRFP-Pon/UAS > GFP-Patronin* (25 °C). *w*^{1118};*UAS-mRFP-Pon/+;Neur > Gal4, Jupiter-GFP/+* (25 °C). *w*^{1118};*UAS > Patronin*$^{RNAi\#1}$*/UAS > mRFP-Pon;Neur > Gal4, Jupiter-GFP/+* (29 °C). *w*^{1118};*Asense > mCherry-Pon/+;pnr > Gal4, Jupiter-GFP/UAS > Klp10A*^{RNAi} (29 °C).

Most of these genotypes correspond to the F1 of crosses performed at 25 °C. Embryos were laid at 25 °C. Larvae were then shifted to 16 °C until puparium formation and 16 h before SOP imaging they were shifted to 25 °C or 29 °C, as indicated. In Extended Data Fig. 1a, k, larvae homozygous for the *Klp98A* mutants were used for western blot analysis instead of animals deriving from an outcross.

Plasmids. All the open reading frames (ORFs) cloned by PCR for this study were flanked by FseI and AscI sites for convenient shuttling between compatible plasmids. eGFP was amplified from pEGFP C1 (Clontech). *Pavarotti* (CG1258-PA), *Klp98A* (CG5658-PA), Bazooka (CG5055-PA) and *Patronin* (CG33130) were amplified from cDNAs prepared from adult *w*^{1118} flies total RNA extracted in TRIzol (Life Technologies), followed by reverse transcription (Super Script II kit, Life Technologies). The *Patronin* cDNA that we cloned encodes a splicing isoform slightly smaller than previously reported *Patronin* cDNAs[16,23] and has been deposited in the NCBI database (BankIt1865736 Patronin KT953618). The Pon localization domain (corresponding to amino acids 474–670 of Pon[35]) was similarly cloned from cDNA from *w*^{1118} flies. In various transgenes in this work (driven by UAS or Ase promoters), this Pon localization domain is referred to as 'Pon' for simplicity. Sara was subcloned from pUAST–GFP–Sara[42]. For antibody production, we also cloned smaller fragments of Patronin (corresponding to amino acids 1,039–1,384, named Patronin-Cter thereafter) and Klp98A (corresponding to amino acids 401–1,265, named Klp98A-Cter thereafter). Jupiter–mCherry was generated by cloning Jupiter–GFP from cDNA prepared from Jupiter–GFP flies[14] and by replacing the GFP (in the middle of the gene) by mCherry using site-directed mutagenesis. We also cloned the GFP-binding peptide (GBP), or so called GFP nanobody, a lama VHH single chain antibody against GFP[43] either for protein production (His–GBP) or for expression of fusion proteins in the fly (GBP–Pon and GBP–Bazooka, see below).

Klp98A–GFP–PC: for stable expression of Klp98A in S2 cells, the Klp98A ORF described above was subcloned into a modified pMT vector (Life Technologies), to which a Puromycin selection gene (amplified from the pCoPuro plasmid[44]) and a C-terminal tag (eGFP followed by PC, the Protein C epitope tag: EDQVDPRLIDG) were added.

GST–Klp98A-Cter, and GST–Patronin-Cter: for expression of GST–Klp98A-Cter and GST–Patronin-Cter in bacteria, the ORFs described above were subcloned into a modified pGEX vector[45].

His–Klp98A-Cter, His–eGFP, and His–GBP: for expression of $(His)_6$-tagged Klp98A-Cter, GFP and GBP, these ORFs were subcloned into a modified pET28b vector, which tags the ORF at its N terminus with a $(His)_6$ tag.

UAS > GFP–Patronin, UAS > Jupiter–mCherry, UAS > GBP–Pon, UAS > GBP–mCherry–Pon UAS > GBP–Bazooka, UAS > Klp98A–mCherry, UAS > Klp98A–GFP: for expression in flies with the UAS/Gal4 system, the Patronin, Bazooka, Klp98A, Pon localization domain and Jupiter–mCherry ORFs described above were subcloned into modified pUAST4 vectors tagging the ORF with either N-terminal PC–eGFP (for Patronin, referred to as GFP–Patronin for simplicity), C-terminal mCherry–PC (for Klp98A), C-terminal eGFP (for Klp98A), N-terminal GBP (for the Pon localization domain and Bazooka), N-terminal GBP–mCherry (GBP followed by mCherry separated by a GGG linker, for the Pon localization domain) or leaving it untagged (for Jupiter–mCherry). N-terminal GFP tagging of Patronin has been previously shown to be functional[16], as well as N-terminal tagging of Bazooka[46].

Ubi > mCherry–Pavarotti: for ubiquitous expression of mCherry–Pavarotti, Pavarotti was subcloned into a modified pUbi vector allowing the expression of mCherry–Pavarotti under the ubiquitin promoter.

Ase > GFP–Pon, Ase > GFP–Sara and Ase > mCherry–Pon: for specific expression in SOPs independently of the UAS/Gal4 system, the Pon localization domain and Sara were subcloned into the pAsense GFP vector, which was created by inserting a 1,943-bp fragment upstream of the start codon of the *Asense* gene (amplified from *w*^{1118} flies genomic DNA) into the Green Pelican GFP plasmid (*Drosophila* Genomics Resource Center), which results in tagging the Pon localization domain (or Sara) with an N-Terminal GFP (Ase > GFP–Pon). Alternatively, the GFP was exchanged by quick-change PCR into mCherry to generate the pAsense mCherry vector, in which the Pon localization domain was subcloned.

Injection of plasmids into *Drosophila* embryos to generate transgenics was performed by BestGene Inc.

SDS–PAGE and western blot. SDS–PAGE was performed using NuPAGE 4–12% Bis-Tris gels (Life Technologies) according to the manufacturer's instructions. Colloidal Coomassie blue (Life Technologies) was used for total protein staining of gels. Gels were transferred on nitrocellulose membranes using iBLOT (Life Technologies) according to the manufacturer's instructions. For western blot, we used all primary antibodies at 1 μg ml^{-1} in TBS, 0.2% BSA, 1 mM $CaCl_2$, 0.02% Thymerosal O/N at 4 °C. Western blots were revealed using HRP coupled antibodies (Jackson immunoResearch 1:10,000 dilution), Western Bright Quantum (Advansta) or SuperSignal West Pico (Pierce) chemiluminescence reagents and a Vilber Lourmat Fusion imager. Alternatively (Extended Data Fig. 6a), western blots were performed with fluorescently labelled anti-tubulin antibodies and imaged with an Ettan DIGE Imager (GE Healthcare). For gel source data, see Supplementary Fig. 1.

Fly and S2 cell total extracts. For total fly extracts (Extended Data Fig. 1a, k), dissected brains, imaginal discs and salivary glands of second instar larvae were squashed into 500 μl of lysis buffer (25 mM NaF, 1 mM Na_3VO_4, 50 mM Tris pH 7.5, 1.5 mM MgCl2, 125 mM NaCl, 0.2% IGEPAL, 5% glycerol, 1 mM DTT and protease inhibitor cocktail (benzamidine (1 mM, Applichem), chymostatine (40 μg ml^{-1}, Applichem), antipain (40 μg ml^{-1} Applichem), leupeptine (1 μM Applichem), pefabloc (1 mM) and PMSF (0.5 mM)). The extract was incubated 40 min at 4 °C with rocking, then cellular debris were cleared by centrifugation at 16,000*g* for 10 min at 4 °C. Extracts were then diluted in LDS sample buffer (Life Technologies) enriched with 2.5% β-mercaptoethanol and analysed by SDS–PAGE and western blot as above.

For RNAi-treated S2 total cell extracts (Extended Data Fig. 6a), *Drosophila* S2 cells (UCSF, mycoplasm-free judged by DAPI staining) were cultured and incubated with 5 μg dsRNA for 4 days as previously described[47]. This dsRNA sequence corresponds to the sequence in the *UAS > Patronin*$^{RNAi\#1}$ fly stock (VDRC no. 108927). Cells were washed in XB (20 mM HEPES, 150 mM KCl, pH 7.7), resuspended in LDS sample buffer, boiled for 2 min, then treated with Benzonase (30 units μl^{-1}, Sigma) and analysed by SDS–PAGE and western blot as above.

Protein purification. Unless stated otherwise, reagents were from Sigma. All purification steps were performed at 4 °C. Protein concentrations were determined spectrophotometrically using absorbance at 280 nm or after SDS–PAGE using purified BSA as a standard, followed by quantifications by densitometry using ImageJ (http://imagej.nih.gov/ij/).

GST- and His-tagged Klp98A-Cter were expressed in *E. coli* BL21 Rosetta 2 (Stratagene) by induction with 0.5 mM IPTG in Terrific Broth medium (Sigma) at 23 °C. Bacteria expressing GST–Klp98A-Cter were lysed enzymatically using 0.7 mg ml^{-1} lysosyme and 10 μg ml^{-1} DNase I (Roche) in lysis buffer (50 mM Tris, 150 mM NaCl, 1% Triton X-100, 1 mM DTT, 5% Glycerol, pH 7.6) enriched with protease inhibitors (Roche Mini) for 1 h at 4 °C with rocking. After clarification (12,000 r.p.m., Beckman JA 25.5), lysate was incubated with glutathione sepharose resin (glutathione sepharose 4B, Amersham) for 2 h at 4 °C and washed extensively

in 50 mM Tris, 2 mM β-mercaptoethanol, 100 mM NaCl, 5 mM $MgCl_2$ pH 7.5. Glutathione-sepharose-bound GST–Klp98A-Cter was then cleaved on column by an overnight incubation at 4 °C with 40 μg of TEV protease per mg of fusion protein. Klp98A-Cter was subsequently dialysed against PBS, concentrated to 1 mg ml^{-1} by ultrafiltration (Amicon Ultra-4 3k Millipore) and injected into rabbits for polyclonal antibody production (see Antibodies).

For affinity purification of polyclonal anti-Klp98A antibodies, we purified His–Klp98A-Cter following a protocol similar to the one described above, but using NiNTA resin (Ni Sepharose High Performance, Amersham) and 10 mM imidazole in lysis and wash buffers. His–Klp98A-Cter was eluted by 20 mM HEPES, 150 mM KCl, 300 mM imidazole, 1 mM DTT, pH 7.7, dialysed against 20 mM HEPES, 150 mM KCl, 10% glycerol, 1 mM DTT, pH 7.7, concentrated by ultrafiltration to 7.3 mg ml^{-1} and finally coupled to amino-link sepharose resin (Pierce).

His–GFP and His–GBP were expressed and purified from *E. coli* BL21 Rosetta 2 following the same procedure as for His–Klp98A-Cter. Final dialysis buffer was (20 mM HEPES, 150 mM NaCl, pH 7.7) for His–GFP and (20 mM HEPES, 150 mM NaCl, 5% glycerol, 15 mM imidazole, pH 7.7) for His–GBP. His–GFP and His–GBP were concentrated by ultrafiltration to 7.5 mg ml^{-1} and 2.34 mg ml^{-1}, respectively, flash frozen in liquid N_2 and kept at −80 °C.

GST-tagged Patronin-Cter purification was similar to the one of GST–Klp98A, except that TEV was removed by using NiNTA resin before final dialysis. Tag-free Patronin-Cter was injected into rabbits for polyclonal antibody production. Alternatively, tag-free Patronin-Cter was coupled to amino-link sepharose resin for affinity purification these anti-Patronin antibodies (see Antibodies).

Klp98A–GFP–PC (that is, full length Klp98 fused to GFP and the PC tag in Cter) was purified from a puromycin-resistant Schneider S2 stable cell line expressing Klp98A–GFP–PC under the inducible metallothionein promoter. To obtain this cell line, S2 cells were transfected with pMT Puro Klp98A–GFP–PC plasmid (see above) using Effectene (Qiagen). This stable cell line was subsequently grown and selected in Schneider medium (Life Technologies) enriched with 10% vol/vol fetal calf serum and 5 μg ml^{-1} puromycin (Applichem). The concentration of inducer ($CuSO_4$) was subsequently gradually increased from 0.05 mM to 0.6 mM over 1 month so as to select clones able to express high amounts of Klp98A (whose overexpression is toxic). We then grew 100 15-cm plates of this pseudo-clone. Cells were harvested, washed in XB buffer (20 mM HEPES, 150 mM KCl, 1 mM $CaCl_2$, pH 7.7) then lysed in 100 ml of lysis buffer (20 mM HEPES, 150 mM KCL, 1% Triton X-100, 1 mM $CaCl_2$, 2 mM $MgCl_2$, 0.1 mM ATP, pH 7.2) supplemented with a protease inhibitor cocktail (benzamidine/chymostatine/antipain/leupeptine/pefabloc/PMSF, see SDS–PAGE and western blot section). Lysate was rocked for 1 h at 4 °C to ensure microtubule depolymerization. Cell debris were removed by centrifugation at 3,300*g* for 10 min at 4 °C in a swinging bucket rotor (Heraeus Megafuge) followed by an ultracentrifugation at 200,000*g* for 30 min at 4 °C (Beckman Ti 60). Clarified lysate was subsequently incubated with 1 ml of pre-equilibrated Protein C affinity resin (Roche) for 4 h at 4 °C with recirculation. The column was then washed extensively with 50 ml lysis buffer, then with 50 ml of Klp98A buffer (20 mM HEPES, 150 mM KCL, 2 mM $MgCl_2$, 0.1 mM ATP, 10% glycerol, pH 7.2) enriched with 1 mM $CaCl_2$, followed by 50 ml Klp98A buffer. Elution was then performed by incubating the 1 ml resin with 1 ml of Klp98A buffer enriched with 5 mM EGTA overnight at 4 °C with rocking. Eluted Klp98A–GFP–PC was then mixed with Klp98A buffer enriched with 2 mM DTT in a 50:50 volume ratio, concentrated by ultrafiltration (Amicon Ultra-4 3k Millipore), and further purified by gel filtration on a Superdex 200 10/300 column (GE Healthcare Life Sciences) in (20 mM HEPES, 0.15 M KCl, 2 mM $MgCl_2$, 1 mM DTT, 0.1 mM ATP, pH 7.2) at 0.25 ml min^{-1}. Fractions containing Klp98A–GFP–PC were pooled, mixed with Klp98A buffer containing 20% glycerol final in a 50:50 volume ratio, concentrated by ultrafiltration (Amicon Ultra-4 3k Millipore), flash frozen in liquid N_2 and finally kept at −80 °C (Fig. 1b). Final Klp98A–GFP–PC buffer is (20 mM HEPES, 150 mM KCL, 2 mM $MgCl_2$, 0.1 mM ATP, 10% glycerol, 1 mM DTT pH 7.2). For motility assays were a high concentration of Klp98A–GFP–PC was critical to achieve a high density of Klp98–GFP–PC on the quantum dots, the gel filtration step was omitted.

Unlabelled porcine tubulin or HiLyte488- and rhodamine-labelled porcine tubulin were purchased from Cytoskeleton, reconstituted at 10 mg ml^{-1} in BRB80 buffer (80 mM K-Pipes, 1 mM $MgCl_2$ pH 6.9) supplemented with 1 mM GTP (Roche) or 1 mM GMPPCP (Jena Bioscience), flash frozen in liquid N_2 and kept at −80 °C.

GFP–MAP65-1 was a gift from V. Stoppin-Mellet, M. Vantard and J. Gaillard (ref. 13).

Fly notum live imaging, Delta antibody uptake and SiR-tubulin imaging. Fly notum dissection and SOP imaging was performed in clone 8 medium after embedding into a fibrinogen clot[48,49] in order to diminish tissue movements during fast 3D image acquisition as described[50].

Fluorescent Delta antibody uptake to label the Sara endosomes was performed as previously described[1,50] with a 5-min pulse (3.4 μg ml^{-1} antibody in clone 8) and a 20-min chase (referred to as $iDelta_{20}$). To address antibody bleaching, which hampers the accuracy of endosome tracking during acquisition, we replaced the original primary anti-Delta antibody coupled to a fluorescent Fab[1,50] by a primary anti-Delta antibody covalently coupled to the very stable Atto647N dye (see Antibodies). Under these labelling conditions, no bleaching is detectable (Extended Data Fig. 4n).

For SiR-tubulin imaging, dissected nota were incubated in clone 8 medium enriched with 1 μM SiR-tubulin[15] (Spirochrome) for 30 min at room temperature, then washed twice in clone 8 before fibrinogen clot embedding as above and imaging. Note that SiR-tubulin is less excluded from the Pavarotti-positive central spindle core than Jupiter–mCherry (Fig. 3a).

For imaging of Sara endosomes dynamics *in toto* with neither iDelta uptake nor notum dissection (Extended Data Fig. 2c–h), pupae were mounted as described by Jauffred and Bellaïche[51]. Drift along the *z* axis resulting from muscle contractions was corrected by manually adjusting the focus during the acquisition. Compared to the signal in the primary culture preparation upon an antibody uptake, this *in toto* preparation shows a lower signal-to-noise ratio owing to the glow signal generated by the tissues underneath the epithelium of the epidermis. To address this, and only for visualization purposes, in Extended Data Fig. 2f, g we processed the images with a wavelet *à trous* filter (ImageJ plugin 'Kymo Toolbox' developed by Fabrice Cordelières).

Imaging was performed using a 3i Marianas spinning disk confocal setup based on a Zeiss Z1 stand, a 63× PLAN APO NA 1.4 objective and a Yokogawa X1 spinning disk head followed by a 1.2× magnification lens and an Evolve EMCCD camera (Photometrics). Fast *z*-stack acquisition of entire SOP cells (0.5-μm steps) was obtained using a piezo stage (Mad City Labs). Single-emitter emission filters were always used to avoid bleed-through and each channel was acquired sequentially. To increase acquisition speed for $iDelta_{20}$ endosome tracking, we acquired 3D stacks spanning only 3 μm along the *z* axis (with 0.5-μm steps), which is usually sufficient to contain most of the central spindle (and sufficient to distinguish particles along the *z* axis, given the PSF of the microscope at this wavelength). In addition, the Pavarotti channel was acquired once every 20 time points. The strong brightness of the Atto647N dye allowed us to perform 3D acquisition at 1.3 Hz on average. Unless stated otherwise, data presented in figure panels correspond to maximum-intensity projections.

Fly notum and S2 cells immunofluorescence. Dissected fly nota were fixed according to a method designed to preserve the microtubule cytoskeleton[52]. In brief, nota were first incubated in Hank's balanced salt solution (Gibco) enriched with 1 mM DSP (Pierce) for 10 min at room temperature followed by a 10 min incubation in MTSB (microtubule stabilization buffer: 0.1 M PIPES, 1 mM EGTA, 4% PEG 8000, pH 6.9) enriched with 1 mM DSP, then finally in MTSB enriched with 4% PFA (Electron Microscopy Science). Nota were then permeabilized in MTSB enriched with 4% PFA and 0.2% Triton X-100 then processed for immunofluorescence as described[1] and mounted in Prolong Gold anti-fade reagent (Molecular Probes). Unlabelled and fluorescently labelled (see Antibodies) primary antibodies were used at 1 μg ml^{-1}. When non-labelled primary antibodies were used, we added Alexa647- and Alexa488-coupled secondary antibodies (Life Technologies) at a 1:500 dilution.

For lineage staining (Extended Data Fig. 3c), fly nota were dissected 30 h after puparium formation and processed for immunofluorescence as above using primary rat anti-Elav at 22 μg ml^{-1} antibodies followed by Cy5-coupled secondary antibodies (Biozol) at a 1:100 dilution.

For S2 cells immunofluorescence (Extended Data Fig. 6b), cells were plated onto glass coverslips pre-coated with Concanavalin A (Sigma, 0.05 mg ml^{-1} in water for 1 h) for 1 h at 25 °C in Schneider medium enriched with 10% serum. Cells were then fixed with 4% PFA (Electron Microscopy Science) for 20 min, then processed for immunofluorescence using standard techniques with Oregon-green 514-anti α-tubulin antibodies at 1 μg ml^{-1} final (see Antibodies). Coverslips were mounted in Prolong Gold anti-fade reagent.

Image acquisition was performed on the 3i Spinning disk confocal microscope described above, but using a 100× PLAN APO NA 1.45 TIRF objective and a *z* step of 0.27 μm for optimal sampling along the *z* axis. Alternatively, for Extended Data Fig. 3c, images were taken on this setup using a 40× PLAN APO NA 1.3 objective and a Photometrics HQ2 CCD camera.

Fly notum preparation for co-localization analysis. For co-localization studies of $iDelta_{20}$ with GFP–Sara (Extended Data Fig. 2a, b) and of Klp98–mCherry with GFP–Sara, $iDelta_{20}$, GFP–Rab5 knock-in and YFP–Rab7 knock-in (Extended Data Fig. 1c–e), dissected fly nota embedded in the fibrinogen clot were fixed using 4% PFA in PEM buffer (80 mM K-Pipes, 5 mM EGTA, 1 mM $MgSO_4$, pH 6.95) for 20 min at room temperature, then washed three times with PEM and imaged in PEM. Image acquisition was performed on the 3i Spinning disk confocal microscope described above with the 100× PLAN APO NA 1.45 TIRF objective, a *z* step of 0.27 μm and both channels were acquired sequentially at each *z* plane. Cells at various stages of the cell cycle were included into the analysis.

Since signal of YFP–Rab11 at endogenous levels (knock-in) was lost upon fixation in our conditions, co-localization between Klp98–mCherry and YFP–Rab11 was addressed in living tissue (acquiring only one *z* plane, to address fast 3D movements of the endosomes).

Antibodies. Polyclonal rabbit anti-Klp98A antibody was generated by injecting rabbits (Eurogentec Speedy program) with cleaved GST–Klp98A-Cter (see Protein purification). Immunized serum was subsequently affinity-purified with sepharose-bound His–Klp98A-Cter using standard glycine (0.1 M, pH 3.0) elution. Eluted antibody was subsequently dialysed against PBS then PBS-50% glycerol for storage at −20 °C. The characterization of this antibody is presented in Extended Data Fig. 1a, b. Polyclonal rabbit anti-Patronin antibody was generated using the same protocol. Its characterization is provided in Extended Data Fig. 6a.

Mouse anti-Delta monoclonal antibodies (C594.9B, Developmental Studies Hybridoma Bank) were purified on a Protein G column (Pierce) from hybridoma culture supernatant obtained by cultivating the hybridoma in CELline devices (Integra) using RPMI medium (Gibco) supplemented with 10% ultra-low IgG fetal calf Serum (Gibco) and 1% pen-strep (Gibco). Antibodies were subsequently dialysed against fresh 0.15 mM sodium bicarbonate pH 8.3, concentrated to 4.11 mg ml^{-1} and labelled with NHS-Atto 647N (Atto tech) in a 5× molar excess of dye for 2 h in the dark at room temperature. Free dye was subsequently removed by gel filtration on a G-25 fine column (Sigma) in PBS. Degree of labelling was measured spectrophotometrically to be 2.6.

Oregon Green 514-labelled mouse anti-β-tubulin (E7, Developmental studies hybridoma bank), Oregon Green 514-labelled mouse anti-α-tubulin (12G10, Developmental studies hybridoma bank) and Atto-647N-labelled anti-α K40 acetylated tubulin (C3B9, HPA Cultures) were purified and labelled in a similar fashion. Degree of labelling was measured spectrophotometrically to be 2.7 for Oregon Green 514-labelled anti-β-tubulin, 1 for Oregon Green 514 labelled anti-α-tubulin, and 1.6 for Atto-647N labelled anti-acetylated tubulin.

Biotinylated GBP was obtained by *in vitro* biotinylation of purified GBP (see protein purification, or purchased from Chromoteck) with EZ-Link SulfoNHS biotin (Pierce) in a 1:5 ratio followed by extensive dialysis (SnakeSkin 3kD MWCO, Pierce) against PBS.

All labelled antibodies were subsequently frozen in liquid N_2 and kept at −80 °C. Mouse anti-PC (clone HPC4) antibodies were from Roche. Rat anti-Elav (7E8A10) was from Developmental studies hybridoma bank. Unlabelled mouse anti-β-tubulin (E7) was also used for loading controls in western blots.

***In vitro* motility assays.** General tubulin handling as well as preparation of GMPPCP-stabilized, Taxol-stabilized and polarity marked fluorescent microtubules were performed accordingly to the protocols of the Mitchison laboratory (http://mitchison.med.harvard.edu/protocols.html). GTP and GMPPCP microtubules were polymerized at 5 mg ml^{-1} for 20 min at 37 °C in a water bath. Unpolymerized fluorescent tubulin dimers were removed by ultracentrifugation over a glycerol cushion. Motility assays of Klp98A were performed using purified full length Klp98A–GFP–PC (that is, full length Klp98A fused to GFP and the PC tag in Cter; see Protein purification).

Imaging of motility assays were performed using a 3i TIRF microscope based on a Zeiss Z1 stand equipped with a TIRF Slider 3 module. Excitation was performed with a 488 nm laser and simultaneous detection of both microtubules and quantum dots (Qdots) was performed using a Dualview device (Photometrics) equipped with a 565dcxr dichroic (Chroma) and two emission filters (520/30 and 630/50, Chroma) in front of an EMCCD camera (Cascade II 512, Photometrics) at 6.66 Hz. The motility properties of Klp98A-bound Qdots were analysed on kymographs using the ImageJ plugin 'Kymo Toolbox' developed by Fabrice Cordelières. This plugin was also used to process images from the Qdot channel with a wavelet *à trous* filter for representation purposes (Supplementary Video 5). Motility of Klp98A-bound Qdots was analysed as described[53] with the following modifications. In brief, glass coverlips (Agar Scientific) were cleaned using a plasma cleaner (Harrick_plasma) and assembled into a flow chamber using sticky slides (sticky-Slide VI 0.4 Luer, Ibidi). This flow chamber was connected to an Aladdin Syringe Pump (World Precision Instrument) used to change gently the solution in the chamber. The chamber was first perfused with anti-tubulin antibodies (SAP4G5, Sigma, 1/100 dilution in BRB80) for 5 min, then passivated using four chamber volumes of 0.1 mg ml^{-1} PLL-PEG (Susos) in BRB80 for 5 min followed by four chamber volumes of 0.5 mg ml^{-1} K-Casein (Sigma) in BRB80 for 5 min. A dilute solution of Taxol- or GMPPCP-stabilized microtubules (0.05 mg ml^{-1}, 5% labelled with HiLyte 488) were then injected and let to adhere to the antibodies for 10 min. The chamber was then washed with four chamber volumes of imaging buffer (BRB80 enriched with 0.25 mg ml^{-1} K-casein, 1 mM ATP, 40 mM DTT, 20 μg ml^{-1} catalase, 160 μg ml^{-1} glucose oxydase and 40 mM D-glucose). Klp98A–GFP–PC (3 μM) was pre-incubated with 1.5 μM of biotinylated GBP for 5 min, before mixing in a 10:1 molar ratio with strepavidin-coated Qdots 605 (Molecular Probes). This ensured a high density of motors per Qdot, thus mimicking a bead assay, although bead diameter is small. These Klp98A-bound Qdots were then injected in the flow chamber in imaging buffer.

Gliding assays of polarity-marked microtubules (Fig. 1c) were performed using the same flow chamber described above. Polarity-marked microtubules were obtained by elongating short bright GMPPC microtubule seeds (5 mg ml^{-1}, 30% rhodamine labelled) with a dimmer tubulin mix (1.5 mg ml^{-1}, 5% rhodamine labelled) followed by stabilization with 20 μM Taxol. The chamber was first perfused with Klp98A–GFP–PC (2.9 μM) then passivated with PLL-PEG as above. Polarity-marked Taxol-stabilized microtubules were then injected and let to adhere to Klp98A for 5 min. The chamber was then washed with two chamber volumes of imaging buffer enriched with 20 μM Taxol then imaged in the same buffer. As seen in Fig. 1c, the minus-end (short) is leading in these gliding assays, indicating that Klp98A is a plus-end motor.

For motility of Klp98A-bound Qdots on antiparallel arrays of microtubules, antiparallel bundles were generated by incubating 50 nM GMPPCP microtubules (5% rhodamine-labelled) with 6.5 nM of GFP–MAP65-1[13] for 5 min at room temperature. These bundles were injected into the chamber and moving Klp98A-bound Qdots were observed as before using a 561 nm laser to excite rhodamine and a 405 nm laser to excite the Qdots 605. Due to the excess of Klp98A–GFP–PC over GBP–biotin in this assay, it is likely that all available GFP-binding sites of the Qdots are saturated, thus the presence of GFP-tagged MAP65-1 is not an issue.

For the analysis of the frequency at which Qdots change direction, we only considered antiparallel overlaps composed of two microtubules. We first identified pauses in the motility of Qdots (a pause is defined by a Qdot immobile for at least three consecutive frames, which corresponds to 0.9 s). Then we scored the incidence of changes of direction after a pause, in order to compute the frequency of direction changes.

Liposome flotation assay. Liposome flotation assays were performed as described[45] with the following modifications. Small unilamellar vesicles (SUVs) were prepared by N. Chiaruttini in BRB80 buffer by sonication in a water bath with several lipid mixtures: DOPC:DOPS 90:10; DOPC:DOPS:PI(3)P 80:10:10; DOPC:DOPS:PI(4)P 80:10:10 and DOPC:DOPS:PI(5)P 80:10:10. All lipid mixtures were doped with 0.6% rhodamine phosphatidylethanolamine (PE). 70 μl of SUVs (1 mg ml^{-1}) were incubated with 5 μl Klp98A–GFP–PC (0.05 mg ml^{-1}) for 30 min at room temperature. Then 50 μl of 2.5 M sucrose in BRB80 was added and gently mixed. 100 μL of this solution was poured into a polyallomer tube (Beckman Coulter), and then overlaid with 100 μL of 0.75 M Sucrose in BRB80 then with 20 μL of BRB80. This discontinuous sucrose gradient was then ultracentrifuged at 100,000 r.p.m. for 20 min in a TLA 100.4 rotor (Beckman Coulter) at 25 °C with acceleration and deceleration settings set to level 5. The top 50 μl of the gradient, referred to as the 'floating fraction', was subsequently collected and liposome recovery was quantified by measuring rhodamine fluorescence using a Spectramax I3 plate reader (Molecular Devices). Equal amounts of recovered SUVs were then loaded onto a SDS–PAGE gel followed by western blot against the PC tag to analyse protein co-flotation with the SUVs. As controls, we also loaded samples devoid of liposomes as well as the input before centrifugation (Extended Data Fig. 1f).

Scanning electron microscopy (SEM). Flies were euthanized by exposure to diethyl ether for 20 min, then mounted on SEM holders using double-sided carbon tape (Electron Microscopy Sciences) and subsequently treated with a gold sputter coater (JFC-1200, JEOL). Imaging was performed using a JEOL JSM-6510LV scanning electron microscope operating in high-vacuum mode using a working distance of 10 mm and an acceleration of 10 kV. Alternatively, for Extended Data Fig. 3a, imaging was performed using a JEOL 7600F scanning electron microscope using a working distance of 25 mm and an acceleration of 5 kV.

Rationale and quantification of the *Neur* and *Numb* phenotypes. *Rationale.* Two endocytic factors play major, independent roles during asymmetric Notch signalling in the SOP: Neuralized and Numb (reviewed in ref. 8). In Neuralized mutants, cells in the lineage become neurons and, conversely, in Numb mutants they become sockets. It has previously been shown that Neuralized complete loss of function causes a full conversion of all the SOP lineage into neurons leading to a bald notum cuticle[54,55]. However, a partial depletion of Neuralized in the centre of the notum ($pnr > neur^{RNAi}$) allows many sensory organs to perform asymmetric cell fate assignation and to develop, as in wild type, into structures containing at least the two external cells (shaft and socket; Fig. 1i, j, Extended Data Fig. 3a, b).

Klp98A mutants reveal that the lineages which generated bristles in $pnr > neur^{RNAi}$ need Klp98A function to perform asymmetric cell fate assignation: in Klp98A^{-}, $pnr > neur^{RNAi}$ double mutants, these lineages failed to perform asymmetric signalling, causing the notum to be largely bald (Fig. 1i, j, Extended Data Fig. 3a, b). This was confirmed with two independent Klp98A mutants. Conversely, these two different Klp98A mutant conditions in combination with three alternative hypomorphic mutant conditions for Numb ($Numb^{SW}/Numb^{2}$, $Numb^{SW}/Numb^{15}$ or pnr-gal4 driving $Numb^{RNAi}$) all show a strong suppression (by half) of the multiple socket phenotype diagnostic of Numb mutants[9]

(Extended Data Fig. 3d–f). All together, these experiments demonstrate the role of Klp98A motility in Notch signalling.

Quantification. To quantify these cell-fate phenotypes in the SOP lineage in *Neuralized*^{RNAi} mutants (Fig. 1i, j and Extended Data Fig. 3a, b), we manually scored in each genotype the number of organs within the region between the left and right pairs of dorso-central macrochaetes (which corresponds to the *panier* expression region) at the dissecting scope or on SEM images. To focus on lineage specification phenotypes generated by cell-fate specification failures in the SOP division, we scored lineages which generated organs composed of one-shaft/one-socket or two-shafts. In these organs, the SOP division seems to have been normal and thereby generated a pIIa (and a pIIb cell). 'Tufts', which are characteristic of neuralized mutant phenotype, could be caused by SOP specification defects and were therefore excluded from the analysis.

We verified that the absence of lineages generating bristles in the *pnr* > *neur*^{RNAi}, *Klp98A*$^{\Delta 8}$/*Klp98A*$^{\Delta 47}$ double mutant conditions are not due to an earlier, SOP specification problem. The question is whether, in the double mutant condition, the notum is bald because SOPs were specified and the lineage has all been converted into neurons or, alternatively, whether SOPs were not specified in the first place. Immunostaining with a neural specific marker (elav) confirmed that, below the bald cuticle, clusters of elav-positive neurons are present like in the control animals (Extended Data Fig. 3c).

To quantify cell-fate phenotypes in the SOP lineage in *Numb* mutants (Extended Data Fig. 3d–f), we manually scored on SEM images the number of organs showing multiple sockets (that is, Notch gain-of-function phenotype) in the dorsal-most region of the notum (between the left and right pairs of dorsocentral bristles) both in mutant and control flies and calculated the percentage of affected organs in each genotype.

Flurescence lifetime imaging microscopy (FLIM). Lifetime imaging of GFP–Patronin was performed on a setup composed of an Olympus IX81 stand, a 60× NA 1.42 oil objective, a FV1000 confocal scanner head and time-correlated single-photon counting (TCSPC) hardware from Picoquant. Illumination was achieved with a pulsed 485 nm laser (Picoquant) operating at 40 Mhz, and detection was performed on a gated PMA hybrid 40 detector (Picoquant) behind a 520/35 nm bandpass filter (Semrock). Data analysis was performed using SymPhotime 2.0 software (Picoquant). GFP fluorescence lifetime was fitted to a dual exponential model after deconvolution for the instrument response function (measured using fluorescein in the presence of saturating potassium iodine). The lifetime reported in images and graphs corresponds to the intensity-weighted average lifetime.

To measure the lifetime of GFP, we incubated 10 µl of TALON beads (Clontech) with 37.5 µg of purified His–GFP (see protein purification) in 10 µl clone 8 medium for 3 h at room temperature. After two washes in Clone 8 medium, we mounted the beads on a coverslip in 50 µl clone 8 and measured the intensity-weighted average lifetime in a region of interest (ROI) encompassing each bead by FLIM, followed by averaging over several beads.

Similarly, to measure the lifetime of GFP in conditions where 100% of the molecules are bound to the GFP–nanobody (GBP), we incubated 10 µl streptavidin beads (GE healthcare) with 18 µg of biotinylated GBP (see Antibodies) for 10 min at room temperature. After extensive washing of unbound GBP, the resulting GBP-bound beads were incubated with 37.5 µg of purified His–GFP in 10 µl clone 8 medium for 3 h at room temperature. After two washes in clone 8 medium, the lifetime of GBP-bound GFP was measured as above. Alternatively, we used GFP-trap beads from Chromoteck, in which the GBP is directly cross-linked to beads. This gave similar values of increased GFP lifetime: $\tau = 2.627 \pm 0.006$ ns; $n = 15$ for the GBP-biotin/Streptavidin beads versus $\tau = 2.678 \pm 0.004$ ns; $n = 10$ for the GFP-Trap beads (GBP-free GFP has a lifetime of $\tau = 2.531 \pm 0.003$ ns; $n = 29$). Please note that for all FLIM measurements, either of purified GFP *in vitro* or of GFP–Patronin fusion in the fly, the term GFP refers to the enhanced GFP variant (eGFP).

Fluorescence recovery after photobleaching (FRAP). FRAP of GFP–Patronin (Extended Data Fig. 9e) was performed on the 3i Marianas spinning disk setup described above (63× NA 1.4 oil objective) equipped with a Micropoint Photomanipulation hardware driven by Slidebook 6.0. A region of interest (ROI) was drawn onto half of the mitotic spindle, bleached, and recovery was monitored by spinning disk confocal imaging at a frame-rate of 14.3 Hz (50 ms exposure, 20 ms transfer time). Owing to the fast recovery of GFP–Patronin (timescale of few seconds), recovery was monitored in 2D (that is, one z plane) to maximize frame-rate.

FRAP movies were processed as follows: signal background was first removed homogenously using a ROI outside the cell as a reference, then, bleaching was corrected homogenously using the first frame as a reference. GFP–Patronin signal within the bleached ROI was then integrated overtime. Intensity was then normalized using the formula:

$$I_{\mathrm{norm}}(t) = \frac{I(t) - I_{\mathrm{postbleach}}}{I_{\mathrm{prebleach}} - I_{\mathrm{postbleach}}}$$

With $I(t)$, the integrated intensity at time point t; $I_{\mathrm{postbleach}}$, the intensity just after bleaching, and $I_{\mathrm{prebleach}}$ the intensity before bleaching (averaged over five time points).

Normalized intensity was then fitted to the equation:

$$I_{\mathrm{norm}}(t) = A(1 - \mathrm{e}^{-t\tau})$$

In this equation, A corresponds to the immobile fraction, the half-time of recovery is provided by $t_{0.5} = \frac{-\ln(0.5)}{\tau}$ and τ is an estimate of the k_{off} of GFP–Patronin for mitotic spindle microtubules (assuming that diffusion is faster than binding/unbinding kinetics). Averaging the values of A, $t_{0.5}$, and k_{off} for each curve gave similar results than the values obtained by fitting the average recovery: $A = 0.90 \pm 0.01$, $t_{0.5} = 1.3 \pm 0.1$ s and $k_{\mathrm{off}} = 0.53 \pm 0.03\,\mathrm{s}^{-1}$, $n = 11$ for average of the individual fits versus $A = 0.89 \pm 0.02$, $t_{0.5} = 1.31 \pm 0.03$ s and $k_{\mathrm{off}} = 0.53 \pm 0.01\,\mathrm{s}^{-1}$ for fit of the average curve (95% confidence intervals).

Image analysis. Unless otherwise specified, image analysis was performed using custom codes written for ImageJ and Matlab (Mathworks), available on request. For representation purposes, intensity was sometimes colour-coded using the Rainbow or the Red Hot lookup tables in ImageJ. Videos were edited using Adobe Premiere Pro CS6.

Co-localization. To automatically measure the co-localization between iDelta$_{20}$ and GFP–Sara (Extended Data Fig. 2), as well as the co-localization between Klp98A–mCherry and various early endosome markers (Extended Data Fig. 1c, d), we developed a custom object-based method to determine the percentage of co-localization of signals detected in two different channels. Indeed, the fact the membrane of endosomes is organized as a mosaic of domains[56–58] implies that the corresponding signals only partially overlap, which explain why classical co-localization methods relying on intensity correlation coefficients perform poorly in the case of endosomes. On the other hand, object-based methods rely on the segmentation of the signals in both channels followed by the measurements of the distances between all the objects: two objects are considered co-localized if the distance between their fluorescence centroid is below a certain threshold r_{ref} (ref. 59).

Current endosome segmentation methods rely on an intensity threshold for the fluorescent signal[59]. This is problematic when the signal intensity in different endosomes is heterogeneous (that is, to take dim endosomes into account, bright endosomes are over-segmented, and vice-versa). To avoid this issue, we adapted to 3D a threshold-free method for endosome segmentation, which is based on Gaussian fitting. In brief, signal-positive particles in both channels are first detected in 2D in each z plane by a 2D Gaussian fitting algorithm[60], which does not rely on an intensity threshold, but rather on the fact that particles are characterized by fluorescent signals with a spatial Gaussian distribution with an offset which correspond to the local background. Then, the particles detected in each plane (2D), but corresponding to the same object in 3D, are connected based on the point spread function (PSF) of the microscope. From this, the 3D coordinates of the centroid of fluorescence of all the particle is determined in each channel.

Once this automated detection ('segmentation') has been performed in the two channels, the distance d_{AB} between all particles in 3D in the two channels (A and B) are computed and compared to a reference distance r_{ref}. If $d_{AB} < r_{\mathrm{ref}}$, the particles detected in the two channels do co-localize.

When considering 2D data, r_{ref} is routinely set to be the lateral resolution of the microscope $resol_{xy}$ (ref. 59). However, in 3D, since the axial ($resol_z$) and lateral ($resol_{xy}$) resolutions of the microscope are not equal, the reference distance r_{ref} has to take into account the relative position of the two particles in 3D. For instance, if the two particles are on the same z plane, then r_{ref} has to be $resol_{xy}$ and conversely, if the two particles are on different z planes, but have identical x and y coordinates, then r_{ref} has to be $resol_z$. Following a method implemented by Cordelières and Bolte in the ImageJ plugin JACop 2.0 (ref. 59), we calculated r_{ref} for the 3D problem using the following equations:

$$\Phi = \arccos\frac{(x_B - x_A)}{\sqrt{(x_B - x_A)^2 + (y_B - y_A)^2}} \text{ and}$$

$$\Theta = \arccos\frac{(z_B - z_A)}{\sqrt{(x_B - x_A)^2 + (y_B - y_A)^2 + (z_B - z_A)^2}}$$

$$r_{\mathrm{ref}} = \sqrt{(resol_{xy}\ \sin\Theta\ \cos\Phi)^2 + (resol_{xy}\ \sin\Theta\ \sin\Phi)^2 + (resol_z\ \cos\Theta\ )^2}$$

Here, x_A, y_A, z_A and x_B, y_B, z_B are the 3D coordinates of particles in channel *A* and *B*, respectively, and $resol_{xy}$ and $resol_z$ correspond to the lateral and axial resolutions of the microscope, respectively. For our analysis, we measured $resol_z = 0.9\,\mu m$ and $resol_{xy} = 0.32\,\mu m$ using 0.2-μm TetraSpeck beads from Invitrogen.

Once all the particles have been detected and their co-localization state addressed (that is, $d_{AB} < r_{ref}$), we measured the percentage of co-localization as the fraction of the total signal contained in particles that do co-localize, namely:

$$\text{Per cent of colocalization} = \frac{\sum \text{intensity of colocalizing particles}}{\sum \text{intensity of total particles}} \times 100$$

This measurement was then averaged between cells and compared between genotypes. Similar values of the percentage of co-localization were obtained if the fraction of co-localizing particles rather than the fraction of total intensity was considered (data not shown).

Since much of the signal of YFP–Rab11 at endogenous levels is lost upon fixation in our conditions, we measured the co-localization between Klp98–mCherry and YFP–Rab11 in living samples. We thus acquired only single planes and applied the algorithm describe above in 2D, considering $r_{ref} = resol_{xy}$.

Mean square displacement analysis of endosome tracks. All endosome tracks were recorded with a time interval of 12 s between frames. For each endosome track, a mean square displacement (MSD) analysis was performed using the MATLAB plugin MSD Analyser[61]. In brief, for each endosome track in data sets of different conditions, the MSD of segments of increasing duration (delay time *t*) was computed ($\text{MSD}(t) = \langle(\Delta_x)^2\rangle + \langle(\Delta_y)^2\rangle$ to obtain Extended Data Fig. 4a for wild type (103 tracks) and Extended Data Fig. 4b for Klp98A$^-$ (158 tracks). The 'weighted mean' of all individual MSD traces in each condition was then computed as described[61]: $\text{Weighted mean MSD}(t) = \frac{\sum_{i=0}^{n} w_i \text{MSD}_i(t)}{\sum_{i=0}^{n} w_i}$; where *n* is the number of tracks, $\text{MSD}_i(t)$ corresponds to the MSD value of the endosome track *i* for the delay time *t*, and w_i to the number of points averaged to compute $\text{MSD}_i(t)$ (Extended Data Fig. 4c and Extended Data Fig. 4a, b, black curve). Note that the weighted mean gives more weight to MSD curves that have greater certainty.

We fitted two fit functions to the measured weighted MSD of endosomes as a function of delay time: (i) motion with an average velocity *v* and a diffusive component with a diffusion *D* (diffusion + directed motion), which is captured by $\text{MSD}(t) = 4Dt + v^2t^2$; and (ii) simple diffusion, captured by $\text{MSD}(t) = 4Dt$.

While simple diffusion (that is, $\text{MSD}(t) = 4Dt$) captures well the motion of Klp98A$^-$ endosomes ($R^2 = 0.999$; $D = (2.04 \pm 0.02) \times 10^{-3}\,\mu m^2\,s^{-1}$; Extended Data Fig. 4c, 95% confidence interval), it poorly fits the data when considering the motion of wild-type endosomes ($R^2 = 0.8$). This indicates that Klp98A is essential for the directed motility of endosomes beyond diffusion, as seen in wild type. Indeed, the 'diffusion + directed motion' fit function (that is, $\text{MSD}(t) = 4Dt + v^2t^2$) fits well the wild-type data ($R^2 = 0.99$; Extended Data Fig. 4c). This fit provides an estimate for $v = (5.75 \pm 0.12) \times 10^{-3}\,\mu m\,s^{-1}$, while confirming the diffusion coefficient ($D = (1.83 \pm 0.13) \times 10^{-3}\,\mu m^2\,s^{-1}$; 95% confidence interval) observed in Klp98A$^-$ conditions. Furthermore, the 'diffusion + directed motion' fit function fits the Klp98A$^-$ data well ($R^2 = 0.999$) only for very low values of *v* ($v = (0.3 \pm 0.5) \times 10^{-3}\,\mu m\,s^{-1}$; $D = (2.11 \pm 0.04) \times 10^{-3}\,\mu m^2\,s^{-1}$; 95% confidence interval), confirming that most of the directed motion of wild-type endosomes is mediated by Klp98A motor function.

Since endosomes in Klp98A$^-$ mutants display simple diffusion, we used this mutant condition to independently evaluate the diffusion coefficient of endosomes by measuring the variance of the histograms of instantaneous speed $\frac{\Delta_x}{\Delta_t}$ and $\frac{\Delta_y}{\Delta_t}$ in both *x* and *y* dimensions. Indeed simple diffusion along the *x* axis is described by $D_x = \frac{\sigma_x \Delta_t}{2}$ (ref. 61), where σ_x is the variance of the instantaneous speed over the *x* axis and Δ_t is the frame-rate (here $\Delta_t = 12$ s). A corresponding expression applies to the *y* axis. This provided an estimate of $D_x = 0.0024\,\mu m^2\,s^{-1}$ (Extended Data Fig. 4d) and $D_y = 0.0023\,\mu m^2\,s^{-1}$ (Extended Data Fig. 4e), confirming the results of the MSD analysis above.

Spatio-temporal registration of movies. In this work, we used spatio-temporal registration of movies to generate a spatio-temporal endosome density plot during SOP division (Fig. 2d, Extended Data Fig. 7a). We also used this spatio-temporal registration to obtain a density plot of different microtubule markers to study the asymmetry of the spindle (Fig. 3a, b, Extended Data Figs 5, 6 and Supplementary Video 6). In addition, time registration allowed us to average data coming from several video data sets (Figs 1f, 3e and Extended Data Figs 2i, 4x and 7f), but also to compare the timing in different figure panels (for instance Figs 1f, 3e and Extended Data Fig. 2i)

Spatial registration was performed by defining the centre of the central spindle as monitored by the Pavarotti fluorescent signal, which is also used to establish a Cartesian system of coordinates with respect to which all the other signals (including endosome tracks and density of microtubule markers) are referred. Time registration capitalizes in the stereotypic dynamics of Pavarotti contraction which allowed us to align the timing of our data set of videos (Extended Data Fig. 4q–s). In figure panels where data sets have been registered in time, we have set registered time = 0 to the onset of anaphase B (that is, when the Pavarotti signal starts to constrict, see Extended Data Fig. 4r).

Spatial registration (reference frame tracking). A custom code in ImageJ (available upon request) was generated to segment the Pavarotti signal over time. This allowed us to track the Cartesian reference frame of the central spindle, defined by an origin and two axes (*x* and *y*, where the *y* axis is aligned with the division plane; Fig. 2a, b, Supplementary Video 3). The orientation of the *x* axis is defined to be anterior to posterior (pIIb to pIIa) and was determined by automatic tracking of the mRFP–Pon signal at the anterior cortex of the SOP.

In brief, the 3D stack of confocal slices in the Pavarotti channel (GFP– or mCherry–Pavarotti; 3 μm deep, $\Delta z = 0.5\,\mu m$) is projected (maximum-intensity projection), then the Pavarotti-positive region is fitted by an ellipse after semi-automated thresholding. The long axis of the ellipse defines the *y* axis of the reference frame described above and the short axis, the *x* axis (see Fig. 2a). The length of the Pavarotti-positive region along each axis is determined by taking the full-width half-maximum (FWHM) of the Pavarotti signal along the two axes. For each time point, five parameters are measured: Pavarotti width (PW, size of the Pavarotti-positive region along the *y* axis); Pavarotti length (PL, size along the *x* axis); x_c and y_c, the 2D coordinates (with respect to the top/left corner of the image) of the position of the origin C of the central spindle reference frame and α, the angle defined by the *x* axis of this reference frame and the image horizontal axis (Extended Data Fig. 4f). The anterior to posterior orientation of the *x* axis was determined by detecting the position of the fluorescence centroid of mRFP–Pon signal after manual thresholding.

To evaluate the accuracy of our central spindle tracking method, we applied this tracking code on movies of PFA-fixed fly nota acquired in identical imaging conditions. We calculated the deviation from the mean value of the different parameters (x_c, y_c and α) obtained from these movies of fixed material. We considered the FWHM of the histogram of these deviations as estimates for the accuracy of the parameters (Extended Data Fig. 4g, h, i). This analysis gave an estimated accuracy for x_c, y_c and α of 49 nm, 52 nm and 2.4°, respectively.

Temporal registration (PW alignment). Since the temporal profile of the shrinking Pavarotti width (PW) is stereotypic from cell to cell, we used it to register videos in time. For each cell, we plotted the temporal dynamics $\text{PW}_{cell}(t)$ together with that of a reference cell ($\text{PW}_{ref}(t)$; Extended Data Fig. 4o). This reference cell video was arbitrarily chosen as one that spanned from anaphase to cytokinesis, the relevant phases for this work.

We then determined the time delay τ_{cell} that needs to be applied to the cell of interest to minimize the difference, in absolute value, between the two Pavarotti temporal profiles (ΔPav), that is, find the τ_{cell} for which $\Delta\text{Pav}(\tau_{cell}) = \sum_{t=0}^{t=t_n} |\text{PW}_{cell}(t + \tau_{cell}) - \text{PW}_{ref}(t)|$ is minimum (Extended Data Fig. 4o, p). We then set the initial time of each movie to be equal to τ_{cell} thereby registering all the movies into an 'absolute time frame'. As expected, the registered PW curves collapsed ($R^2 = 0.93$) if plotted all together (Extended Data Fig. 4q–s). Importantly, the registered PL curves (Pavarotti size along the *x* axis), which were not used in the registration process and is a parameter independent of PW contraction, also collapsed ($R^2 = 0.8$; Extended Data Fig. 4t–v), validating our time registration method.

In a fewcases where the Pavarotti signal was not recorded in the video (Fig. 3e, for instance), we used instead the contraction of the Jupiter signal over the *y* axis as a reference. Since Jupiter is excluded from the region where Pavarotti is (Fig. 3a), the absence of Jupiter ('Jupiter gap', defined as a FWHM) can be used as a proxy of the Pavarotti region. Extended Data Fig. 4w shows that the contraction of the Jupiter gap follows that of Pavarotti, thus either marker can be used to register data sets in time.

Importantly, the contraction of Pavarotti/Jupiter is unaffected in Patronin depletion, Klp10A depletion and Klp98A mutants (Extended Data Fig. 4x), thus enabling temporal registration of videos acquired in these genetic backgrounds relative to control (Fig. 3e, h and Extended Data Fig. 7f).

Image averaging. To generate average videos (Fig. 3a and Extended Data Fig. 5a, b and Supplementary Video 6) the Pavarotti tracking data was used to rotate and translate each image to display them in a common spatial reference frame, the centre of which is the centre of the central spindle and whose *x* axis is horizontal. In order to minimize rotation artefacts, rotation was performed with bicubic interpolation after image scaling by a factor of 4 (without interpolation). After time registration, frames corresponding to each time point were processed by performing homogenous background subtraction and signal normalization

(to the brightest pixel). Finally, spatio-temporally registered videos corresponding to different cells were averaged to generate the 'average video'. All these operations were performed on *z*-projected images generated by signal integration over the entire volume of the spindle (sum projection, 12 μm total, $\Delta z = 0.5\,\mu m$). Images presented in Fig. 3a correspond to late cytokinesis (~600 s registered time, see Extended Data Fig. 4r).

Images of fixed samples (Extended Data Figs 5d–i, 6d–f) were obtained shortly before abscission, when PW and PL (Pavarotti size along *y* and *x* axes) do not change much (registered time > 600 s, Extended Data Fig. 4r) and therefore our time registration method (which relies on PW dynamics) cannot be applied anymore. At this stage, we thus used tubulin or Ac-tubulin stainings that had the characteristic '8' shape pattern of late mitotic spindles. For spatial registration, we capitalized on the fact that late spindles have a well-defined elongated 8 shape, allowing image alignment by cross-correlation with a reference image, as used in structure determination from single-particle electron microscopy data[62]. All these operations were performed on *z*-projected images (sum projection, 6 μm total, $\Delta z = 0.27\,\mu m$).

Quantification of endosome recruitment to the central spindle. To generate kymographs of endosome recruitment to the central spindle (Fig. 1g), we used the Pavarotti tracking data to rotate and translate each frame (as above for video averaging, but using maximum-intensity *z* projection in this case). Then each frame was *y*-projected onto its horizontal *x* axis and the *y*-projected movie was displayed as a kymograph.

To measure endosome recruitment to the central spindle (Fig. 1f, Extended Data Figs 2i and 7f), we used the Pavarotti tracking data to measure the iDelta$_{20}$ signal in the central spindle region over time. To quantify the iDelta$_{20}$ signal, images were *z*-projected (sum projection) after homogeneous background subtraction using a region of the cell devoid of endosomes. This *z* projection was then segmented using a constant manual threshold to identify the endosomes and the iDelta$_{20}$ intensity signal was integrated within the segmented endosomal regions. The iDelta$_{20}$ intensity signal was measured both in the central spindle region and the entire cell including the central spindle. The central spindle region was operationally defined on the *x* axis as a 2 μm region centred at the centroid of the Pavarotti region. The central-spindle-associated signal was then expressed as a percentage of the total signal present in the cell. The Pavarotti tracking data was also used for precise time registration of these movies.

Endosome tracking and reference frame change. Endosome tracking was performed using a custom Matlab code. In brief, the 3D stack containing the iDelta$_{20}$-Atto647N signal (3 μm deep, $\Delta z = 0.5\,\mu m$) was *z* projected (maximum-intensity projection). Particles were detected using a 2D Gaussian fitting algorithm, then tracked using a modified Vogel algorithm, as previously described[60]. Tracks were rendered using the ImageJ plugin mTrackJ[63].

To evaluate the accuracy of our endosome tracking method, we applied this tracking code on movies of PFA-fixed fly nota acquired in identical imaging conditions. As an estimate of average accuracy of their position with respect to the image frame (*x*, *y*), we calculated the FWHM of their distribution in this fixed material (Extended Data Fig. 4j–l). This analysis showed a positional accuracy of 57 nm along the *x* axis and 53 nm along the *y* axis. As expected, we found that this measured positional accuracy decreases with the signal-to-noise (SNR) ratio of the particle considered (Extended Data Fig. 4m) and we thus excluded from the analysis all the particles displaying a SNR < 15. The SNR of a diffraction limited object is defined as $\frac{I}{\sqrt{I+\sigma^2}}$, where I is the intensity collected at the brightest pixel of the spot and σ is the standard deviation of the local background[64]. Importantly, due to the very high photostability of our Atto-647N anti-Delta probe, the SNR ratio of endosomes, and thus their positional accuracy, does not vary significantly over time (Extended Data Fig. 4n).

Once we have determined the position of the tracked endosomes with respect to the reference frame of the image, we then expressed these coordinates into the Pavarotti Cartesian frame defined above. We did this in order to refer the motility of the endosomes with respect to the relevant structure: the Pavarotti-positive central spindle. If the endosome has the coordinates $\begin{bmatrix} x \\ y \end{bmatrix}$ in the image reference frame, then $\begin{bmatrix} x' \\ y' \end{bmatrix}$ corresponds to its coordinates in the central spindle reference frame. The central spindle reference frame is centred at $\begin{bmatrix} x_c \\ y_c \end{bmatrix}$ and oriented at an angle α (see above) with respect to the image reference frame (Extended Data Fig. 4f).

The coordinates in both reference frames are related by

$$\begin{bmatrix} x' \\ y' \end{bmatrix} = \begin{bmatrix} \cos(\alpha) & \sin(\alpha) \\ -\sin(\alpha) & \cos(\alpha) \end{bmatrix} \cdot \begin{bmatrix} x - x_c \\ y - y_c \end{bmatrix} \quad (1)$$

The precision of x' and y' thus depends on the relative precision of x, x_c, y, y_c and α. The variation of x' relative to x, x_c, y, y_c and α is as follows

$$dx' = \frac{\partial x'}{\partial x}dx + \frac{\partial x'}{\partial y}dy + \frac{\partial x'}{\partial \alpha}d\alpha + \frac{\partial x'}{\partial y_c}dy_c + \frac{\partial x'}{\partial x_c}dx_c \quad (2)$$

In equation (1) we have $x' = \cos(\alpha)(x - x_c) + \sin(\alpha)(y - y_c)$ so equation (2) becomes:

$$\begin{aligned} dx' = {} & \cos(\alpha)(dx - dx_c) + \sin(\alpha)(dy - dy_c) \\ & + [\cos(\alpha)(y - y_c) - sin(\alpha)(x - x_c)]d\alpha \end{aligned} \quad (3)$$

Since errors are independent, an upper estimate of the accuracy of x' (worst case scenario) is thus:

$$\begin{aligned} dx' = {} & |\cos(\alpha)|(dx + dx_c) + |\sin(\alpha)|(dy + dy_c) \\ & + |\cos(\alpha)(y - y_c) - \sin(\alpha)(x - x_c)|d\alpha \end{aligned} \quad (4)$$

We considered an experimental data set of x, x_c, y, y_c and α from a collection of 263 data points corresponding to endosome tracks close to the Pavarotti centroid, as well as the estimated accuracy by tracking endosomes and central spindles in fixed material described above ($dx = 57$ nm, $dy = 53$ nm, $d\alpha = 2.4°$ (0.042 rad), $dx_c = 49$ nm and $dy_c = 52$ nm; Extended Data Fig. 4g–l). Using this data to input into equation (4), we obtained an upper bound for the average accuracy of $dx' = 166$ nm in the *x* axis, the axis relevant to the motility of endosomes on the central spindle microtubules. Note that the bidirectional movements that we observed at the central spindle (Fig. 2e and Extended Data Fig. 4y) are in the micrometre range, which is therefore one order of magnitude larger than the accuracy of our measurements.

Endosome track analysis. To generate spatio-temporal endosome density plots from our data set of endosome tracks (Fig. 2d and Extended Data Fig. 7a), we binned the data (time bins = 10 s and space bins = 0.5 μm), counted the number of tracks present in each bin and displayed this information as kymograph-type of image and applied the Red Hot lookup table.

For residence time measurements (Extended Data Fig. 7d, e), subsets of 101 tracks for control and 30 for Patronin RNAi ('high-quality tracks', see also below) were selected after gap correction by manual inspection, if necessary (see Extended Data Fig. 4y for examples). Tracks were selected (i) to be long enough (200 time points on average, thereby allowing to determine residence time); (ii) to display low motility on the *y* axis (indicating endosomal motility on the central spindle microtubules; Fig. 2.f); and (iii) to contain at least one bidirectional motility event on the central spindle (that is, side-change event). We defined a side-change event as an event where an endosome is moving from the pIIa to the pIIb side of the spindle (or vice versa), that is, when the *x* coordinate of the moving endosome changes sign. On average, in our selected data, we observed 9 ± 1 side changes per track, which allow determination of the average residence time on each side of the central spindle.

Residence time of endosomes on each side of the spindle was measured as follows. After detection of side-change events, the time spent by endosomes in each side of the spindle between these events was computed. Owing to the 166 nm precision of our tracks within the central spindle frame (see above), we excluded from this analysis the segments of the tracks between $x = -83$ nm and $x = +83$ nm, but the result did not qualitatively change if this region is considered in the analysis (data not shown).

To measure the velocity of microtubule-based-motility, we manually selected segments within our track data where the orientation of movement in the *x* axis was occurring prominently in one direction for at least ten time points. These segments are referred to as 'strides'. For each selected stride, we plotted *x* position versus time and performed a linear fit to estimate the velocity of the stride. This gave us an estimate of $v = 0.173 \pm 0.007\,\mu m\,s^{-1}$.

Measurement of k_{off}, $k_{on}\rho$ and transport run length of endosomes for microtubules. To measure the off-rate (k_{off}) of endosomes from microtubules at the central spindle, we first automatically detected, on our central spindle tracks, which segments within the tracks correspond to events of transport on microtubules ('transport segment'). We performed this track analysis on the subset of 101 control high-quality tracks (see above and Extended Data Fig. 10b for an example). The analysis is based on the study of the properties of each step (the displacement between two frames) and the correlation between successive steps.

We operationally defined a transport segment using three criteria.

(i) Instantaneous speed in each of the steps in the transport segment must be higher than $0.15\,\mu m\,s^{-1}$. Since the velocity of microtubule-based-motility *in vivo* is $v = 0.173\,\mu m\,s^{-1}$, the diffusion coefficient is low and the frame rate is high (see below), this threshold decreases considerably the probability of incorrectly identifying a step of diffusion as a transport step. Two additional criteria help decreasing further this probability.

(ii) Segments must last for at least two consecutive steps (three frames).

(iii) The orientation of the movement must be the same for all the steps in a transport segment. These two additional criteria make negligible the probability of incorrectly identifying a diffusion segment (a segment composed only of

diffusive steps) as a transport segment. Indeed, the probability that a rare fast step of diffusion is followed by yet another rare fast step in the same orientation is extremely low.

We actually estimated by performing stochastic simulations (not shown) that, with our measured value $D = 0.0021 \pm 0.0001\,\mu m^2\,s^{-1}$ and for the fastest frame rate used (1.4 Hz), the probability of incorrectly identifying a diffusion-segment as a transport-segment is about 1×10^{-3}. We found $k_{off} = 0.90 \pm 0.06\,s^{-1}$ from exponential fits of the distribution of the duration of transport segments (95% confidence interval; see Extended Data Fig. 10c).

To estimate $k_{on}\rho$, we considered the track segments in between transport segments which we defined operationally as diffusion segments. We then found $k_{on}\rho = 0.05 \pm 0.01\,s^{-1}$ (95% confidence interval; Extended Data Fig. 10d). Note that, since we analyse the tracks regardless of their position within the central spindle, the value of the measured $k_{on}\rho$ is an average of values for different microtubule densities (that is, $k_{on}\rho = k_{on}(\rho_a + \rho_b)/2$).

Extended Data Fig. 10e shows the distribution of run lengths in the transport-state. To estimate the characteristic run length λ for the transport state, we used the method described by Thorn and Vale (ref. 65). In brief, we determined the cumulative distribution $P(x)$ of the transport run lengths x (that is, the fraction of run lengths shorter than a given run length). We then fitted the observed cumulative distribution $P(x)$ to the corresponding equation $P(x) = 1 - e^{\frac{x-x_0}{\lambda}}$ for $x > x_0$, where $x_0 = 0.4\,\mu m$ is the lower limit of runs included in the fit ($x \leq x_0$ corresponds to short runs, which are not measured with great accuracy and are thereby excluded from the analysis). The characteristic transport run length is $\lambda = 0.31 \pm 0.01\,\mu m$ ($R^2 = 0.98$; 95% confidence interval).

The advantage of the Thorn and Vale procedure is that it allows us to fit the data directly without data binning. Indeed, it has been shown that performing the exponential fit directly on the binned run length distribution (like in Extended Data Fig. 10e) yields characteristic run lengths that depend strongly on the size of the bins.

Measurement of iDelta$_{20}$ asymmetry. iDelta$_{20}$ asymmetry was measured at late stages of cytokinesis when all endosomes had departed from the central spindle, and iDelta$_{20}$ asymmetry had reached its maximum (~600 s in registered time, see Fig. 1f and Extended Data Fig. 2i). Asymmetry was measured as follows. Endosomes were first detected by using the 2D Gaussian fitting algorithm described above. For all data sets, the same minimal fluorescence signal above local background was imposed to detect bona fide endosomes. Total intensity was then integrated for each endosomes, with the local background determined by Gaussian fitting subtracted. The pIIa and the pIIb cells were then segmented manually using the Pon channel as a reference. Finally, endosomes were assigned based on their coordinates to the segmented pIIa or the pIIb regions. The total endosomal signal for each daughter cell was subsequently computed. The percentage of iDelta$_{20}$ in the pIIa daughter cell was then calculated as:

$$\text{Percentage of iDelta}_{20}\text{ in pIIa} = \frac{\text{iDelta}_{20}\ \text{intensity}\ \text{pIIa}}{\text{iDelta}_{20}\ \text{intensity}\ \text{pIIa} + \text{iDelta}_{20}\ \text{intensity}\ \text{pIIb}} \times 100$$

We measured the percentage of iDelta$_{20}$ signal in the pIIa daughter cell rather than the ratio of signal between the two cells (pIIa:pIIb) since our automatic detection method sometimes did not detect any particles in one of the two daughter cell, leading to a pIIa:pIIb ratio of 0 or infinity.

Importantly, the iDelta$_{20}$ asymmetries measured by this method were almost identical to results obtained with our previous method based on a 3D signal integration after manual background subtraction and thresholding[1,2,50] (data not shown). In addition, the iDelta$_{20}$ asymmetry measured by this method was similar if endosome numbers or area were considered instead of endosome intensity (data not shown).

For correlative measurements of spindle asymmetry versus iDelta$_{20}$ endosome asymmetry, and exploration of conditions where spindle asymmetry is inverted (Fig. 4 and Extended Data Fig. 10), we rather plotted the ratio of iDelta$_{20}$ in pIIa, which is calculated as:

$$\text{Ratio of iDelta}_{20}\text{ in pIIa} = \frac{\text{iDelta}_{20}\ \text{intensity pIIa}}{\text{iDelta}_{20}\ \text{intensity pIIa} + \text{iDelta}_{20}\ \text{intensity pIIb}}$$

Measurement of spindle asymmetry in anaphase. In this work, we measured spindle asymmetry by two methods: the 'pseudo-line-scan' method and the 'segmentation' method (illustrated in Extended Data Fig. 5c). Both methods gave similar results in live material (Extended Data Fig. 5c corresponding to the samples displayed in Fig. 3a) and in fixed samples (Extended Data Fig. 5h, i). Unless stated otherwise, the pseudo-line-scan method was used.

Pseudo-line-scan method. For measurements of spindle asymmetry on live material (Fig. 3b, e), we first projected z stacks containing the entire central spindle (6 μm depth, $\Delta z = 0.5\,\mu m$) using sum-intensity projection. We then segmented the Pavarotti signal as described above (see spatio-temporal registration), which defined x/y axes of the spindle, as well as PW (Fig. 2a). Jupiter–GFP, GFP–Patronin or SiR-tubulin signal intensity was then measured along the x axis upon signal integration over the y axis within a region of interest (ROI) centred on the Pavarotti region centroid. This measurement thus conceptually resembles a line scan along the x axis of the spindle, but a rectangular ROI, rather than a line, is considered (ROI dimensions: 10 μm on the x axis and PW on the y axis). The signal intensity over the x axis determined this way displays two peaks: one in pIIa, one in pIIb, see Fig. 3b and Extended Data Fig. 5c. This reflects the facts that these signals are excluded (at least in part) from the Pavarotti region in the middle of the central spindle (see Fig. 2a). We then measured the value of each peak and subtracted the local background (average background was determined from five pixels adjacent to the spindle). Central spindle asymmetry was computed as the enrichment of the density of the marker in the pIIb relative to the pIIa according to

$$\text{Signal enrichment in pIIb} = \frac{\text{peak intensity pIIb} - \text{peak intensity pIIa}}{\text{peak intensity pIIa}} \times 100$$

Importantly, results were almost identical if a maximum intensity projection was used instead of a sum-intensity projection, and if microtubule density was measured along a line scan with a 1 pixel width instead of the entire width of the spindle by using the ROI, suggesting that spindle asymmetry is invariant along the y axis (data not shown).

For measurement of spindle asymmetry on live material (Fig. 3e), we measured this marker enrichment in pIIb at each time point and subsequently averaged these values between different videos using the time registration method described above. In cases where frame rates were not identical among videos, the spindle asymmetry values were interpolated to the correct frame rate using spline interpolation.

The kymograph of Jupiter–GFP depolymerization (Fig. 3f) was generated by plotting the pseudo-line-scan for each time point as a kymograph. We then applied the Red Hot lookup table.

For correlative measurements of spindle asymmetry versus iDelta$_{20}$ endosome asymmetry, and exploration of conditions where spindle asymmetry is inverted (Fig. 4 and Extended Data Fig. 10), we plotted Δ, the normalized enrichment of microtubule density in the pIIb side, rather than the enrichment on the pIIb. Δ is given by the formula:

$$\Delta = \frac{\text{peak intensity pIIb} - \text{peak intensity pIIa}}{\text{peak intensity pIIb} + \text{peak intensity pIIa}}$$

Note that Δ is symmetrical when pIIb and pIIa are inverted and that $-1 \leq \Delta \leq 1$.

For images of fixed samples (Extended Data Figs 5d–i, 6d–f and 8f, g), we capitalized on the fact that the spindle asymmetry as a function of time remains approximately constant at late stages of cytokinesis (Fig. 3e) and therefore measurements at those stages are unlikely to be affected by incorrect time registration. We fitted the microtubule marker signal to an ellipse to obtain the x and y axes of the spindle, determined manually (in the absence of Pavarotti signal) the cytokinesis plane and measured the microtubule enrichment in pIIb as described above considering a ROI of dimensions 10 μm on the x axis and 0.812 μm (4 pixels) over the y axis.

Segmentation method. In this method, we segmented the central spindle by considering an intensity threshold above the cytosolic background and computed the average intensity in the segmented regions in the pIIa and pIIb sides (see Extended Data Fig. 5c). This second methods considers the average density of the complete pool of microtubules at the central spindle. This gave comparable results to the pseudo-line-scan method (Extended Data Fig. 5c, h, i).

Measurement of spindle asymmetry during metaphase. To measure spindle asymmetry in metaphase (Extended Data Fig. 5n), we first projected z stacks containing the entire metaphase spindle (8.5 μm depth, $\Delta z = 0.5\,\mu m$) using maximum-intensity projection. We then drew a line between the two spindle poles, which define the mitotic plane: the plane orthogonal to this line, located in the middle distance between centrosomes. We then measured the total signal in two ROIs of 4.6 μm (along the mitotic plane) × 2.3 μm (along the inter-centrosome line) on each side of the mitotic plane, in the pIIa and pIIb sides. Local background was subtracted by considering an adjacent ROI in the cell outside the spindle and the two ROIs described above. The signal enrichment on the pIIb side was then computed as

$$\text{Signal enrichment in pIIb} = \frac{\text{total intensity pIIb ROI} - \text{total intensity pIIa ROI}}{\text{total intensity pIIa ROI}} \times 100$$

Importantly, these ROIs do not contain the centrosomes so that spindle asymmetry measurements are not affected by centrosome asymmetry (Extended Data Fig. 5o, p).

Measurement of centrosome asymmetry. To measure centrosome asymmetry of different markers throughout mitosis (Extended Data Fig. 9d–h), we first projected z stacks containing the entire centrosome signal (6 μm depth, $\Delta z = 0.5$ μm) using maximum-intensity projection. We then measured the intensity of each centrosome by considering a circular ROI centred on the centrosome (1.4 μm diameter). Local background was subtracted by considering an adjacent ROI of identical diameter. We then calculated the ratio between the pIIa and the pIIb centrosome intensities. For prophase and prometaphase, the pIIa/pIIb centrosome identity could not be assigned since spindle rotates during metaphase. We therefore measured the ratio of the brighter centrosome over the dimer.

Measurement of normalized Jupiter–GFP Density. To compare Jupiter–GFP intensity between different videos (Fig. 3g,h), a reference intensity was needed to account for the variations of the Jupiter–GFP signal, which occurs even in identical imaging conditions and with expression of Jupiter–GFP at endogenous levels, probably owing to different imaging depths into the tissue. We decided to use the intensity of the centrosome of the pIIa daughter cell, which Jupiter labels throughout the cell cycle (Fig. 3d and Supplementary Video 7) as a reference. We measured the intensity of the pIIa centrosome by considering a circular ROI centred on the centrosome (1.2 μm diameter) and integrating the signal intensity within the ROI on ten z planes (5 μm total depth). Local background was subtracted by considering an adjacent ROI of identical diameter for each plane. We then measured the Jupiter–GFP signal in both the pIIa and the pIIb daughter cells by using the same circular ROI dimensions and background subtraction as above. We then normalized the obtained signal intensity by the pIIa centrosome value.

Interestingly, the centrosome of the pIIa daugther cell is 1.41 ± 0.06 (mean ± s.e.m.; $n = 26$ cells) times more intense than the one of the pIIb daughter at the late cytokinesis stage considered here (Fig. 3d, Extended Data Fig. 5o, p, Supplementary Video 7). Importantly, this difference is still present in Patronin RNAi (1.39 ± 0.17, $n = 24$) or Klp10A RNAi (1.25 ± 0.08, $n = 23$; Extended Data Fig. 5o, p) conditions, although the values of the normalized central spindle intensities are different from wild-type conditions (Fig. 3h), suggesting that using the pIIa centrosome is indeed a good way to normalize the Jupiter–GFP data. The fact that Patronin RNAi does not affect microtubule density around the centrosome is in agreement with a recent report showing that CAMSAP2, a mammalian orthologue of Patronin, does not act on astral microtubules[28].

Statistics. Unless stated otherwise, measurements are given in mean ± s.e.m. Fit values (MSD analysis, Extended Data Fig. 9e and 10c–e), are provided with their 95% confidence interval. The experiments were not randomized and the investigators were not blinded to allocation during experiments and outcome assessment. No statistical methods were used to predetermine sample size. All statistical analyses were performed using SigmaStat 3.5 software (Systat) with an α of 0.05. Normality of variables was verified with Kolmogorov–Smirnov tests. Homoscedasticity of variables was always verified when conducting parametric tests. For Fig. 3h, a $\log_{10}$ transformation was applied to the data. In the case were variables failed normality and/or homoscedasticity tests, non-parametric tests were applied. In the main figures, we used Dunn's post hoc test when performing Kruskal–Wallis tests (Fig. 1h, i) and Tukey's post hoc test when performing ANOVA (Figs 3h and 4b). Post hoc tests used in Extended Data figures are indicated in their respective figure legends.

29. Gong, W. J. & Golic, K. G. Ends-out, or replacement, gene targeting in *Drosophila*. *Proc. Natl Acad. Sci. USA* **100,** 2556–2561 (2003).
30. Gong, W. J. & Golic, K. G. Genomic deletions of the *Drosophila* melanogaster *Hsp70* genes. *Genetics* **168,** 1467–1476 (2004).
31. Seum, C. *et al. Drosophila* SETDB1 is required for chromosome 4 silencing. *PLoS Genet.* **3,** e76 (2007).
32. Emery, G. *et al.* Asymmetric Rab 11 endosomes regulate delta recycling and specify cell fate in the *Drosophila* nervous system. *Cell* **122,** 763–773 (2005).
33. Bellaïche, Y., Gho, M., Kaltschmidt, J. A., Brand, A. H. & Schweisguth, F. Frizzled regulates localization of cell-fate determinants and mitotic spindle rotation during asymmetric cell division. *Nature Cell Biol.* **3,** 50–57 (2001).
34. Minestrini, G., Mathe, E. & Glover, D. M. Domains of the Pavarotti kinesin-like protein that direct its subcellular distribution: effects of mislocalisation on the tubulin and actin cytoskeleton during *Drosophila* oogenesis. *J. Cell Sci.* **115,** 725–736 (2002).
35. Lu, B., Ackerman, L., Jan, L. Y. & Jan, Y. N. Modes of protein movement that lead to the asymmetric localization of partner of Numb during *Drosophila* neuroblast division. *Mol. Cell* **4,** 883–891 (1999).
36. Mummery-Widmer, J. L. *et al.* Genome-wide analysis of Notch signalling in *Drosophila* by transgenic RNAi. *Nature* **458,** 987–992 (2009).
37. Bitan, A., Rosenbaum, I. & Abdu, U. Stable and dynamic microtubules coordinately determine and maintain *Drosophila* bristle shape. *Development* **139,** 1987–1996 (2012).
38. Tang, H. *et al.* Numb proteins specify asymmetric cell fates via an endocytosis- and proteasome-independent pathway. *Mol. Cell. Biol.* **25,** 2899–2909 (2005).
39. Betschinger, J., Mechtler, K. & Knoblich, J. A. The Par complex directs asymmetric cell division by phosphorylating the cytoskeletal protein Lgl. *Nature* **422,** 326–330 (2003).
40. Fabrowski, P. *et al.* Tubular endocytosis drives remodelling of the apical surface during epithelial morphogenesis in *Drosophila*. *Nature Commun.* **4,** 2244 (2013).
41. Dunst, S. *et al.* Endogenously tagged rab proteins: a resource to study membrane trafficking in *Drosophila*. *Dev. Cell* **33,** 351–365 (2015).
42. Bökel, C., Schwabedissen, A., Entchev, E., Renaud, O. & Gonzalez-Gaitan, M. Sara endosomes and the maintenance of Dpp signaling levels across mitosis. *Science* **314,** 1135–1139 (2006).
43. Rothbauer, U. *et al.* A versatile nanotrap for biochemical and functional studies with fluorescent fusion proteins. *Mol. Cell. Proteomics* **7,** 282–289 (2008).
44. Iwaki, T., Figuera, M., Ploplis, V. A. & Castellino, F. J. Rapid selection of *Drosophila* S2 cells with the puromycin resistance gene. *Biotechniques* **35,** 482–484, 486 (2003).
45. Derivery, E. *et al.* The Arp2/3 activator WASH controls the fission of endosomes through a large multiprotein complex. *Dev. Cell* **17,** 712–723 (2009).
46. Krahn, M. P., Klopfenstein, D. R., Fischer, N. & Wodarz, A. Membrane targeting of Bazooka/PAR-3 is mediated by direct binding to phosphoinositide lipids. *Curr. Biol.* **20,** 636–642 (2010).
47. Goshima, G. & Vale, R. D. The roles of microtubule-based motor proteins in mitosis: comprehensive RNAi analysis in the *Drosophila* S2 cell line. *J. Cell Biol.* **162,** 1003–1016 (2003).
48. Forer, A. & Pickett-Heaps, J. D. Cytochalasin D and latrunculin affect chromosome behaviour during meiosis in crane-fly spermatocytes. *Chromosome Res.* **6,** 533–549 (1998).
49. Januschke, J. & Gonzalez, C. The interphase microtubule aster is a determinant of asymmetric division orientation in *Drosophila* neuroblasts. *J. Cell Biol.* **188,** 693–706 (2010).
50. Loubéry, S. & Gonzalez-Gaitan, M. Monitoring notch/delta endosomal trafficking and signaling in *Drosophila*. *Methods Enzymol.* **534,** 301–321 (2014).
51. Jauffred, B. & Bellaiche, Y. Analyzing frizzled signaling using fixed and live imaging of the asymmetric cell division of the *Drosophila* sensory organ precursor cell. *Methods Mol. Biol.* **839,** 19–25 (2012).
52. Bell, P. B. Jr & Safiejko-Mroczka, B. Improved methods for preserving macromolecular structures and visualizing them by fluorescence and scanning electron microscopy. *Scanning Microsc.* **9,** 843–857, discussion 858–860 (1995).
53. Gell, C. *et al.* Microtubule dynamics reconstituted *in vitro* and imaged by single-molecule fluorescence microscopy. *Methods Cell Biol.* **95,** 221–245 (2010).
54. Lai, E. C. & Rubin, G. M. neuralized functions cell-autonomously to regulate a subset of notch-dependent processes during adult *Drosophila* development. *Dev. Biol.* **231,** 217–233 (2001).
55. Yeh, E., Zhou, L., Rudzik, N. & Boulianne, G. L. Neuralized functions cell autonomously to regulate *Drosophila* sense organ development. *EMBO J.* **19,** 4827–4837 (2000).
56. Gruenberg, J. The endocytic pathway: a mosaic of domains. *Nature Rev. Mol. Cell Biol.* **2,** 721–730 (2001).
57. Sönnichsen, B., De Renzis, S., Nielsen, E., Rietdorf, J. & Zerial, M. Distinct membrane domains on endosomes in the recycling pathway visualized by multicolor imaging of Rab4, Rab5, and Rab11. *J. Cell Biol.* **149,** 901–914 (2000).
58. Zerial, M. & McBride, H. Rab proteins as membrane organizers. *Nature Rev. Mol. Cell Biol.* **2,** 107–117 (2001).
59. Bolte, S. & Cordelieres, F. P. A guided tour into subcellular colocalization analysis in light microscopy. *J. Microsc.* **224,** 213–232 (2006).
60. Holtzer, L. & Schmidt, T. *The tracking of individual molecules in cells and tissues* (Wiley-VCH, 2010).
61. Tarantino, N. *et al.* TNF and IL-1 exhibit distinct ubiquitin requirements for inducing NEMO-IKK supramolecular structures. *J. Cell Biol.* **204,** 231–245 (2014).
62. Frank, J. *Three-Dimensional Electron Microscopy of Macromolecular Assemblies: Visualization of Biological Molecules in Their Native State* 2nd edn (Oxford University Press, 2006).
63. Meijering, E., Dzyubachyk, O. & Smal, I. Methods for cell and particle tracking. *Methods Enzymol.* **504,** 183–200 (2012).
64. Kural, C. & Kirchhausen, T. Live-cell imaging of clathrin coats. *Methods Enzymol.* **505,** 59–80 (2012).
65. Thorn, K. S., Ubersax, J. A. & Vale, R. D. Engineering the processive run length of the kinesin motor. *J. Cell Biol.* **151,** 1093–1100 (2000).
66. Mayer, B., Emery, G., Berdnik, D., Wirtz-Peitz, F. & Knoblich, J. A. Quantitative analysis of protein dynamics during asymmetric cell division. *Curr. Biol.* **15,** 1847–1854 (2005).
67. Kirchhofer, A. *et al.* Modulation of protein properties in living cells using nanobodies. *Nature Struct. Mol. Biol.* **17,** 133–138 (2010).
68. Derivery, E., Helfer, E., Henriot, V. & Gautreau, A. Actin polymerization controls the organization of WASH domains at the surface of endosomes. *PLoS ONE* **7,** e39774 (2012).
69. Vonderheit, A. & Helenius, A. Rab7 associates with early endosomes to mediate sorting and transport of Semliki forest virus to late endosomes. *PLoS Biol.* **3,** e233 (2005).

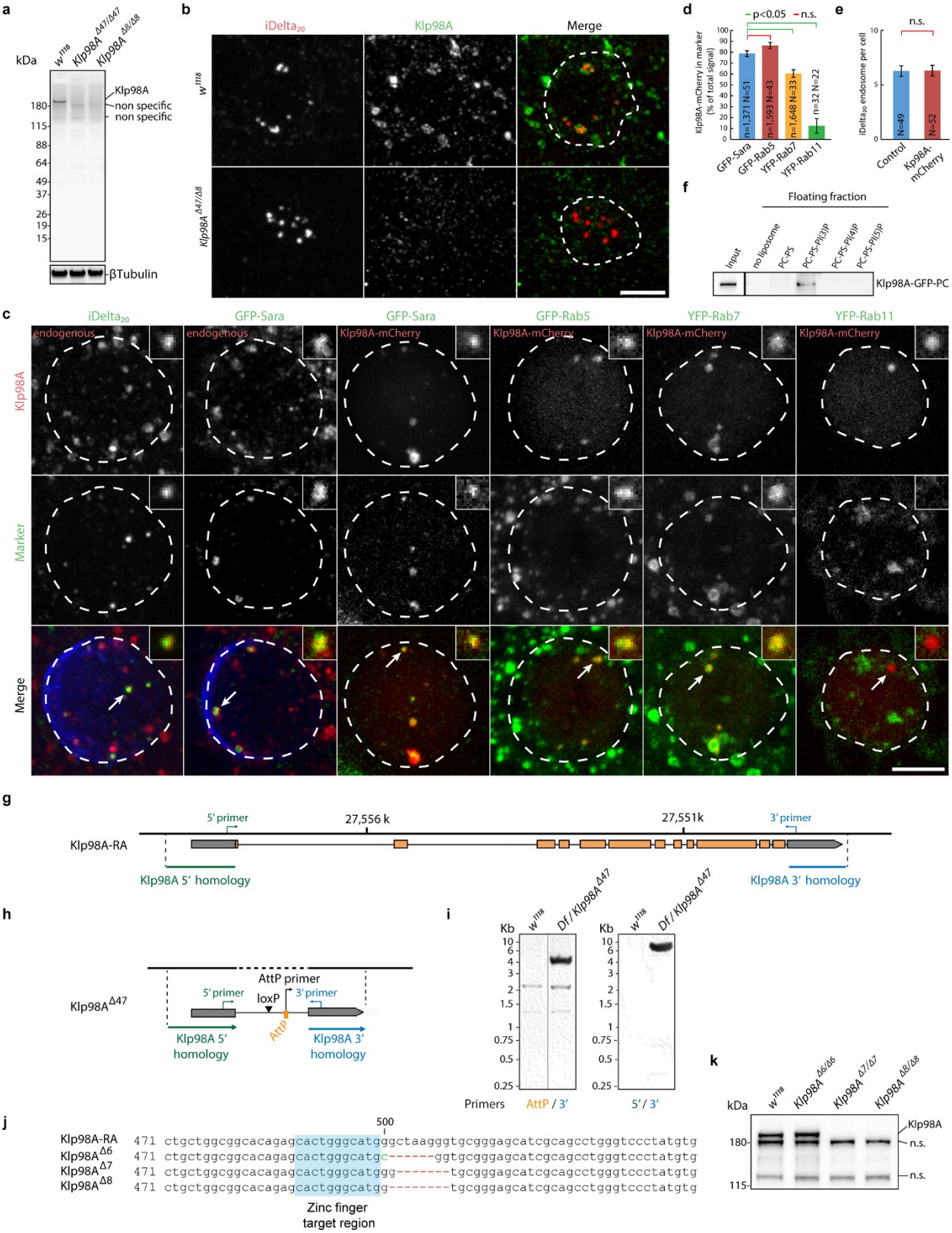

Extended Data Figure 1 | See next page for caption.

Extended Data Figure 1 | Characterization of Klp98A. a, **b**, Characterization of the polyclonal anti-Klp98A antibody in western blot and immunofluorescence. **a**, Western blot of total extracts of w^{1118} and Klp98A^{-} mutant L2 larvae using anti-Klp98A antibodies. Klp98A is the major band above 180 kDa that disappears in Klp98A^{-} mutants. Western blot is representative of two experiments. **b**, Confocal image showing SOPs in the notum labelled by iDelta$_{20}$ and Klp98A immunofluorescence in w^{1118} and Klp98A^{-} mutants. Imaging was performed by spinning-disk confocal microscopy (SDCM, *z* projection). Dashed line, SOP outline. The Klp98A staining associated with Sara endosomes disappears in Klp98A^{-} mutants. **c**–**e**, Klp98A-containing vesicles are early endosomes. **c**, SOPs in metaphase showing Klp98A (first row; either endogenous, in the two first columns, or, in the other columns, Klp98A–mCherry at low expression levels, using temperature control) together with endosomal markers (second row; iDelta$_{20}$, GFP–Sara at low expression levels, as well as GFP–Rab5 and YFP–Rab7 and YFP–Rab11 at endogenous expression levels). Third row, merge; red channel, Klp98A; green channel, endosomal marker; mRFP–Pon, in blue, is also shown in some panels. SDCM imaging. Except for YFP–Rab11, fixed samples were imaged (*z* projection of the entire cell; maximum intensity). Insets correspond to single planes of higher magnification images of a representative endosome (arrow). For YFP–Rab11, images correspond to one single *z* plane in a live cell. Dashed lines, cell outline. Note an apparent lack of fine-grain co-localization between Klp98A and iDelta$_{20}$, which reflects the existence of distinct sub-domains within a particular vesicular compartment, as previously reported for early endosomes[57,68,69]. Scale bars in **b** and **c** are 5 μm. **d**, Automated quantification of the 3D co-localization (see co-localization section in Methods) of Klp98A with the various endosomal markers shown in **c**. Quantification is performed in 2D for YFP–Rab11. Klp98A shows a high level of co-localization with GFP–Sara and GFP–Rab5. A lower, but significant, level of co-localization is observed with YFP–Rab7, and almost no co-localization with YFP–Rab11 (Kruskal–Wallis non-parametric ANOVA followed by Dunn's post-hoc test; *N*, number of cells; *n*, number of endosomes). **e**, Quantification of the number of iDelta$_{20}$ endosomes per SOP in control cells and cells expressing Klp98A–mCherry at low levels. Klp98A–mCherry expression does not affect the number of iDelta$_{20}$ endosomes per cell (Mann–Whitney rank sum test; *N*, number of cells). **f**, Western blot anti-Protein-C tag (PC) of the input and of floating fractions from liposome floating assays using small unilamellar vesicles (SUVs) of different compositions (DOPC:DOPS 90:10; DOPC:DOPS:PI(3)P 80:10:10; DOPC:DOPS:PI(4)P 80:10:10; DOPC:DOPS:PI(5)P 80:10:10) and purified Klp98A–GFP–PC (see Methods). Floating fractions corresponding to equal amounts of liposomes were loaded. Note that, to show the input together with the other samples in this image, the input lane is displayed after a lower exposure time and separated from the other lanes by a vertical line. Klp98A–GFP–PC directly binds to PI(3)P-containing liposomes, and does not bind to PI(4)P- nor PI(5)P-containing liposomes. Western blot is representative of two experiments. **g**–**i**, Generation of the $Klp98A^{\Delta 47}$ deletion mutant by homologous recombination (see Methods). **g**, *Klp98A* isoform A (Klp98A-RA) gene organization. Homology regions used to generate the mutant as well as PCR primers for its characterization are displayed. **h**, Gene organization after homologous recombination: the *Klp98A* gene has been replaced by an AttP site. **i**, PCR analysis of control (w^{1118}) and the $Klp98A^{\Delta 47}$ mutant showing the expected short amplicon in the $Klp98A^{\Delta 47}$ mutant (5′/3′ primers) and the presence of the Attp site in the $Klp98A^{\Delta 47}$ mutant locus (Attp/3′ primers). **j**, Sequence of the three *Klp98A* alleles obtained by zinc-finger-mediated mutagenesis (see Methods). Position refers to the coding sequence of Klp98A (CG5658-PA). $Klp98A^{\Delta 6}$ corresponds to a missense mutation followed by a six-base-pair deletion causing missense change and deletion of two amino acids in the protein. $Klp98A^{\Delta 7}$ and $Klp98A^{\Delta 8}$ correspond to seven- and eight-base-pair deletions causing frame shifts. All the Klp98A mutants generated in this study are viable and fertile in *trans* with $Klp98A^{\Delta 47}$. **k**, Western blot of total extracts of w^{1118} control and Klp98A^{-} mutant L2 larvae using anti-Klp98A antibodies. n.s., non-specific bands (see **a**) serving as loading controls. Full length Klp98A is absent in both $Klp98A^{\Delta 7}$ and $Klp98A^{\Delta 8}$ mutants, but is produced at normal levels in $Klp98A^{\Delta 6}$. Western blot is representative of two experiments. For source gel images of the various western blots displayed in this figure, see Supplementary Fig. 1.

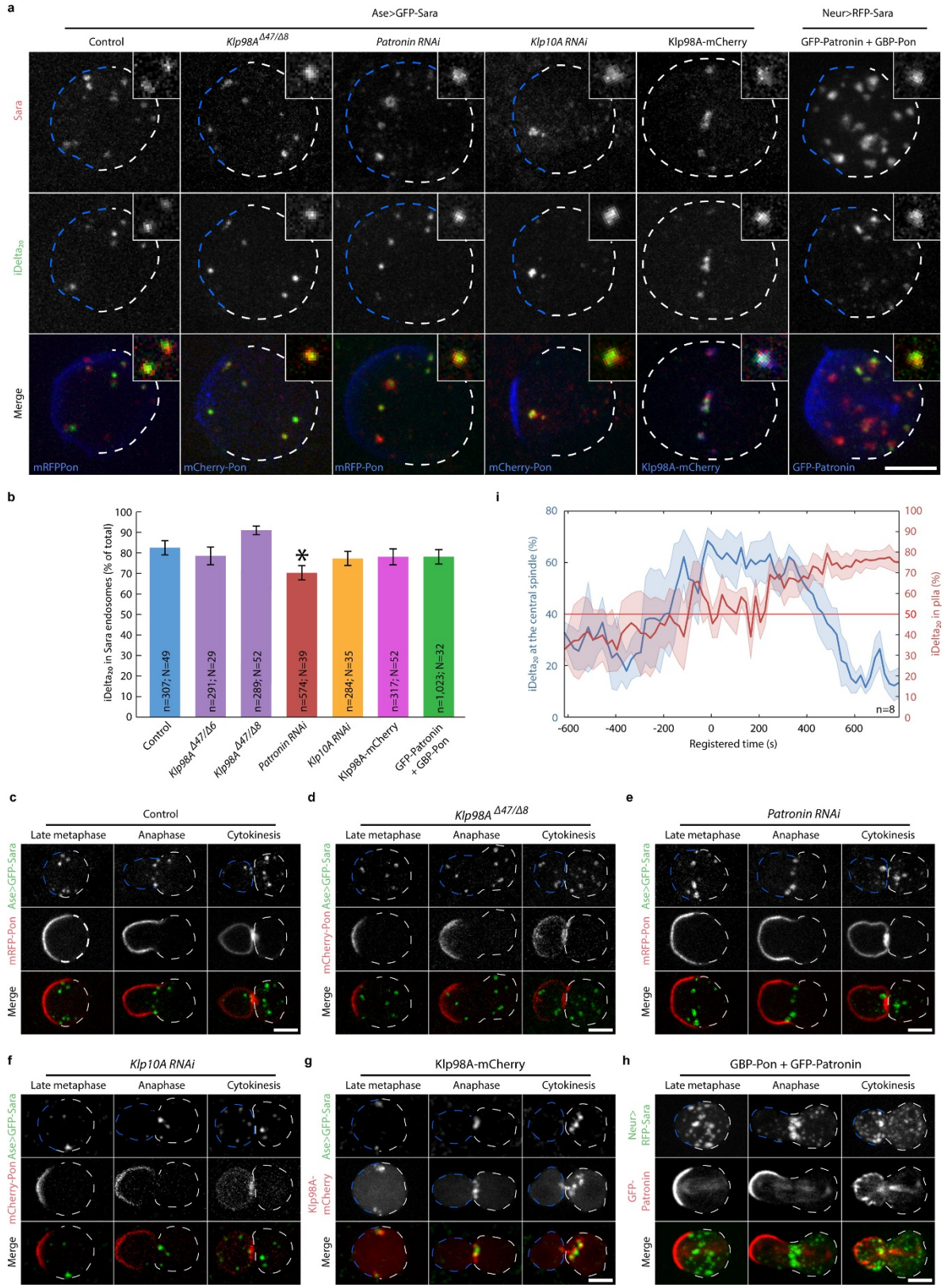

Extended Data Figure 2 | See next page for caption.

Extended Data Figure 2 | iDelta$_{20}$ co-localizes with Sara and they both show the same dynamics in all the genotypes considered in this study. **a**, **b**, iDelta$_{20}$ co-localizes with Sara in all the genotypes considered in this study. **a**, SOPs in metaphase showing GFP–Sara or RFP–Sara (first row) and iDelta$_{20}$ (second row) in the different backgrounds studied in this work (SDCM imaging; image corresponds to maximum-intensity *z* projection of entire cells; insets corresponds to single planes). Third row, merge: Sara in red; iDelta$_{20}$ in green; mRFP–Pon, mCherry–Pon, Klp98A–mCherry or GFP–Patronin in blue. Except for the right-most panel (GBP experiment), GFP–Sara was expressed at low levels using an ase > GFP–Sara construct, yielding Sara endosomes which appear mostly as diffraction-limited vesicles. Dashed line, cell outline (pIIb blue, pIIa white). For the right-most panel, RFP–Sara expression is at some higher level under the control of Neur-Gal4. **b**, Automated quantification of the 3D co-localization of iDelta$_{20}$ and fluorescent-protein-tagged Sara in the different backgrounds (see Methods). The degree of colocalization of the iDelta$_{20}$ signal in Sara–FP vesicles was, as in control, around 80% amongst all the genotypes studied here (Kruskal–Wallis non parametric ANOVA followed by Dunn's post-hoc test; *N*, number of cells; *n*, number of endosomes). Indeed, for all the genotypes, differences in the percentage of co-localization with respect to the control were not statistically significant, with exception of *Patronin*^{RNAi} (asterisk, $P < 0.05$) where the co-localization is slightly lower than in control (about 12% difference). **c**–**h**, Dynamics of FP–Sara endosomes during SOP mitosis in all the genotypes considered in this study. Dividing SOPs showing FP–Sara endosomes in the different backgrounds studied in this report (SDCM imaging; maximum-intensity *z* projection, except for GFP–Patronin channel in **h**, which corresponds to single planes). Imaging was performed in the animal, without dissection. The dynamics of FP–Sara endosomes (spindle targeting or not, asymmetric segregation or not, and so on) parallels what we report for iDelta$_{20}$ endosomes throughout this study. **i**, Dynamics of the percentage of Sara endosomes at the central spindle and of endosome asymmetry measured simultaneously in control SOPs (dark line, mean; lighter area, s.e.m.). Sara endosomes become asymmetric upon spindle targeting. Time was registered between videos (see Methods) and time point zero corresponds to anaphase B onset. *n*, number of cells. Note that, for comparison, the plot of percentage of Sara endosomes at the central spindle shown here is the same as Fig. 1f. Scale bars, 5 μm.

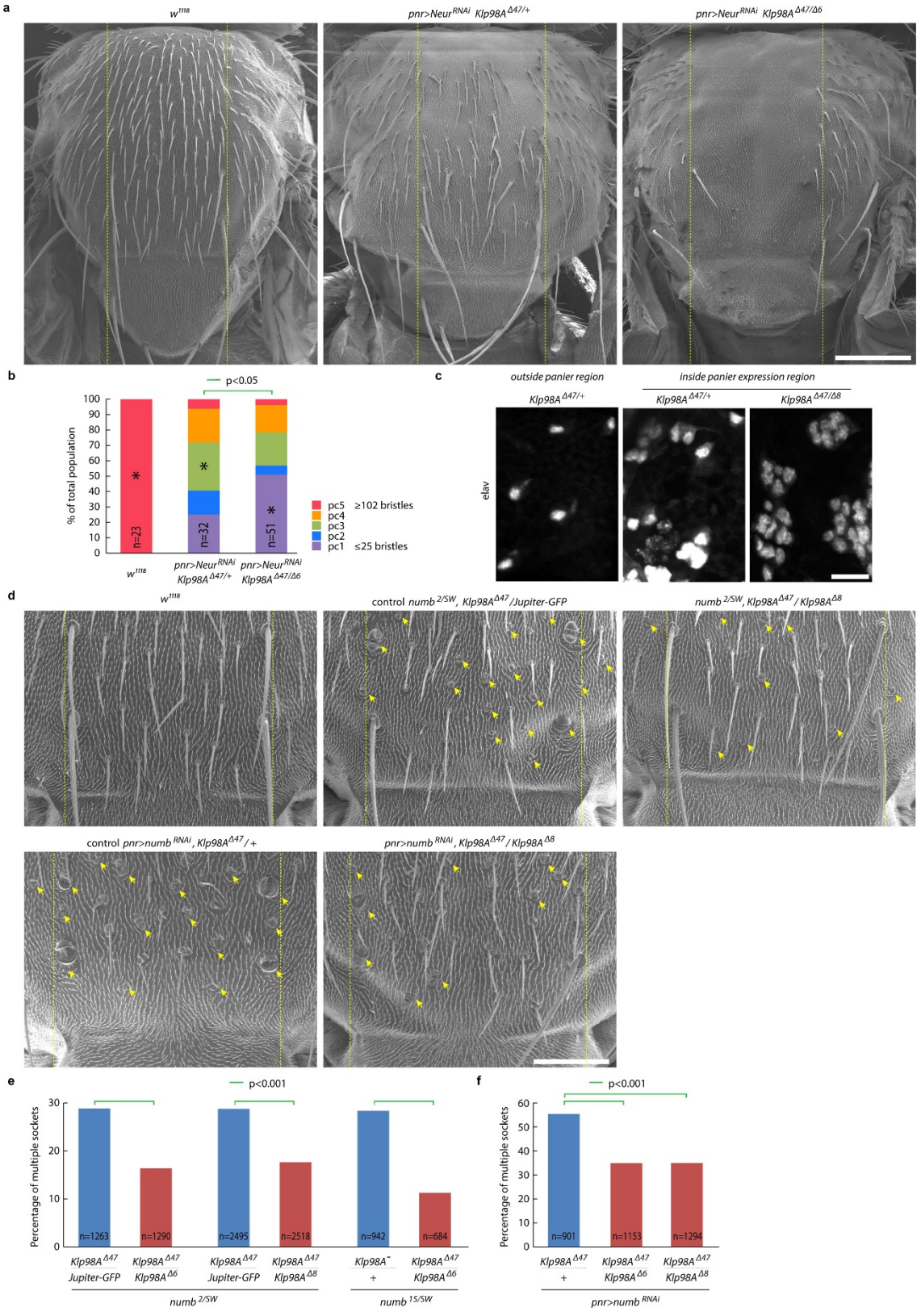

Extended Data Figure 3 | See next page for caption.

Extended Data Figure 3 | *Klp98A* mutants affects asymmetric cell fate assignation in conditions where Neuralized or Numb are compromised. See also 'Rationale and quantification of the Neur and Numb phenotypes' in Methods. **a**–**c**, *Klp98A* mutants show asymmetric cell fate assignation phenotypes in conditions where Neuralized is compromised. **a**, Scanning electron microscopy (SEM) images of adult w^{1118} control, *pnr* > $Neur^{RNAi}$ $Klp98A^{\Delta 47}/Klp98A^{\Delta 6}$ double mutant flies and *pnr* > $Neur^{RNAi}$ $Klp98A^{\Delta 47}/+$ sibling controls (see 'Detailed genotypes' in Methods). Yellow dashed lines delimit the *panier* expression region corresponding to the region between the right and left pairs of dorso-central macrochaetes. For each genotype, the image corresponds to the most frequent phenotypic class in the population (asterisk in the statistical distribution shown in **b**). Scale bar, 200 μm. **b**, Number of organs in the *panier* expression region scored on SEM images for the genotypes shown in a (for scoring criteria, see 'Quantification of the *Neur* and *Numb* phenotypes' in Methods). Five phenotypic classes of equal range of bristles (pc1–pc5) were considered, spanning from 0 bristles (stronger phenotype) to 130 bristles (maximum number of bristles scored in control flies). n, number of flies scored. The number of lineages which generated bristles is significantly reduced in *pnr* > $Neur^{RNAi}$ $Klp98A^{\Delta 47}/Klp98A^{\Delta 6}$ double mutant flies compared to $Klp98A^{\Delta 47}/+$ heterozygous sibling controls (χ^2 test, $P < 0.05$). **c**, SOPs are specified in *pnr* > $neur^{RNAi}$ $Klp98A^{\Delta 47}/Klp98A^{\Delta 8}$ double mutants. Neuron-specific elav staining of nota in *pnr* > $neur^{RNAi}$ $Klp98A^{\Delta 47}/+$ sibling controls (inside and outside the *panier* expression region) and of *pnr* > $neur^{RNAi}$ $Klp98A^{\Delta 47}/Klp98A^{\Delta 8}$ double mutants (inside the *panier* expression region). Note that neurons are present in *pnr* > $neur^{RNAi}$ $Klp98A^{\Delta 47}/Klp98A^{\Delta 8}$ double mutants, indicating that in this mutant SOPs were specified. Scale bar, 10 μm. **d**–**f**, *Klp98A* mutants suppress cell fate assignation phenotypes in hypomorphic *Numb* mutants. **d**, SEM images of adult w^{1118} control, $Numb^{2}/Numb^{SW}$; $Klp98A^{\Delta 8}/Klp98A^{\Delta 47}$ double mutant and its $Numb^{2}/Numb^{SW}$; *Jupiter-GFP*/$Klp98A^{\Delta 47}$ sibling control, *pnr* > $numb^{RNAi}$ $Klp98A^{\Delta 47}/+$ control and *pnr* > $numb^{RNAi}$ $Klp98A^{\Delta 47}/Klp98A^{\Delta 8}$ double mutant. In this panel and as well as **e** and **f**, we used a Jupiter–GFP knock-in as a control chromosome. Arrows indicate organs with multiple sockets, characteristic of Numb mutants. This phenotype is suppressed in Klp98A mutants. Scale bar, 100 μm. Yellow dashed lines delimit the *panier* expression region where phenotypes were scored (also in the $Numb^{SW}$ conditions). **e**, Percentage of total organs showing multiple sockets in the *panier* expression region, scored on SEM images in $Numb^{2}/Numb^{SW}$; $Klp98A^{\Delta 6}/Klp98A^{\Delta 47}$ double mutants (and its $Numb^{2}/Numb^{SW}$; *Jupiter-GFP*/$Klp98A^{\Delta 47}$ sibling controls), $Numb^{2}/Numb^{SW}$; $Klp98A^{\Delta 8}/Klp98A^{\Delta 47}$ double mutants (and its $Numb^{2}/Numb^{SW}$; *Jupiter-GFP*/$Klp98A^{\Delta 47}$ sibling controls) and $Numb^{15}/Numb^{SW}$; $Klp98A^{\Delta 6/}Klp98A^{\Delta 47}$ double mutants (and its $Numb^{15}/Numb^{SW}$; $Klp98A^{\Delta 47}$/*TM6B* or $Numb^{15}/Numb^{SW}$; $Klp98A^{\Delta 6}$/*TM6B* sibling controls). All double mutants show a significant reduction of the percentage of multiple sockets when compared to their respective sibling control (χ^2 test, $P < 0.001$). n, total number of microchaete scored. **f**, Percentage of total organs showing multiple sockets in the *panier* expression region in *pnr* > $numb^{RNAi}$ $Klp98A^{\Delta 47}/+$ controls, *pnr* > $numb^{RNAi}$ $Klp98A^{\Delta 47}/Klp98A^{\Delta 6}$ double mutants and *pnr* > $numb^{RNAi}$ $Klp98A^{\Delta 47}/Klp98A^{\Delta 8}$ double mutants. Both mutants show a significant reduction of the percentage of multiple sockets when compared to the control (χ^2 test, $P < 0.001$).

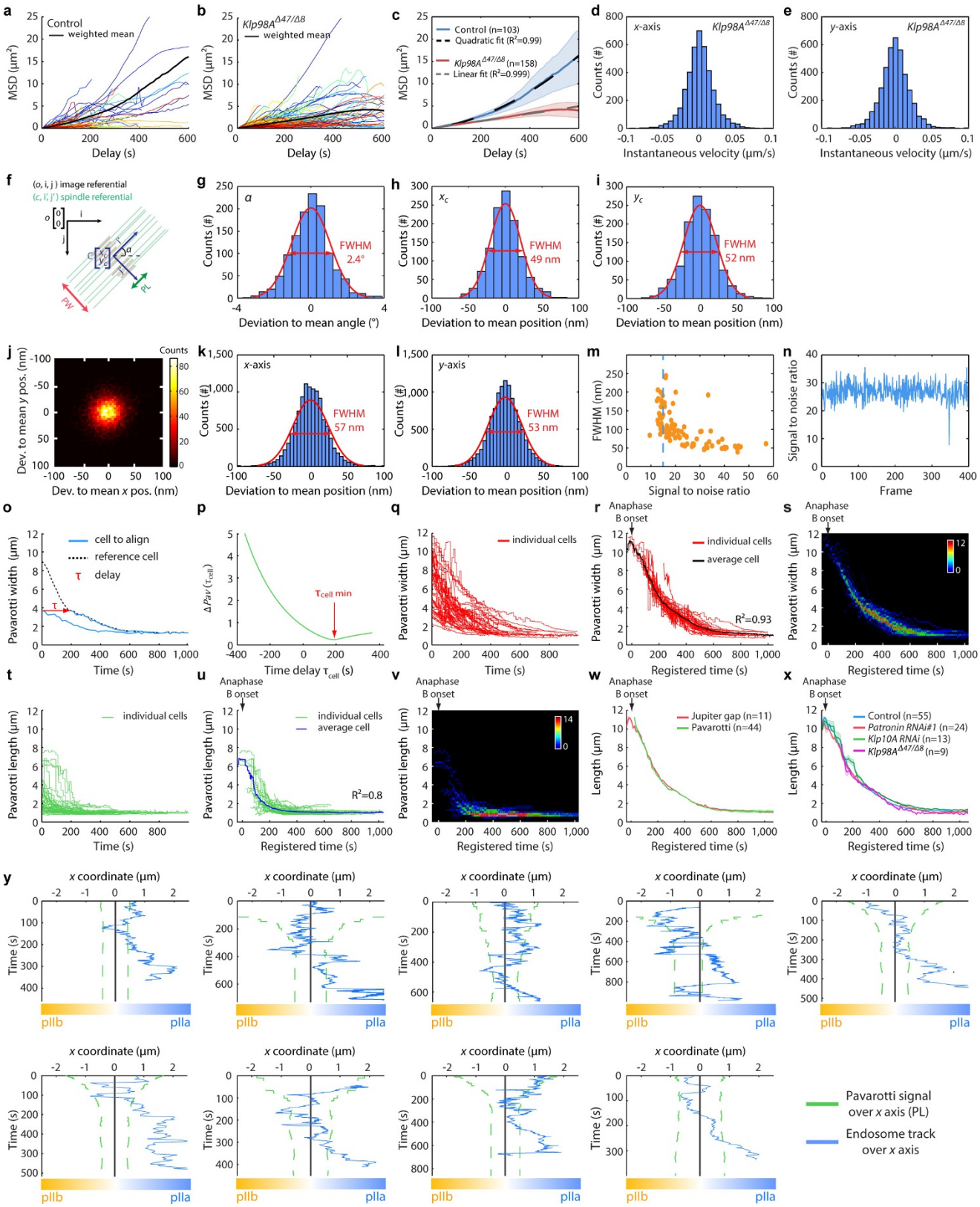

Extended Data Figure 4 | See next page for caption.

Extended Data Figure 4 | MSD analysis of endosome tracks and precision of the tracking algorithms. **a**–**e**, Determination of the endosome diffusion coefficient (see also 'Mean square displacement analysis of endosome tracks' in Methods). **a**–**b**, MSD individual traces as a function of delay time for each endosome track: $n = 103$ tracks in control SOPs (**a**) and $n = 158$ in $Klp98A^{\Delta 47/\Delta 8}$ SOPs (**b**). The thick black line corresponds to the weighted mean curve[61], which weighs the MSD curves according to their certainty (see Methods). **c**, Parabolic or linear fitting of the weighted MSD as a function of delay time in control and Klp98A$^-$ SOPs (for details see Methods). Dark line, weighted mean; lighter area, s.e.m. In the absence of motor activity in the Klp98A null mutant, a linear fit reflects diffusive movement. In the control, a parabolic fit reflects a directed movement as a consequence of Klp98A motor activity. **d**, **e**, Histogram of instantaneous velocities of Sara endosomes in $Klp98A^{\Delta 47/\Delta 8}$ mutant SOPs along x (**d**) and y (**e**) axes. **f**–**i**, Precision of the Pavarotti tracking algorithm. **f**, Scheme showing the two reference frames (image reference frame and central spindle reference frame) considered in the tracking analysis. For details see 'Spatio-temporal registration' in Methods. **g**–**i**, Histograms of the deviation from the mean value of α (**g**), x_c (**h**) and y_c (**i**) from videos of fixed tissue. FWHM values shown in the histograms correspond to the accuracy of each parameter. **j**–**n**, Accuracy of our iDelta$_{20}$ detection and tracking method. **j**–**l**, 100 iDelta$_{20}$ endosomes were tracked in fixed material and the deviation to their mean x and y position was computed. Deviations are represented either as a 2D density plot (**j**) or decomposed in histograms along the x axis (**k**) and the y axis (**l**). FWHM measurements indicate a positional accuracy of 57 nm on the x axis and 53 nm on the y axis, respectively. **m**, Dependence of the tracking accuracy on the endosome signal-to-noise ratio (SNR) using videos of fixed tissue (see Methods). To ensure reliable iDelta$_{20}$ tracking, we only considered endosomes with an SNR > 15 (dashed line). **n**, SNR of a single iDelta$_{20}$ endosome from a video of a fixed tissue imaged under constant laser illumination. Each time point corresponds to a 3D stack of seven slices through the central spindle. The SNR remains constant throughout iterative laser excitation of Atto647N fluorophore, indicating high photostability of this fluorophore and, therefore, that iDelta$_{20}$ tracking accuracy does not decrease over time due to bleaching. **o**, **p**, Principle of the time registration method using the PW dynamics. Since the temporal profile of Pavarotti contraction is stereotypic, each cell can be aligned in time with a reference cell by determining the time delay τ_{cell} that needs to be applied to this cell of interest in order to minimize the difference, in absolute value, between the two temporal profiles (**o**) (that is, find the τ_{cell} for which $\Delta\mathrm{Pav}(\tau_{cell}) = \sum_{t=0}^{t=t_n} |\mathrm{PW}_{cell}(t+\tau_{cell}) - \mathrm{PW}_{ref}(t)|$ is minimum (**p**)). **q**, **t**, Unregis**t**ered PW (**q**) and PL (**t**) curves of 45 cells. **r**, **u**, Same data set as in **q** and **t**, but upon **t**ime registration. In this panel and others in this report, the time point zero in registered time corresponds to anaphase B onset (that is, when PW starts to contract). **s**, **v**, Same plot as in **r** and **u**, but represented as a density plot to show the collapse of the temporal profiles upon registration (rainbow lookup table). Note that the registered PL curves (which were not used in the registration process based on PW) also collapse, validating the method. **w**, Average temporal contraction profile of PW and 'Jupiter gap' (see Methods). Since Jupiter is excluded from the region that Pavarotti occupies (see Fig. 3a), the absence of Jupiter (Jupiter gap, defined as a FWHM) can be used as a proxy of the Pavarotti region. The PW and Jupiter gap temporal profiles are very similar, thus either marker can be used for temporal registration. n, number of cells. **x**, Average PW/Jupiter gap temporal profiles in control, *Patronin* RNAi#1, *Klp10A* RNAi and *Klp98A* mutant conditions. The profiles are very similar: time registration can be applied to *Patronin* and *Klp10A* RNAi conditions, as well as to *Klp98A* mutants. n, number of cells. **y**, Examples of bidirectional movements on the central spindle. iDelta$_{20}$ endosomes were automatically tracked during mitosis of GFP–Pavarotti expressing cells. Movement of nine endosomes on the x axis of the central spindle is shown. Green dashed line indicates PL over time. iDelta$_{20}$ tracks are mostly confined within the Pavarotti-positive region containing the antiparallel overlap until their departure. Tracks explore both sides of the Pavarotti positive region, but do it more often and deeper on the pIIa side.

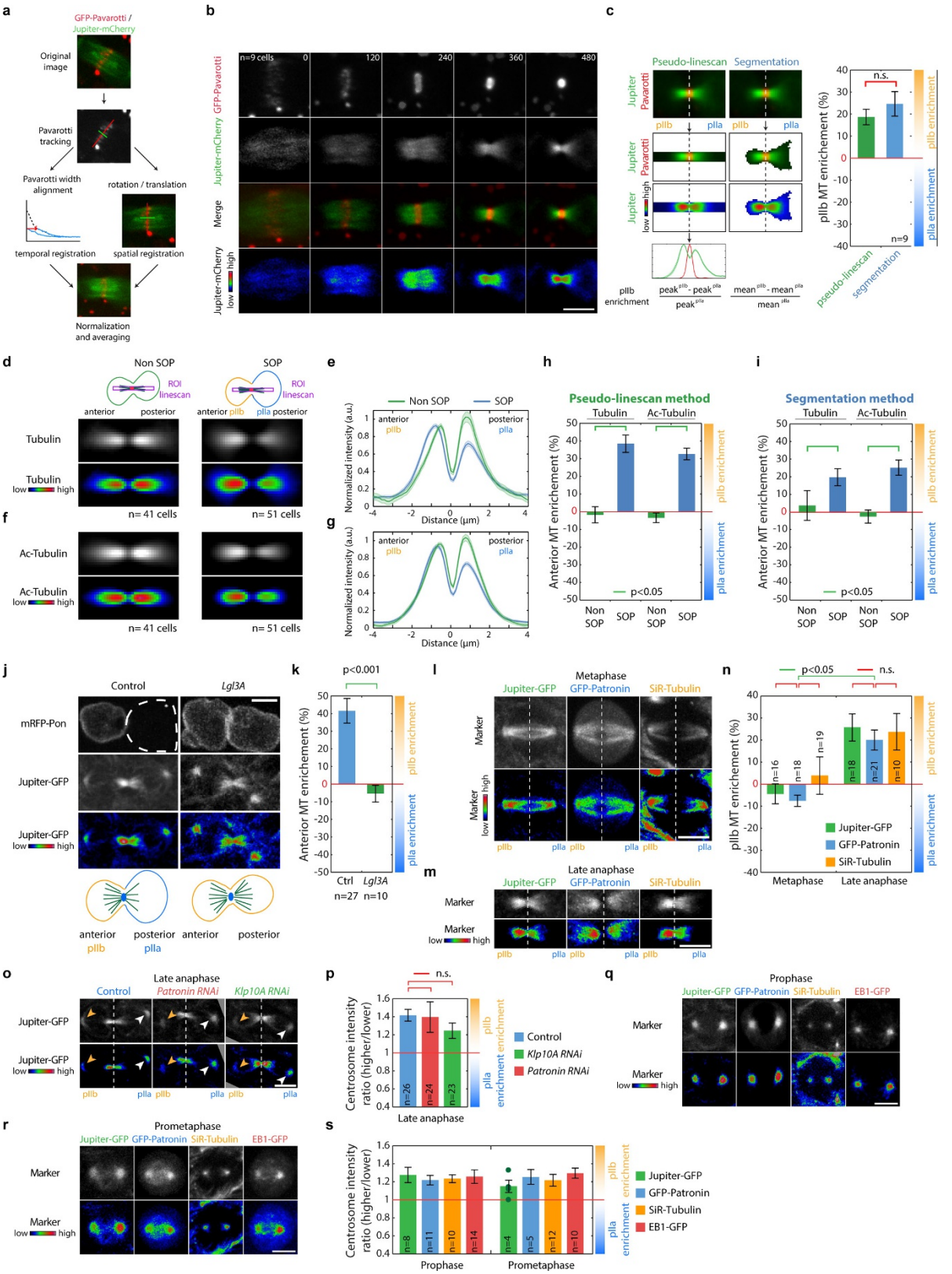

Extended Data Figure 5 | See next page for caption.

Extended Data Figure 5 | The central spindle of SOPs is asymmetric. **a**, **b**, Generation of the 'average SOP cell'. **a**, Principle of the spindle averaging technique. Dividing SOPs expressing GFP–Pavarotti and Jupiter–mCherry were imaged by SDCM (*z* projection). Pavarotti signal was subsequently tracked to register all the movies in space and time before averaging. **b**, Time frames from a time-lapse average video of nine dividing SOPs. The central spindle is asymmetrical, with an enrichment of Jupiter density on the pIIb side (left). Elapsed time in seconds. **c**–**i**, The central spindle of SOPs is asymmetric. **c**, Left two panels: illustration of the two methods (pseudo-line-scan and segmentation method) used to measure central spindle asymmetry (see 'Measurement of spindle asymmetry in anaphase' in Methods). Right panel, Jupiter–mCherry enrichment in pIIb as scored with either method. Samples are the same as in Fig. 3a. Both methods gave comparable results when applied to the samples in Fig. 3a, but also to immunofluorescence of endogenous tubulin in fixed samples (see **h**, **i**). **d**–**g**, Average central spindle images (**d**, **f**) and line scan (**e**, **g**; line scan is based on the ROI shown in the top panels in **d** of both SOP and neighbouring epithelial cells (non-SOP) immunolabelled using Oregon Green-514 anti-β-tubulin antibodies and Atto647N anti-acetylated-α-tubulin antibodies. SDCM imaging with sum projection to generate an average cell (see 'Image averaging' chapter in Methods). Anterior to the left as determined by the mRFP–Pon signal (not shown). Central spindles of SOPs are asymmetric, with an enrichment of tubulin and a corresponding enrichment of acetylated-tubulin on the pIIb side of the spindle, while non-SOP central spindles are symmetric. **h**, **i**, Tubulin and acetylated tubulin enrichment in the anterior pIIb cell in SOPs and anterior cells in non-SOP mitoses in the samples presented in **d** and **f** using either the pseudo-line-scan or the segmentation methods as in **c**. Note that the non-SOP cells do not show a statistically significant enrichments (zero enrichment is within the s.e.m. of the samples), while SOP cells do. Confirming this, a Kruskal–Wallis non-parametric ANOVA followed by Dunn's post hoc test ($P < 0.05$) shows that in SOP cells the anterior (pIIb) enrichment of microtubule markers is higher than in non-SOP cells. These statements are true whether the line scan or the segmentation methods are considered. $n = 47$ for *n*on-SOP and 57 for SOP cells. **j**, **k**, Spindle asymmetry occurs downstream of Par complex signalling. **j**, Representative dividing control or *lgl3A*-expressing SOPs showing mRFP–Pon and Jupiter–GFP. Upon *lgl3A* overexpression, Pon segregation becomes symmetrical. Central spindle asymmetry (Jupiter–GFP channel) is also abolished upon *lgl3A* expression. Note that the control panel is the same as Fig. 3g, shown here for comparison. **k**, Jupiter–GFP enrichment in anterior pIIb daughters (control) or in anterior daughters (*lgl3A*) at late cytokinesis. $P < 0.001$ (Mann–Whitney test). **l**–**s**, Analysis of spindle asymmetries from early- to late-mitotic phases (see also 'Centrosome asymmetry' in the Supplementary Discussion). **l**–**n**, Spindle asymmetry occurs late during SOP mitosis. Dividing SOPs showing Jupiter–GFP, GFP–Patronin or SiR-tubulin in metaphase (**l**) or late anaphase (**m**, ~600 s registered ti**m**e). Antero-posterior orientation is based on the mRFP–Pon cortical signal (not shown). **n**, Jupiter–GFP, GFP–Patronin or SiR-tubulin enrichment in the pIIb side of the spindle ($100 \times \frac{(\rho_b - \rho_a)}{\rho_a}$; ρ_a, pIIa density; ρ_b, pIIb) in metaphase or late anaphase. While the spindle is not asymmetric in metaphase, in late anaphase, the density of Jupiter–GFP, GFP–Patronin and SiR-tubulin is enriched in the pIIb side compared to pIIa. Statistics were performed using a Kruskal–Wallis non-parametric ANOVA followed by Dunn's post hoc test ($P < 0.05$). **o**, **p**, Centrosome asymmetry in anaphase is unaffected upon Patronin or Klp10A depletion. **o**, SOPs in late anaphase showing Jupiter–GFP in control, Patronin-depleted or Klp10A-depleted conditions. The centrosome in pIIa (white arrow) is brighter than that in pIIb (orange arrow) in all conditions. **p**, Intensity ratio of Jupiter–GFP signal in the pIIa centrosome over the pIIb centrosome in control, Patronin- and Klp10A-depleted SOPs in late anaphase (mean ± s.e.m.). In control, the enrichment of Jupiter–GFP in the pIIa centrosome is statistically significant (the s.e.m. does not cross the ratio = 1 line). In Patronin and Klp10A depletion this asymmetry is not statistically different to that of control (Kruskal–Wallis non-parametric ANOVA followed by Dunn's post hoc test). Note that in control cells, in the central spindle, it is the anterior pIIb (not the posterior pIIa) side that shows a higher density of microtubules. This observation untangles the asymmetry of the centrosomes from the asymmetry of the central spindle. Consistent with this, in Patronin depletion and Klp10A depletion conditions, central spindle asymmetry is abolished (see here, but also Fig. 3e, g, h), while centrosome asymmetry is not affected. **q**–**s**, Centrosome asymmetry can be detected before anaphase. Dividing SOPs showing Jupiter–GFP, GFP–Patronin, SiR-tubulin and EB1–GFP in prophase (**q**) or prometaphase (**r**). All four markers show a signal enrichment in one centrosome compared to the other, suggesting different microtubule-organizing activities of the two centrosomes. **s**, Intensity ratio of the centrosome-associated signals of Jupiter–GFP, GFP–Patronin, SiR-tubulin and EB1–GFP in prophase and prometaphase. Here, the pIIa/pIIb identity of the centrosome could not be determined since the mitotic spindle rotates in metaphase. We thus plotted the ratio of the brightest over the dimer centrosome. This suggests that centrosome asymmetry is acquired early, perhaps due to centrosome age. However, it must be noted that centrosome asymmetry is untangled from central spindle asymmetry. Individual data points are figured when number of cell scored is inferior to 5. All images in this figure correspond to SDCM imaging (maximum-intensity projection). Scale bars, 5 μm. Lower panels in **b**–**d**, **f**, **j**–**m**, **o**, **q**, **r** correspond to rainbow lookup table. n, number of cells scored.

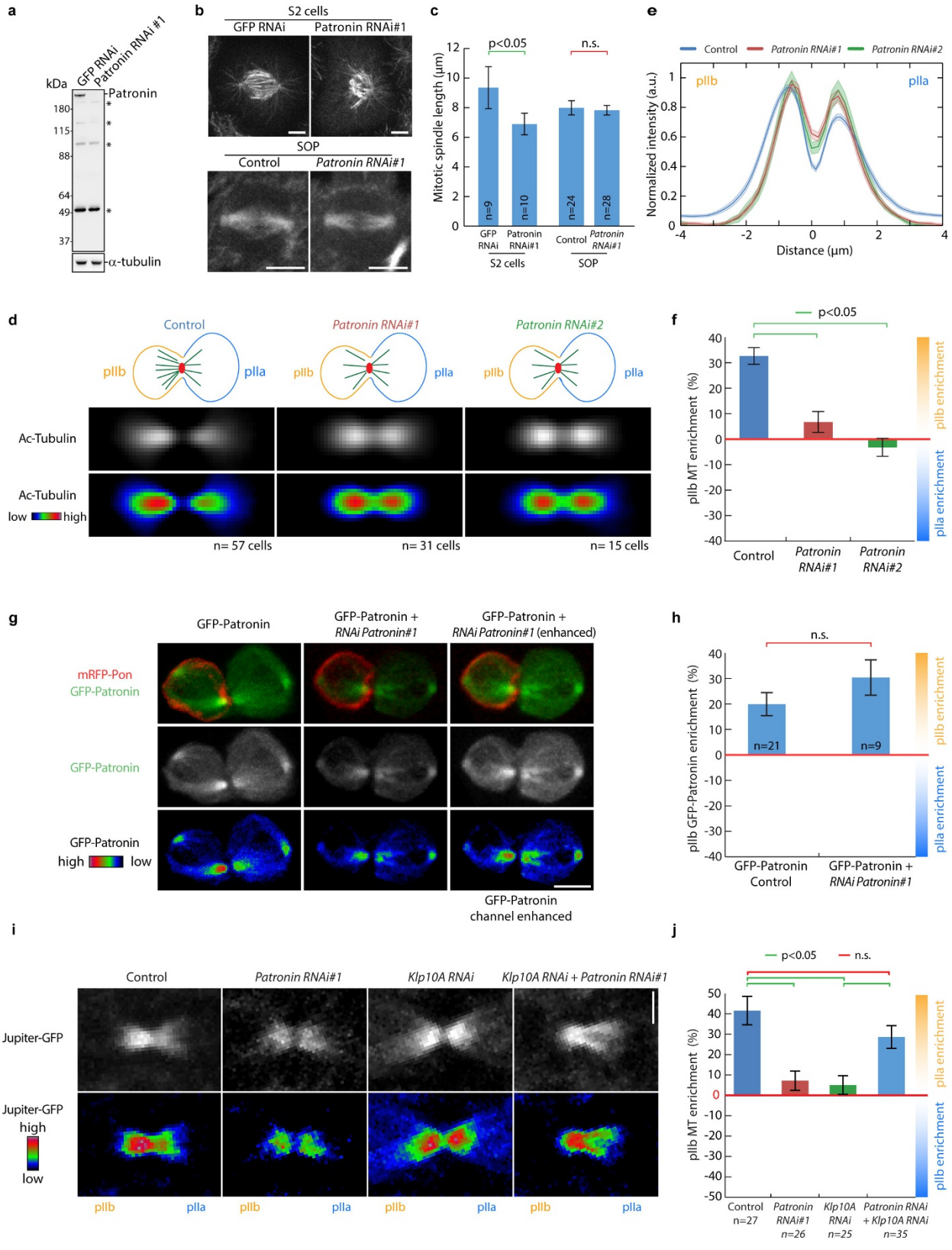

Extended Data Figure 6 | See next page for caption.

Extended Data Figure 6 | Patronin controls central spindle asymmetry. **a**, Validation of the anti-Patronin antibody and of the depletion of Patronin by the *Patronin* RNAi#1 sequence. Anti-Patronin western blot of total extracts of S2 cells treated with *GFP* RNAi or *Patronin* RNAi#1. Patronin corresponds to the major band above 180 kDa that disappears upon RNAi treatment, validating both the RNAi sequence and the antibody. The *Patronin* RNAi construct presented in the main text corresponds to this *Patronin* RNAi #1. Asterisks indicate non-specific bands. Western blot is representative of two experiments. For source gel images, see Supplementary Fig. 1. **b**, **c**, Validation, in S2 cells, of the *Patronin* RNAi#1 sequence used in the SOP. **b**, Upper panel, α-tubulin immunofluorescence of S2 cells treated with *GFP* RNAi or *Patronin* RNAi#1 in metaphase. Lower panel, Jupiter–GFP signal control and *Patronin* RNAi#1 depleted SOPs in metaphase. Live imaging. **c**, Measurement of the spindle pole to spindle pole distance of metaphase spindles in the samples described in **b**. Statistics were performed using a Kruskal–Wallis non-parametric ANOVA followed by Dunn's post hoc test; $P < 0.05$. Similar to what was reported by Goodwin and Vale (ref. 16) using a different RNAi sequence, depletion of Patronin in S2 cells by our *Patronin* RNAi#1 leads to short and disorganized mitotic spindles. This is however not the case in the SOP: the mitotic spindle is neither short nor disorganized. The difference between the SOP and S2 cells can be explained by the different levels of expression of the RNAi in the two systems: in the SOP, a milder Patronin depletion does allow the cell to proceed to anaphase without metaphase spindle defects/arrest. Later, the SOP central spindle seems to be more sensitive than the metaphase spindle and it is affected by our conditions of Patronin depletion in the SOP: it becomes symmetric (see below and Fig. 3e, g, h). **d**, **e**, Average central spindle images (**d**) and line scan (**e**; line scan is based on a ROI, as shown in Extended Data Fig. 5c) of both control and Patronin-depleted SOPs immunolabelled using Atto647N anti-acetylated-α-tubulin antibodies. SDCM imaging with sum projection to generate an average cell (see 'Image averaging' in Methods). Anterior to the left as determined by the mRFP–Pon signal (not shown). Spindle asymmetry is abolished upon Patronin depletion by two independent RNAi sequences. *Patronin* RNAi#1 is referred as *Patronin* RNAi in the main text. Note that the control line scan is the same as Extended Data Fig. 5g, shown here for comparison. **f**, Acetylated tubulin enrichment in the pIIb cell in control and Patronin-depleted SOPs measured by the pseudo-line-scan method (see Extended Data Fig. 5c). pIIb microtubule enrichment is defined as $100 \times \frac{(I_b - I_a)}{I_a}$, with I_b and I_b the respective pIIb and pIIa peak values of the linescans shown in **e**. The asymmetry of the central spindle is significantly reduced upon Patronin depletion (Kruskal–Wallis non-parametric ANOVA followed by Dunn's post hoc test; $P < 0.05$). Note that the control data set is the same as Extended Data Fig. 5h, shown here for comparison. **g**, **h**, Specificity of the central spindle symmetry phenotype by *Patronin* RNAi#1 as shown in Fig. 3e, g, h: rescue of the effects of RNAi-induced Patronin depletion by overexpression of GFP–Patronin. **g**, Representative dividing SOPs expressing mRFP–Pon and GFP–Patronin (GFP–Patronin control; left panel) or, in addition, expressing *Patronin* RNAi#1 (GFP–*Patronin* + *Patronin* RNAi#1; middle and right panels) at late cytokinesis. SDCM imaging, *z* projection. RNAi-mediated depletion is rescued by GFP–Patronin overexpression mediated by the UAS/Gal4 system. Note that, in the RNAi conditions, the GFP–Patronin signal is reduced, reflecting the fact that the GFP–Patronin mRNA is targeted by RNAi; see, for example, GFP–Patronin signal in central versus left panels. Spindle asymmetry is rescued upon overexpression of GFP–Patronin in the RNAi condition (see right panel, where the brightness has been enhanced to visualize the different microtubule levels of the spindle). **h**, GFP–Patronin enrichment in the pIIb cell in control and rescued SOPs as in **g**. Enrichment in both conditions is not statistically significant ($P = 0.175$; Mann–Whitney test). **i**, **j**, Co-depletion of Klp10A and Patronin suppresses their respective phenotype on central spindle asymmetry. **i**, Central spindle in dividing control, Patronin-, Klp10A-depleted and Patronin/Klp10A-co-depleted SOPs expressing Jupiter–GFP (SDCM, *z* projection). Antero-posterior orientation is based on the mRFP–Pon signal (not shown). Note that, upon co-depletion of Patronin and Klp10A, the phenotype of symmetric central spindle observed in *Patronin* and *Klp10A* RNAi conditions is suppressed to recover the levels of asymmetry observed in the control situation (see lookup table image; bottom panels). **j**, Quantification of GFP–Jupiter signal enrichment in the pIIb cell in control and depleted/co-depleted SOPs as in **i**. The asymmetry of the central spindle is significantly reduced upon Patronin or Klp10A depletion, but restored to control levels upon co-depletion of Patronin and Klp10A (Kruskal–Wallis non-parametric ANOVA followed by Dunn's post hoc test; $P < 0.05$). Note that the control data set is the same as Extended Data Fig. 5k, shown here for comparison. Lower panels in **d**, **g** and **i** correspond to the rainbow lookup table. n, number of cells scored. Scale bars, 5 μm (**b**, **g**) and 2 μm (**i**).

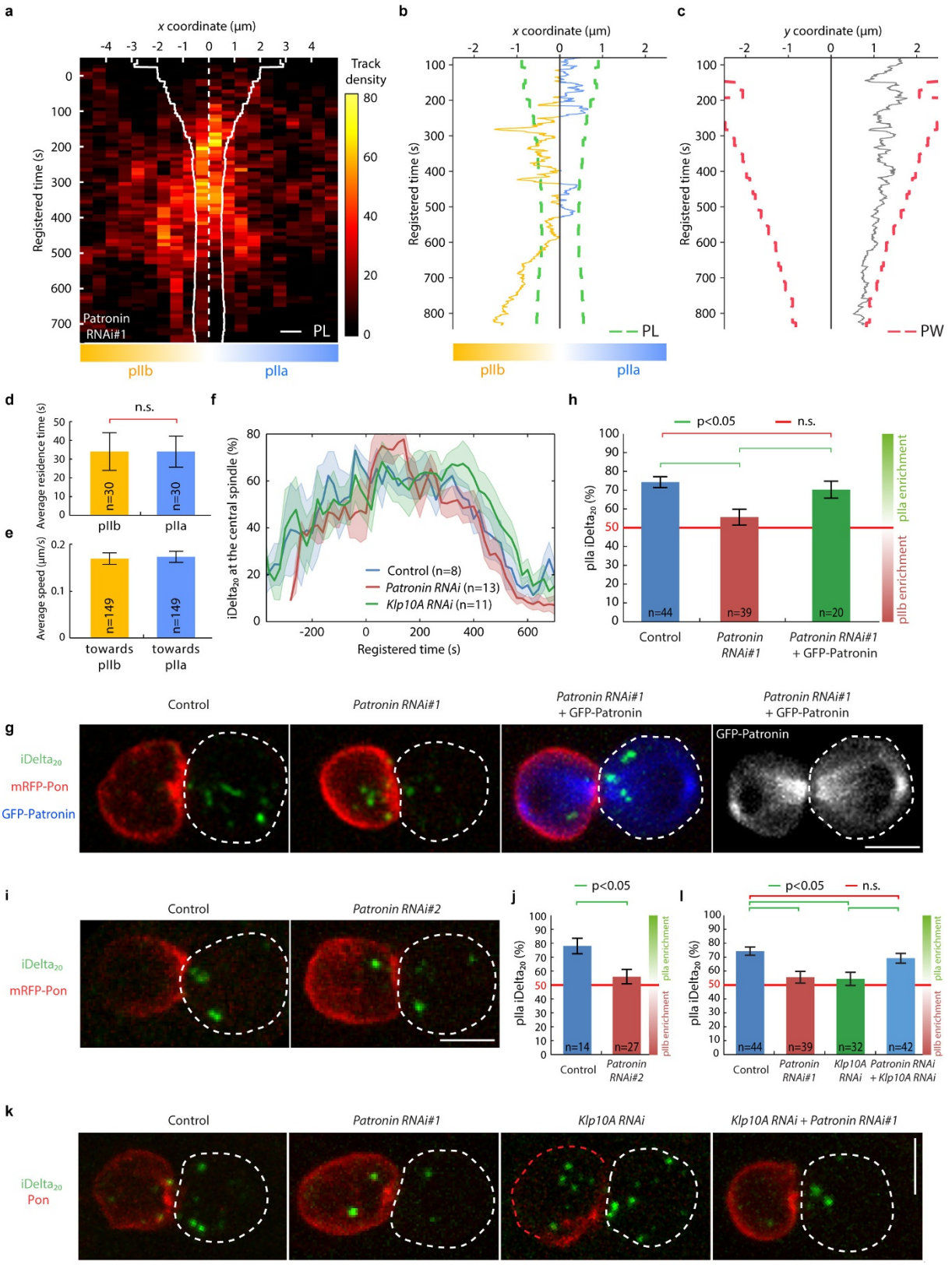

Extended Data Figure 7 | See next page for caption.

Extended Data Figure 7 | Impaired spindle asymmetry and asymmetric Sara endosome segregation upon Patronin depletion. a–**e**, Endosome motility analysis in *Patronin* RNAi#1 condition. **a**, Spatio-temporal density plot of iDelta$_{20}$ endosomes at the central spindle in Patronin-depleted cells. iDelta$_{20}$ endosomes were automatically tracked during mitosis of ten cells expressing GFP–Pavarotti and *Patronin* RNAi#1. After spatial registration of each track with respect to its own central spindle reference frame and temporal registration using PW constriction, the resulting 1,541 tracks were all plotted as a spatio-temporal density map (*x* axis, time). Overlaid continuous white line, averaged Pavarotti length (PL); dashed line, centroid of the Pavarotti region. iDelta$_{20}$ tracks are enriched within the Pavarotti-positive region. In contrast to control, tracks explore approximately equally both sides beyond the Pavarotti-positive region. **b**, **c**, Representative endosome track, decomposed on the *x* (**b**) and *y* (**c**) axes. On the *x* axis, movement is bidirectional and mostly confined within the Pavarotti-positive region. On the *y* axis, movements are limited or at most follow the contraction of the PW. **d**, Velocity of microtubule-based motility towards the pIIa or the pIIb cells during bidirectional movement on the *x* axis. Speed does not depend on orientation of the movement ($n = 149$ strides in 45 tracks; non-significant in Mann–Whitney test). **e**, Residence time of endosomes within both cells during bidirectional movement. In contrast to the control, there is no bias ($n = 30$ endosome tracks; non-significant in Mann–Whitney test). **f**, Dynamics of the percentage of iDelta$_{20}$ endosomes at the central spindle in control, Patronin- and Klp10A-depleted SOPs as in Fig. 1f (dark line, mean; lighter area, s.e.m.). iDelta$_{20}$ endosomes reach the central spindle in Patronin- and Klp10A-depleted cells with similar kinetics than in control cells. Note that the control data set is the same as Fig. 1f, shown here for comparison. **g**, **h**, Specificity of the endosomal targeting symmetry phenotype induced by *Patronin* RNAi#1 as shown in Fig. 4a, b: overexpression of GFP–Patronin rescues the effects of *Patronin* RNAi#1 on Sara endosome asymmetric segregation. **g**, Representative dividing SOP showing mRFP–Pon and iDelta$_{20}$ (control), or, in addition, expressing *Patronin* RNAi#1, or *Patronin* RNAi#1 and GFP–Patronin (GFP–Patronin + *Patronin* RNAi#1, third and fourth panels) at late cytokinesis. SDCM imaging, *z* projection. Sara endosome symmetric segregation induced by *Patronin* RNAi#1 expression is rescued by overexpression of GFP–Patronin. Note that spindle asymmetry is also rescued (fourth panel), as shown above in Extended Data Fig. 6g, h. **h**, Percentage of iDelta$_{20}$ in the pIIa daughter cell at late cytokinesis in control, *Patronin* RNAi#1-treated and rescued cells (GFP–Patronin + *Patronin* RNAi#1). GFP–Patronin expression rescued the symmetric iDelta$_{20}$ segregation induced by the *Patronin* RNAi#1 (ANOVA test followed by Holm–Sidak post hoc test). **i**, **j**, Confirmation of the effects of Patronin depletion on Sara endosome asymmetric segregation by an independent RNAi sequence, *Patronin* RNAi#2. **i**, Representative control or *Patronin* RNAi#2-treated SOPs showing mRFP–Pon and iDelta$_{20}$ at late cytokinesis. SDCM imaging, *z* projection. **j**, Percentage of iDelta$_{20}$ in pIIa at late cytokinesis in control and *Patronin* RNAi#2-treated cells. iDelta$_{20}$ percentage in pIIa is significantly lower upon Patronin depletion ($P < 0.05$; unpaired two-tailed *t*-test). **k**, **l**, Co-depletion of Klp10A and Patronin suppresses their respective phenotype on endosome asymmetry. **k**, Control, Patronin-, Klp10A-depleted and Patronin/Klp10A-co-depleted SOPs showing mRFP–Pon and iDelta$_{20}$ in late cytokinesis. SDCM imaging, *z* projection. **l**, Percentage of iDelta$_{20}$ in the pIIa daughter cell at late cytokinesis in control, Patronin-, Klp10A-depleted and Patronin/Klp10A-co-depleted SOPs. Note that the control, *Patronin* RNAi and *Klp10A* RNAi data sets are the same as Fig. 4b, shown here for comparison. Endosome segregation becomes symmetrical upon Patronin or Klp10A depletion, but is restored to control levels upon co-depletion of Patronin and Klp10A ($P < 0.05$; ANOVA followed by Tukey's post hoc test). Note that spindle asymmetry is also suppressed (Extended Data Fig. 6i, j). Unless stated otherwise, n corresponds to the number of SOP scored. Scale bars, 5 μm.

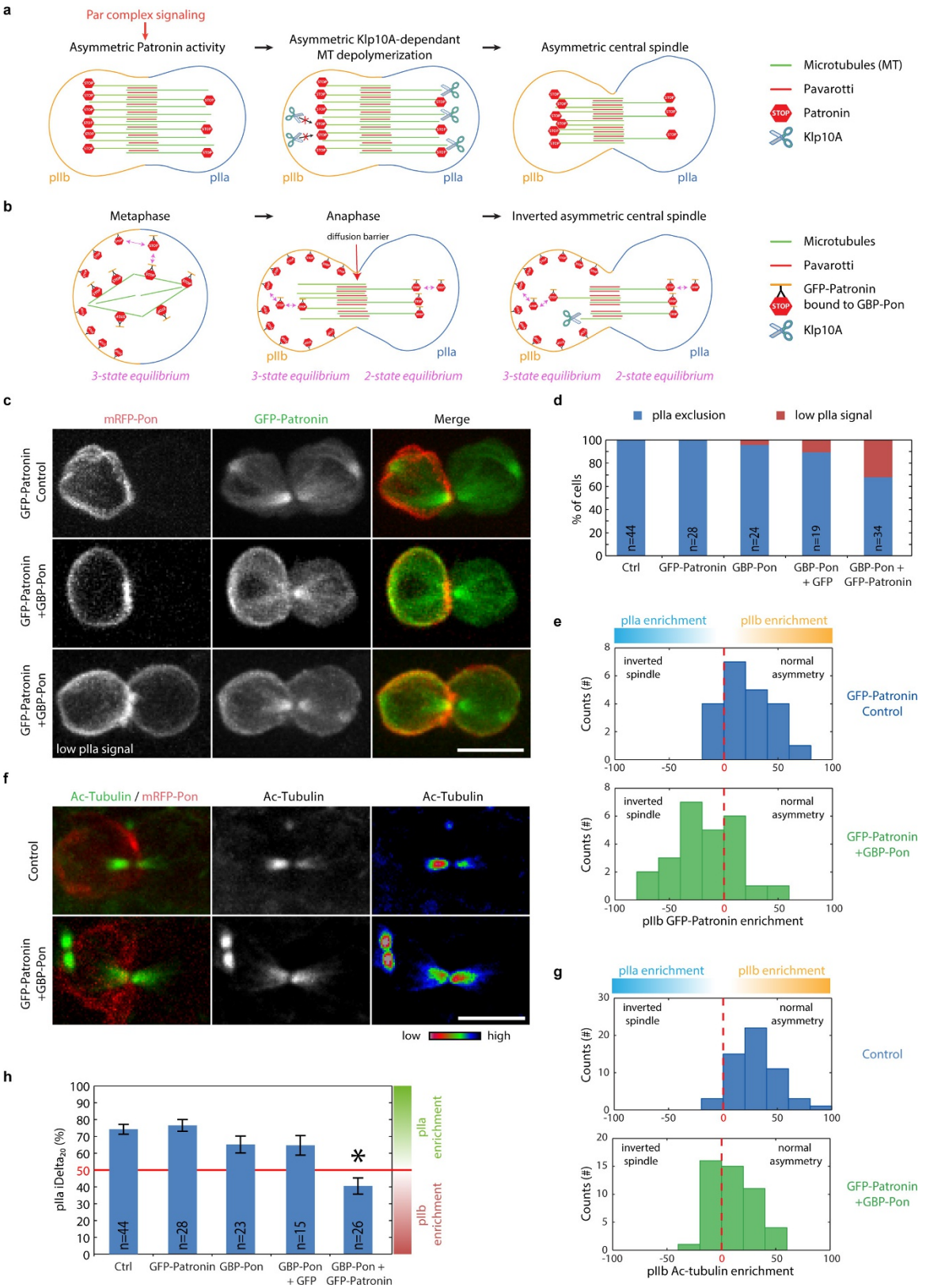

Extended Data Figure 8 | See next page for caption.

Extended Data Figure 8 | Inversion of central spindle asymmetry by the nanobody assay. a, Model of spindle asymmetry generation by the Patronin/Klp10A machinery. Directly or indirectly, Par complex signalling leads to a biased localization of Patronin, which is thereby enriched on the pIIb side of the central spindle (left panel). Patronin antagonizes Klp10A microtubule depolymerization activity and therefore net microtubule depolymerization activity is stronger on the pIIa side of the spindle (middle panel). As a consequence, the central spindle becomes asymmetric with a higher density in the pIIb side (right panel). **b**, Cartoon of the rationale of the 'nanobody assay' for central spindle inversion (see also 'Rationale of the nanobody experiment' in the Supplementary Discussion). Expression of an anti-GFP nanobody (GBP) fused to an anterior cortex localization domain (Pon; left panel) leads to the specific targeting of GFP-tagged molecules at the anterior cortex. Due to the high affinity of the GBP for GFP[66], most of the GFP–Patronin molecules are bound to the nanobody (see Extended Data Fig. 9a–d). Owing to the high off-rates of Pon for the cortex[67] and Patronin for the spindle (see Extended Data Fig. 9e) in metaphase, the Pon–GBP/GFP–Patronin complex is in three-state equilibrium between the cytosol, the anterior cortex and the spindle (left panel). In late anaphase, owing to the diffusion barrier at the central spindle (because of crowding), the situation becomes different in pIIa and pIIb: while in pIIb there is a three-state equilibrium (anterior cortex, cytosol, spindle), in pIIa there is only a two-state equilibrium (cytosol, spindle; middle panel). This generates an asymmetry of the amount of Patronin at the spindle: in pIIb there is an additional sink provided by the anterior cortex. As a consequence, the antagonistic activity of Patronin on Klp10a-mediated microtubule depolymerization is depleted in pIIb, thereby biasing microtubule density to higher levels in pIIa (right panel). **c**, Dividing SOPs expressing mRFP–Pon and GFP–Patronin (GFP–Patronin control) or, in addition, expressing GBP–Pon (GFP–Patronin + GBP–Pon) at late cytokinesis. Like in control cells (upper panel), polarized mRFP–Pon localization is observed upon co-expression of GBP–Pon and GFP–Patronin (middle panel) but, occasionally, low levels of mRFP–Pon are also detected in the pIIa cell cortex (lower panel). Note that the GFP–Patronin control panel is the same as Extended Data Fig. 6g, shown here for comparison. **d**, Frequency of the leaking pIIa mRFP–Pon signal upon expression of the indicated fusion proteins. Cells showing leaking Pon cortical localization in pIIa were excluded from the subsequent analysis of spindle and endosome asymmetries considered in this report. **e**–**g**, Analysis of spindle inversion in the nanobody assay using a battery of microtubule markers. **e**, Enrichment in pIIb of GFP–Patronin in GFP–Patronin control and GFP–Patronin + GBP–Pon cells. Co-expression of GFP–Patronin and GBP–Pon induces a shift of the frequency distribution of GFP–Patronin asymmetry towards enrichment in pIIa and lower levels of enrichment in pIIb. In these conditions, inverted spindles are observed, which are only very rarely seen in control cells. **f**, Dividing control or GFP–Patronin and GBP–Pon expressing SOPs stained by anti-acetylated-α-tubulin (Ac-tubulin) immunofluorescence. **g**, Enrichment in pIIb of Ac-tubulin in control and GFP–Patronin + GBP–Pon cells. Note the shift towards pIIa enrichment induced by coexpression of GFP–Patronin and GBP–Pon. **h**, Percentage of $iDelta_{20}$ in the pIIa daughter cell at late cytokinesis upon expression of the indicated fusion proteins. Co-expression of GBP–Pon with GFP–Patronin causes a statistically significant reduction of $iDelta_{20}$ asymmetry compared to control. $^{*}P < 0.001$ compared to control, as calculated by ANOVA followed by Tukey's post hoc test. Comparisons between the other genetic backgrounds and the control or between themselves are not significant. All images in this figure correspond to SDCM imaging (maximum-intensity projection). n, number of SOPs scored. Scale bars, 5 μm.

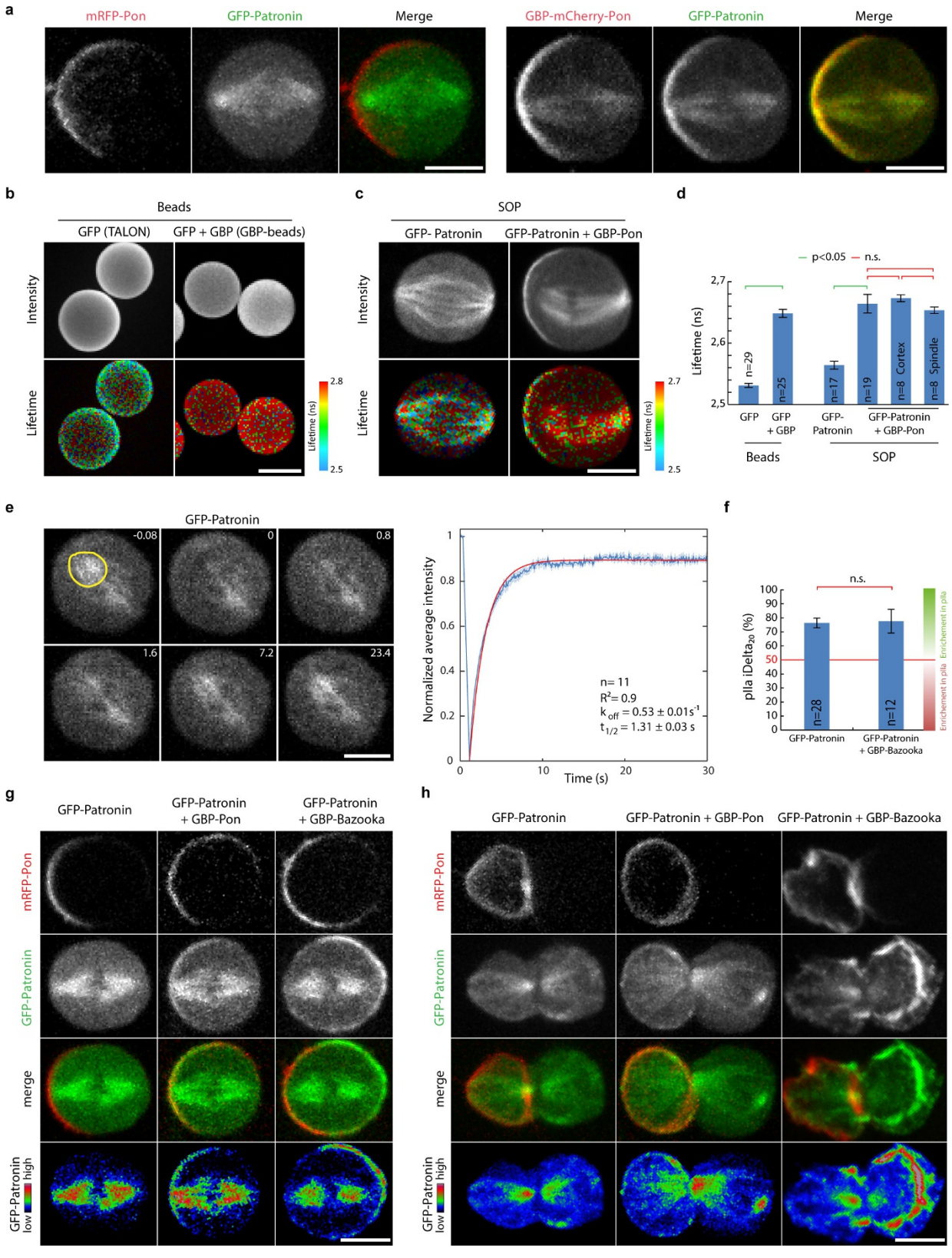

Extended Data Figure 9 | See next page for caption.

Extended Data Figure 9 | Rationale of the nanobody assay. a–d, Most GFP–Patronin in the SOP is bound to GBP–Pon. **a**, Dividing SOPs expressing mRFP–Pon and GFP–Patronin (left panels) or GBP–mCherry–Pon and GFP–Patronin (right panels) were imaged by SDCM (maximum-intensity projection). Note that GBP–mCherry–Pon colocalizes with GFP–Patronin both at the cortex and at the spindle. **b**, GBP binding increases the fluorescence lifetime of GFP *in vitro*. Purified $(His)_6$–GFP was coupled to TALON beads through the $(His)_6$ tag (left panels) or to GBP beads through GFP itself (right panels). The GFP fluorescence lifetime was imaged by FLIM (see Methods). Bottom panels correspond to images where abundance of GFP (pixel intensity) is combined with (multiplied by) the lifetime of GFP (pixel colour). Note that lifetime increases (that is, more red pixels) in the GBP beads when compared to the TALON beads (more cyan pixels). **c**, GBP binding increases the fluorescence lifetime of GFP–Patronin *in vivo*. Dividing SOPs expressing mRFP–Pon and GFP–Patronin (GFP–Patronin, control) or expressing GBP–Pon in addition (GFP–Patronin + GBP–Pon) at metaphase imaged by FLIM. As in **b**, bottom panel corresponds to images where abundance of GFP–Patronin (pixel intensity) is combined with its lifetime (pixel colour). Note that lifetime increases (that is, more red pixels) in the GBP–Pon sample. **d**, GFP lifetime measurements in the samples described in **b** and **c** (mean ± s.e.m. of different beads or cells; n, number of beads or cells scored). Note that lifetimes of GFP–Patronin are the same in the spindle and the cortex in the GFP–Patronin + GBP–Pon SOP, and that this homogenous lifetime value in the SOP corresponds to that of $(His)_6$–GFP bound to nanobody beads. This suggests that most GFP–Patronin molecules are bound to the nanobody in the SOP. Please note that in the experiments described in **b** (purified GFP) and in **c** (GFP–Patronin fusion in the fly) the term GFP refers to the enhanced GFP variant (eGFP). **e**, Fluorescence recovery after photobleaching (FRAP) of GFP–Patronin at the spindle. Left panel, images from the FRAP experiment. Fluorescence of GFP–Patronin at the mitotic spindle was bleached (yellow region of interest) and fluorescence recovery was monitored over time. Elapsed time, indicated in seconds. Right panel, average recovery of 11 cells (blue curve; mean ± s.e.m.) was fitted to a single exponential model (red line), providing an estimate of the half-life of GFP–Patronin on microtubules of 1.31 ± 0.03 s (95% confidence interval). This indicates that Patronin exchanges rapidly between the cytosol and the spindle. **f–h**, Co-expression of GBP–Bazooka and GFP–Patronin does not cause central spindle inversion in the SOP. **f**, Percentage of $iDelta_{20}$ in the pIIa daughter cell at late cytokinesis in SOPs expressing GFP–Patronin (GFP–Patronin) or expressing GBP–Bazooka in addition (GFP–Patronin + GBP–Bazooka). Co-expression of GBP–Bazooka with GFP–Patronin does not cause a statistically significant reduction of $iDelta_{20}$ asymmetry compared to control. ($P = 0.847$, unpaired two-tailed *t*-test). **g**, Dividing SOPs expressing mRFP–Pon and eGFP–Patronin (GFP–Patronin) or expressing GBP–Pon in addition (GFP–Patronin + GBP–Pon) or GBP–Bazooka in addition (GFP–Patronin + GBP–Bazooka) in metaphase. SDCM imaging (single plane). Bottom panels correspond to the rainbow lookup table. GBP–Pon targets GFP–Patronin asymmetrically to the cortex of the pIIb and, conversely, GBP–Bazooka targets GFP–Patronin asymmetrically to the cortex of the pIIa. Note that, in metaphase, the mitotic spindle is symmetric in control, but also in the two GBP conditions. **h**, Dividing SOPs as in **g** in late cytokinesis. GBP–Pon inverts the asymmetry of the central spindle, whereas GBP–Bazooka does not (it shows the same asymmetry as in control). SDCM imaging (maximum-intensity projection, except GFP–Patronin in the GFP–Patronin + GBP–Bazooka image, which corresponds to a single plane). n, number of SOPs scored. Scale bars, 5 μm (**a**, **c**, **e**, **g**, **h**) and 40 μm (**b**).

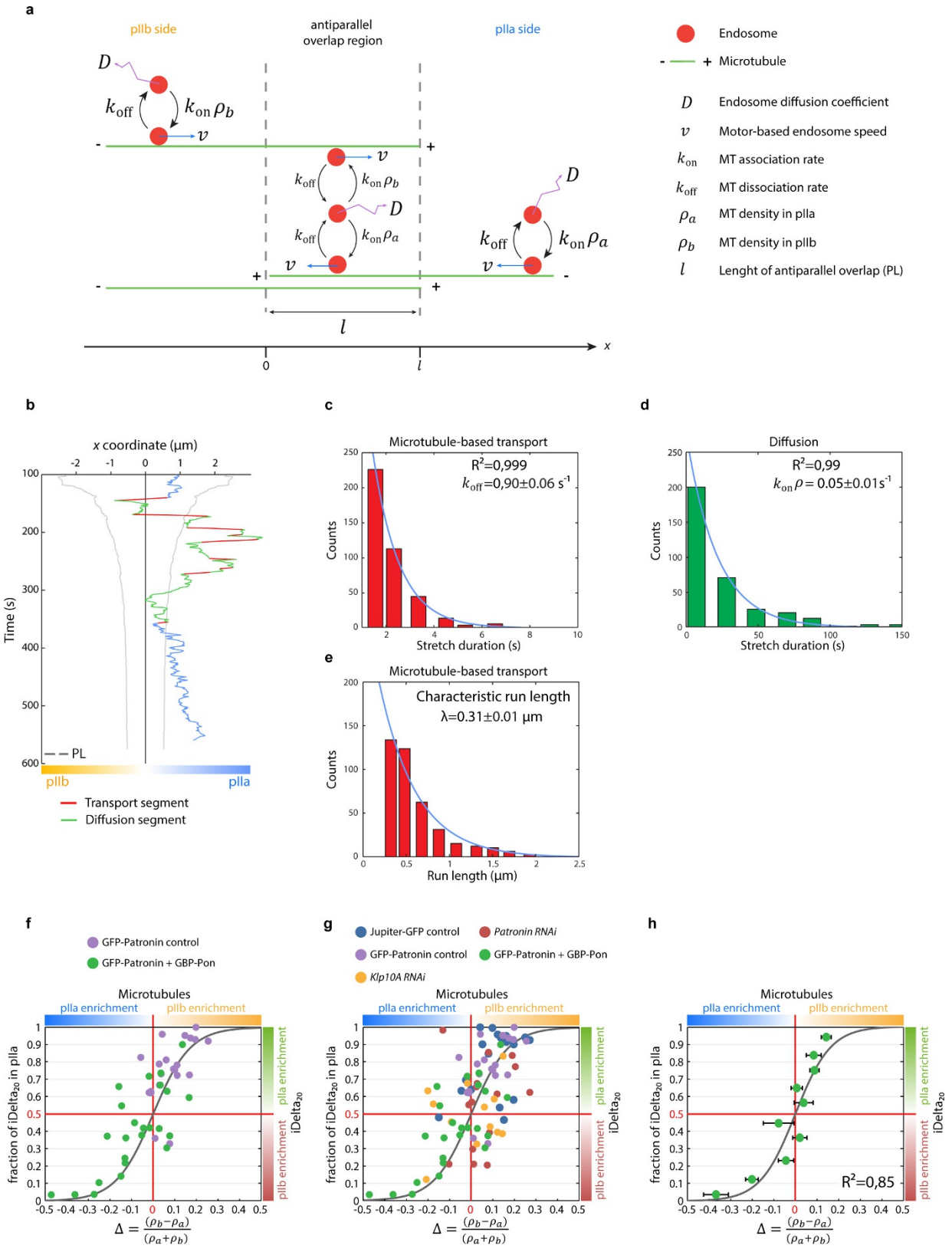

Extended Data Figure 10 | See next page for caption.

Extended Data Figure 10 | Model of motility onto an asymmetric central spindle. a, Schematic representation of a model of bidirectional motor transport, which generates a biased spatial distribution of endosomes through an antiparallel microtubule overlap (see Supplementary Information equations). **b**–**e**, Determination of k_{off} and $k_{on}\rho$ of endosomes for microtubules and transport run length in control cells (see also 'Determination of k_{off} and $k_{on}\rho$ and transport run length' in Methods for details). **b**, Representative endosome track at the central spindle (along the x axis, as in Fig. 2e) after automated detection of transport segments (that is, motility occurs by microtubule-based transport; red) and of diffusion segments (that is, movement occurs by diffusion; green). Blue segments correspond to the initial and final segments of the track, the total length of which cannot be determined and are therefore excluded from the analysis. Grey line, extent of the Pavarotti antiparallel overlap of microtubules as in Fig. 2. **c**–**e**, Distribution of the duration (**c**, **d**) and the run length (**e**) of transport segments (**c**, **e**) and/or diffusion-segments (**d**) from 101 tracks. Exponential fits (blue lines) give $k_{off} = 0.90 \pm 0.06\,s^{-1}$ (**c**) and $k_{on} = 0.05 \pm 0.01\,s^{-1}$ (**d**; 95% confidence interval). Characteristic run length was not estimated from exponential fit of this distribution in **e**, but instead by the method of Thorn and Vale (ref. 65), which relies on the fitting of the cumulative distribution of the run length (see Methods). The estimated characteristic transport run length is $\lambda = 0.31 \pm 0.01\,\mu m$ ($R^2 = 0.98$; 95% confidence interval). **f**, Endosome asymmetric segregation (that is, $\frac{P_{pIIa}}{P_{pIIa}+P_{pIIb}}$; P_{pIIa} , iDelta$_{20}$ signal in pIIa; P_{pIIb}, in pIIb) as a function of the central spindle asymmetry (that is, $\Delta = \frac{\rho_b - \rho_a}{\rho_b + \rho_a}$; ρ_b, GFP–Patronin density in the pIIb side; ρ_a, in pIIa) for GFP–Patronin control ($n = 21$) or GFP–Patronin + GBP–Pon ($n = 25$) cells at during late cytokinesis (~600 s in registered time). The same data are shown in bins in Fig. 4h. The experimental data points fall on the theoretical curve (grey line corresponding to equation (36), with measured parameters values; see Supplementary Information equations) which accounts for the different levels of spindle reversal and their corresponding endosome segregation reversal measured in this assay. **g**, Fraction of iDelta$_{20}$ versus microtubule enrichment as in **f**, considering the data from all the genotypes presented in this study. The model (grey line, as in **f**) for asymmetric bidirectional transport accounts for all spindle asymmetry/endosome asymmetries found across all the backgrounds presented in this study. **h**, Fraction of iDelta$_{20}$ versus microtubule enrichment as in **g**. The model outside of the limit case (grey line corresponding to equation (37) with measured parameters values and fitted $l = 3.2\,\mu m$, see Supplementary Information equations) also accounts for all spindle asymmetry/endosome asymmetries found across all the backgrounds presented in this study.